Marine Biofluidics in Benthic (and Naval) Systems

Elizabeth Ann Keatinge Murphy

Lafayette, California

B.A., University of California, Berkeley, 2009

A Dissertation presented to the Graduate Faculty

of the University of Virginia in Candidacy for the Degree of

Doctor of Philosophy

Department of Environmental Sciences

University of Virginia

August, 2018

Contents

Abstract

Marine biofluidics is the study of how organisms interact with their fluid environments at the intersection of biology and fluid physics. An integrative field, it addresses fundamental and applied questions about the feedbacks that connect physical and biological characteristics of the ocean, and how these interact with other processes such as chemical cycling. The research described in this dissertation advances both fundamental understanding and practical application of marine biofluidics. Specifically, I studied how burrowing organisms pump oxygenated water through burrows change the chemical characteristics of coastal sediments, and how this mediated by water temperature. I also studied how biofilm growth creates drag on aquatic surfaces, with an emphasis on ship hulls for which this drag has enormous economic consequences.

Burrowing organisms play a central role in shaping the chemical characteristics of coastal sediments by pumping oxygenated water through burrows into what would otherwise be an anoxic environment. In cohesive sediments, oxygenated burrow water allows for the diffusive flux of oxygen across the burrow wall and into the sediment, where it is consumed. In a series of laboratory experiments, I used particle image velocimetry (PIV), planar optodes, and a transparent mud analog that I developed to measure the water movements and oxygenation patterns in and around the burrows of a common coastal polychaete, the nereid *Alitta succinea*.

The polychaete ventilates its burrows through undulatory pumping, but this activity is periodic, resulting in pulses of oxygen flux across the burrow wall and into the sediments. The frequency and magnitude of pumping (and hence oxygen pulses) depends strongly on water temperature. I found that the volume of oxygenated sediment, as well as the pattern of oxygenation that sediment experiences, vary substantially due to seasonal shifts in water

temperature, but that total oxygen flux remains relatively uniform. Collectively, my results demonstrate that animal behavior can cause dramatic changes in the chemical environment of sediments and that these processes are tied to environmental parameters such as water temperature, which is changing in many regions across the planet.

Biofilms are bacterial and algal cells that form a thin layer on most aquatic surfaces including streambeds, coral reefs, and ship hulls. Biofilms are known to impact the dynamics of the fluid environment, for example increasing skin friction on surfaces, but the processes contributing to this are poorly quantified. In this dissertation, I studied the impact of biofilm fouling on boundary layer flow structure at moderate, ship-relevant Reynolds numbers. Specifically, I measured the characteristics of the turbulent boundary layer over diatomaceous-slime-fouled plates using high resolution PIV. The mean velocity profile over biofilm has a large downward shift due to momentum extracted from the flow, and higher friction velocity and drag coefficient compared to a control plate with no biofilm. Due to the complex nature of the biofilm's topography, the Reynolds shear stress, turbulence production, and dispersive stress is highly heterogeneous in the streamwise direction. The strength of instantaneous turbulent events also increased, enhancing vertical momentum transport to and from the biofilm, and the bed, if exposed. Collectively, these processes increase the effective roughness of a surface significantly more than the physical thickness of the biofilm. Patchy biofilms have the greatest increase in near- bed turbulence production, dispersive stresses, and rotational flow, compared with a uniform biofilm or a sparse biofilm. Uniform biofilm, however, increases the drag coefficient of the bed more than patchy biofilms. These results contribute to understanding the mechanisms that fuel biofilm growth on diverse surfaces by bringing nutrients to and removing metabolites from the organism. They also have immediate importance for understanding biofouling impacts

on ships and autonomous underwater vehicles. Specifically, my results show that percent cover of a biofilm is a good indicator of the effect of a biofilm on ship performance and could be used to schedule optimal cleaning frequencies.

Acknowledgments

I have been truly lucky to work with a number of kind, smart and supportive mentors and colleagues. I am beyond grateful for my advisor, Matthew Reidenbach, whose support, guidance and good humor have made this process truly enjoyable. I would often head into meetings with Prof. Reidenbach feeling lost and unsure of myself, and emerge reinvigorated, excited by my data and feeling much more positive about my abilities as a scientist. I was also incredibly lucky to end up working with Julio Barros, Michael Schultz and Karen Flack at the United States Naval Academy. They took me on despite my not having much background in fluid mechanics and gave me access to state- of- the- art equipment and a very cool slime tank, and then tons of support in collecting, processing and analyzing my data, allowing me the space and time to wallow in the data but also being readily available with insight into even my more basic questions. The staff in the hydromechanics lab at the USNA were also a huge help with getting experiments working and keeping the slime tank running, especially Mark Pavkov, Dan Rhodes and Michael Stanbro. I am also grateful to he staff of the ABCRC for logistical support, especially Donna Fauber, and Art Schwarzschild, for sharing his love of the Easter Shore.

I also thank my dissertation committee, Patricia Wiberg and Peter Berg, for their guidance and insight during this process, and Mike Mellon for serving on my committee early in my PhD and providing helpful guidance on my proposal, and Christopher Goyne for kindly agreeing to be on my committee for my defense at rather the last minute. My labmates, especially Martin Volaric for being a great field and lab buddy, and Jon Stocking, provided support and good conversation. Undergraduate students Kendall Combs and Dustin Pike made

my first summer as a graduate student as enjoyable and productive as possible, and assisted with specimen collection.

I would also like to thank Kelly Dorgan, who I began working with as an undergraduate where Kelly and her work inspired my interest in burrower biomechanics and polychaetes in particular, and provided early, wonderful opportunities for research. Kelly continues to provide professional guidance, mentorship and friendship. I wouldn't be here without her. Mimi Koehl introduced me to biomechanics and to Kelly, and her work continues to inspire me.

For all of this, I blame my parents, Daniel Murphy and Connie Keatinge. Because they put me in science camp when I was little, and encouraged my love of the outdoors, and have always been exceptionally supportive. Special thanks to Connie Keatinge, who showed me how to have a demanding career and be a good mom, and more directly, provided a lot of last minute childcare so I could finish this dissertation!

I am also grateful for David Seekell, who has kept me fed and kept me from being buried in an avalanche of dirty coffee mugs these past few months. I appreciate his steady encouragement and willingness to read my writing and provide helpful critiques, and also ice cream. I also appreciate his unflagging good naturedness in the face of packing up and moving to Annapolis every summer for three years and for keeping me company during lonely wintertime lab work at the Shore. While I am also grateful for Charlotte Seekell, she has been the opposite of helpful, and so she gets whatever the opposite of an acknowledgment is.

Funding and support for this work was provided by the University of Virginia Department of Environmental Sciences, PreSens Precision Sensing GmbH, which loaned the planar optode system used in Chapter 1, the National Science Foundation via a Graduate Research Fellowship and a GRIP internship support and funding, and a Grant (NSF-DEB

1237733) to the Virginia Coast Reserve Long Term Ecological Research site, and the Office of Naval Research via the NURP program.

Introduction

Biofluidics

Biofluidics is the study of how organisms interact with their fluid environments. It is interdisciplinary in nature, existing at the nexus of biology and fluid physics. Biofluidics research is worthy in its own right as curiosity-driven science, and also because the field lends itself to solving more immediate human problems. The study of biofiluidics can take advantage of millions of years of evolutionary experiments, leading to novel engineering insights in the form of bio-inspired design (Patek 2014; Lauder and Madden 2006). Biofluidics can also help scientists understand the links between ecology and the environment. For example, many organisms considered ecosystem engineers, e.g. seagrasses (Bos et al. 2007), interact with the surrounding fluid in a way that alters ecosystem processes and services and alters habitat suitability for other organisms (Jones et al. 1994; Coen et al. 2007). Lastly, this field is also relevant when solving problems of organisms impacting engineered systems.

The research presented in this dissertation focuses on biofluidics in two rather different systems: animal burrows in marine sediments and biofouling on ship hulls. Specifically, this work applies the principles of biofluidics to study the effects of burrowing organisms on sediment chemistry in coastal ecosystems, the fluid mechanics of burrow ventilation, the effects of biofouling on ship performance, and the effects of biofilm community morphology on boundary layer flow. The following section introduces the concept of bioturbation and the role bioturbation plays in coastal sedimentary processes, and lays out the approach taken here in filling in some of the knowledge gaps surrounding small scale fluid and mass transport in

burrows, and why these knowledge gaps matter. Next, I discuss the impacts of biofilm fouling on Naval ship performance, which was the driving impetus behind the second section of the dissertation, and also outline the effects of biofilms on some other systems, both engineered and natural, that the research presented here has implications for.

Fluid dynamics of burrow ventilation

Marine sediments, by area, are the largest habitat on earth (Snelgrove 1997). The physical and chemical properties of the sediments are intimately intertwined with the fauna that live within them- the zoobenthos, or infauna- both dictating the distribution of these organisms (Anderson 2008; Gray 1974; Snelgrove and Butman 1994) and being altered by them, physically (Rhoads and Boyer 1982) and chemically (Aller 1982). Infauna, therefore, play a major role in most important processes occurring in or mediated by marine sediments. In aquatic environments, the term bioturbation includes sediment reworking via particle mixing and transport, as well as burrow ventilation, which is the advective transport of overlying water into a burrow tube, typically for respiration or feeding

> *"Worms have played a more important part in the history of the world than most persons would at first suppose."*
>
> -Charles Darwin (1881), *The Formation of Vegetable Mould, Through the Action of Worms: With Observations on Their Habits*

Ecosystem engineers are "…organisms that directly or indirectly modulate the availability of resources to other species, by causing physical state changes in biotic or abiotic materials. In so doing they modify, maintain and create habitats" (Jones et al. 1994). Charles Darwin was one of the first scientists to recognize the activities of burrowing organisms as having profound consequences to the physical structure of the environment in which they live (Darwin 1881; Kristensen et al. 2012). Darwin published a book detailing his observations of sediment reworking by terrestrial earthworms, and thus the concept of bioturbation was introduced. Darwin (1881) noticed that earthworms brought a large amount of buried earth to the surface through burrow building activities, and this plus the collapse of abandoned burrow tubes resulted in the burial of plant matter, stones and even archaeological artifacts.

(Kristensen et al. 2012). Coastal areas are hotspots of burrower activities, where bioturbation often plays a critical role in ecosystem functioning and processes. Global cycling of oxygen, carbon and other nutrients (Waldbusser et al. 2004), the fate of pollutants (Benoit et al. 2006), and the transport of sediments (Grant and Daborn 1994) are all such processes. In the Precambrian, it is hypothesized that the advent of burrowing organisms, and thus bioturbation, resulted in globally diminished stocks of available atmospheric oxygen due to the reduction of sulfur in marine sediments, facilitated by burrowers (Boyle et al. 2014; Canfield and Farquhar 2009). Though infauna are critical to globally consequential processes, much of this activity occurs on small spatial and temporal scales. However, many of the research methods used to study the impacts of burrowers are unable to resolve these small scales, leaving a gap in our understanding of burrower- sediment interactions. We know that in aggregate and over large distances and amounts of time, burrowing organisms are ecosystem engineers. How, then are these processes occurring at the organismal scale? Specifically, how does burrower behavior, especially as it can be impacted by environmental changes, affect the transport of solutes into marine sediments?

Burrow ventilation

A major factor in the influence of bioturbation on nutrient cycling and the fate of organic carbon and pollution is the introduction of oxygen by burrowers into otherwise anoxic sediments. Cohesive sediments especially are oxygen depleted below the top few millimeters (Rasmussen and Jørgensen 1992), due to the diffusion limited nature of solute transport in the porewater and the consumption of oxygen by microbes (Glud 2008). As oxygen is depleted, other, less preferential electron acceptors are used for microbial respiration. It is this cascade of electron

acceptors that drives vertical chemical zonation in marine sediments, the cycling of many nutrients, and the relative respiration or sequestration of organic carbon. In defaunated sediments, the more favorable an electron acceptor is, the closest to the surface of the sediment it is depleted, resulting in a redox profile of oxygen, nitrate, manganese oxide, iron oxide, and sulfate depletion with depth, in that order (Froelich et al. 1979). However, in sediments where there is burrower activity, this zonation is altered in highly spatially and temporally heterogeneous patterns via pumping of oxygenated water into burrows (Fenchel 1996), resulting in additional fluxes of oxygen through the burrow walls and into the sediment. Anyone who has dug up a worm or clam burrow in the muddy intertidal zone may have noticed a zone of lightly colored sediment surrounding the burrow, in contrast with the dark sediment further from the burrow (Fig. 1). This lighter colored sediment is oxic due to the presence of the burrow, as opposed to the dark colored reduced sediment (Sturdivant and Shimizu 2017).

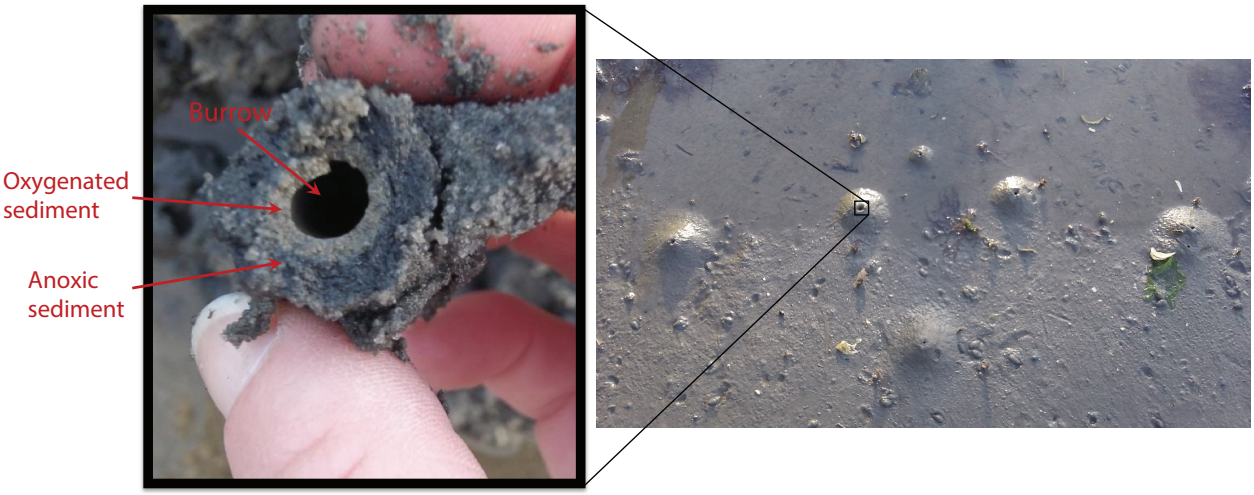

Figure 1. Example of oxic sediment surrounding a polychaete burrow, collected from muddy intertidal sediments on the Delmarva Penninsula, VA, USA.

Most studies of biologically- mediated oxygen transport use enclosure techniques which integrate oxygen transport over large spatial and temporal scales. These studies have shown that burrowers increase benthic oxygen uptake by up to 85% (Forster and Graf 1995). However, this type of method cannot resolve small scale variability. Chemical and physical heterogeneity on small temporal and spatial scales is the default state for faunated sediments (Volkenborn et al. 2012; Aller 1982; Zeibis 1996; Kristensen 2000; Jovanovic et al. 2014), and this variability has profound effects on microbial activity and therefore nutrient cycling, organic matter diagenesis, and even pollutant transport and transformation. Temporally variable oxygenation alters the sediment microbial community and can result in enhanced microbial respiration of organic matter compared to a steady oxygenated state (Urban-Malinga et al. 2013; Aller 1994). Similarly, mercury is methylated to the more bioavailable and highly toxic form more readily under oscillating redox conditions (Bouchet et al. 2011).

Approach

For these reasons, measuring small scale solute transport, burrow flow dynamics and ventilation behavior at high temporal resolutions is important, but relatively overlooked. In a series of laboratory experiments, I used particle image velocimetry (PIV), planar optodes, and a transparent mud analog that I developed to measure the water movements and oxygenation patterns in and around the burrows of a common coastal polychaete, the nereid *Alitta succinea*.

Visualizing burrowing and ventilation activities in sediments is a challenge due to the opaque nature of sediments. Measurements of ventilation activity have been made using artificial

tubes (Stamhuis and Videler 1998; Kristensen 1983; Wohlgemuth et al. 2000), porewater pressure transducers (Wethey et al. 2008), planar optodes (Volkenborn 2010; Volkenborn 2012b; Wenzhofer and Glud 2004), and flow measurements or modeling at the burrow entrance or exit (Jumars 2013; Ridd 1996). Other researchers have used transparent mud or sand analogs to visualize burrowing mechanics in different types of sediments (Dorgan et al 2007; Murphy and Dorgan 2011; Dorgan 2018), or in one of few studies to measure burrowing behavior in natural sediments, tracked the motion of sand grains in burrowed sediment (Du Clos 2014). Here, I use planar optodes and particle image velocimetry at the burrow entrance to link burrower ventilation behavior with fluid mechanics and mass transport. I also develop a novel transparent mud analog in which a polychaete will readily build a semi- permanent and particle tracking inside of burrows built by the study organism in a transparent mud analog to measure the fluid dynamic characteristics within a ventilated burrow. For this work, I chose a common coastal polychaete, *Alitta succinea* (Leuckart 1847; formerly *Neanthes succinea*) as my study organism. A nereid polychaete, *A. succinea* is found in intertidal and subtidal coastal sediments worldwide, and has been recorded occurring in densities up to 600 m^{-2} (Rasmussen 1973). As intertidal organisms, this species is able to withstand wide variations in temperature and salinity. It is thought to be introduced in some locations (Carlton, 1979) and its presence has been shown to impact sediment biogeochemistry, including oxygen uptake by sediments and denitrification rates (Bartoli et al. 2000). In addition to effects on sediment, *A. succinea* is an important food source for coastal fish species, including economically important species (Muus 1967; Proskurina 1980). As detritus feeders, these polychaetes provide an energy link between benthic and pelagic food webs (Neuhoff 1979). This species is also a rapid colonizer of disturbed soft

bottom habitats (Holland et al. 1977) and has been introduced in some areas, such as the San Francisco Bay and the Caspian Sea (Fong 1987; Ghasemi et al. 2013).

Chapters 1 and 2 investigate how intermittent pumping by *A. succinea* alters the fluid exchange and oxygen transport within low oxygen, muddy sediments within the Virginia Coast Reserve. Chapter 1, which is a detailed study of oxygen transport due to burrow ventilation, was published in the journal *Marine Biology* (Murphy and Reidenbach 2016). The second chapter is in preparation as a manuscript.

Biofilm fouling

Biofouling is the attachment and growth of organisms on wetted surfaces. In the marine environment, biofouling organisms are diverse, including macroalgae, hard shelled animals such as barnacles, tube worms, and biofilms (also called slime). People have been battling biofouling for centuries, with written records of antifouling efforts dating to the 1st century, when the scholar Plutarch wrote of ships "…it is probable that it glides lightly, and as long as it is clean, easily cuts the waves; but when… weeds, ooze, and filth stick upon its sides, the stroke of the ship is more obtuse and weak; and the water, coming upon this clammy matter, doth not so easily part from it; and this is the reason why they usually scrape the sides of their ships" (Plutarch 1870; Field 1981). Presumably, ooze refers here to biofilm fouling. Ancient mariners clearly recognized that biofouling increased the power requirements of ships and altered ship hydrodynamics, and in addition to mechanical cleaning of hulls, early anti-fouling coatings such as wax and lead sheathing were used (Field 1981). Currently, surface treatments that prevent fouling (anti-fouling coatings) or that decrease the adhesive strength of foulers (fouling-release coatings) are used to control fouling, as well as hull cleaning. These coatings can be expensive,

toxic to the environment (such as copper- based coatings), or require frequent re-application. Mechanical cleaning of the hull is expensive, labor intensive, and results in large ships being out of commission for an extended period of time. In addition, anti-fouling and fouling-release coatings which are effective at preventing hard fouling organisms such as barnacles, are often still colonized by biofilms (Molino and Wetherbee 2008). Bacteria and algae that can be either planktonic or biofilm forming exhibit higher resistance to environmental stresses such as decreased salinity, and increased resistance to antibiotics (Stoodley 2004; Decho 1990). This can make biofilms good reservoirs of pathogenic bacteria, and also makes biofilm fouling difficult to eradicate.

Biofilms are aggregates of single-celled organisms embedded in a matrix of gel-like extracellular polymeric substance (EPS) that coat moist or aquatic surfaces. Biofilms can be microbial, algal, or both, and some have thin filamentous streamers protruding from the surface, depending on the hydrodynamic conditions under which the biofilms grow. Biofilms are also difficult to prevent and eradicate on ship hulls, where they exact a steep drag penalty. On ships, biofilms tend to be diatomaceous slimes (Schultz et al. 2011)- a type of low form algal biofilm.

Despite significantly impacting the performance of ships and other engineered aquatic systems, the boundary layer hydrodynamics of biofilms are poorly understood. Due to the complex nature of the biological assemblages in biofilms, the interaction of a biofilm with the boundary layer flow over a ship hull is complicated, and the induced resistance is difficult to model. This complexity is compounded by the fact that biofilm fouling is not well- studied, especially compared to other types of fouling, such as calcareous algae (Townsin, 2003).

On an otherwise smooth ship hull, biofilm fouling essentially adds roughness to the surface. Ships underway experience drag from two sources: residuary resistance and frictional

resistance, where residuary resistance is primarily due to the wake of the vessel. Drag from frictional resistance is a result of viscous shear stress on a surface. Roughness elements on a ship's hull are subject to pressure drag and increase the shear stresses at the wall, increasing the drag on the vessel. Increased drag as a result of biofouling, primarily biofilm fouling, results in increased fuel consumption, decreased maximum speed of the vessel, and a reduced operational range. Biofouling is estimated to cost the Navy $56 million per year for their mid-sized vessels due to increased fuel consumption and the costs of cleaning and painting the hull (Schultz et al. 2011). In addition to the economic and performance impact of biofouling, increased fuel consumption results in larger than necessary greenhouse gas emissions from shipping and Naval activities.

Rough wall boundary layers

Resistance due to frictional drag is a result of the boundary layer conditions on a ship hull. The friction drag coefficient is a function of the shear stress on a body. The viscous shear stress is a function of the velocity gradient at the wall. In turbulent flow, which characterizes any flow over a ship hull, the shear stress is composed of both the turbulent shear stress and the viscous shear stress. The turbulent shear stress is a function of the turbulent velocity fluctuations at the wall, and is generally called the Reynolds stress.

Adding roughness to a surface, such as that due to biofouling organisms, increases the frictional drag on that surface, and biofilms are known to increase drag on surfaces substantially, despite their slimy nature (Andrewartha et al. 2010; Schultz and Swain 2000). Surface roughness elements increase the wall shear stress, and interact with the viscous sublayer by shedding

eddies, which increase turbulence at the surface, and creating flow separation, which induces pressure differentials along the surface (Dade et al., 2001).

Previous work has shown that biofilms extract momentum from boundary layer flow, resulting in a downward shift in the mean streamwise velocity profile. This equates to a large equivalent sandgrain roughness height (Walker et al. 2013; Schultz and Swain 1999; Schultz 2000), and contributes to the large drag coefficient on biofilm fouled surfaces. However, the mechanisms behind this large effective roughness height and drag penalty are poorly understood. This section of this dissertation addresses this knowledge gap by providing a more mechanistic understanding of biofilm drag.

> *"Indeed, the underlying complexity of fluid mechanics can be something of a boon, since it greatly restricts the possibilities of exact mathematical solutions or trustworthy simulations. Thus the investigator must often resort to the world of direct experimentation and simple physical models, a world in which the biologist can feel quite at home"*
>
> -Steven Vogel (1996) *Life in Moving Fluids: The physical biology of flow*

Approach

We were able to acquire very high quality PIV data over biofilms in fast (moderate Reynolds number) flow. Two dimensional flow data like that presented here is rare in studies of organism- flow interactions, and the studies conducted provide new insights into the generation of turbulence and momentum transport in biofilm boundary layer flow. Chapters 3 and 4 examine the two dimensional flow structure over uniform and patchy biofilms at moderate, ship-

relevant Reynolds number, especially focusing on the spatial heterogeneity of turbulence and coherent structures in the flow.

Biofilm experiments were carried out in the hydromechanics lab at the United States Naval Academy (USNA). Diatomaceous biofilms were grown under shear in a dynamic slime exposure facility from a culture of diatoms collected from a plate exposed to the environment in the Indian River Lagoon, FL (Schultz et al. 2015). Flow imaging was carried out by high resolution PIV. Preliminary results from Chapter 3, which sets a baseline of understanding of biofilm boundary layers using a relatively uniform biofilm, were published as conference proceedings in a refereed conference paper (Murphy et al. 2017). The final results from Chapter 3 are in revision in the journal *Biofouling*. Chapter 4, which examines the effects of biofilm patchiness on the turbulent boundary layer, is in preparation as a journal article.

While biofilm impact on ship performance was the primary motivation behind Chapters 3 and 4, this work has additional implications, because biofilms are ubiquitous in wet environments, from human mouths to hotsprings (Wake et al. 2016; Hall-Stoodley et al. 2004). Biofilm growth in medical settings, such as tubing, as well as growth on food processing equipment, can lead to severe infections because biofilms can harbor pathogens and biofilm formation renders pathogenic bacteria more resistant to elimination by disinfecting or cleaning (use of surfactants) than non- biofilm forming bacteria (Kumar and Anand 1998; Davies 2003). Similarly, biofilms in coastal environments can harbor and protect virulent bacteria such as *Vibrio* on oyster reefs (Shikuma & Hadfield 2010). Biofouling is also ecologically problematic due to dispersal of invasive species (Canning-Clode et al. 2013) and smothering of coral reefs. Biofilm- fluid interactions drive the dispersal of biofilms and the transport of momentum to and from the bed. Therefore, an understanding of how biofilms influence the turbulent boundary

layer can also inform our understanding of how biofilms affects ecosystems, or how they spread in food production systems, or how they impact stream hydrodynamics. Likewise, in order to predict and model how global change affects burrower- mediated sedimentary processes, it is important to have a mechanistic understanding of burrower- sediment interactions. The research presented in this dissertation provides detailed knowledge of how organisms interact with fluids in ways that affect ecosystems and engineered systems.

References

Aller RC. 1982. The effects of macrobenthos on chemical properties of marine sediment and overlying water. In: *Animal-sediment relations*. 53-102. Springer, Boston, MA.

Aller RC. 1994. Bioturbation and remineralization of sedimentary organic matter: effects of redox oscillation. *Chem. Geol*. 114:331–345

Anderson MJ. 2008. Animal-sediment relationships re-visited: Characterising species' distributions along an environmental gradient using canonical analysis and quantile regression splines. *Journal of Experimental Marine Biology and Ecology*. 366(1-2):16-27.

Andrewartha J, Perkins K, Sargison J, Osborn J, Walker G, Henderson A, Hallegraeff G. 2010. Drag force and surface roughness measurements on freshwater biofouled surfaces. *Biofouling*. 26(4):487-96.

Benoit JM, Shull DH, Robinson P, Ucran LR. 2006. Infaunal burrow densities and sediment monomethyl mercury distributions in Boston Harbor, Massachusetts. *Marine Chemistry*. 102(1-2):124-33.

Bos AR, Bourna TJ, de Kort GLJ, van Katwijk MM. 2007. Ecosystem engineering by annual intertidal seagrass beds: Sediment accretion and modification. *Estuarine, coastal and shelf science*. 74:344-348.

Bouchet S, Bridou R, Tessier E, Rodriguez-Gonzalez P, Monperrus M, Abril G, Amouroux D. 2011. An experimental approach to investigate mercury species transformations under redox oscillations in coastal sediments. *Mar. Environ. Res*. 71:1-9.

Boyle RA, Dahl TW, Dale AW, Shields-Zhou GA, Zhu MY, Brasier MD, Canfield DE, Lenton TM. 2014. Stabilization of the coupled oxygen and phosphorus cycles by the evolution of bioturbation. *Nature Geoscience*. 7(9):671.

Canfield DE, Farquhar J. 2009. Animal evolution, bioturbation, and the sulfate concentration of the oceans. *Proceedings of the National Academy of Sciences*. 106(20):8123-7.

Canning-Clode J, Fofonoff P, McCann L, Carlton JT, Ruiz G. 2013. Marine invasions on a subtropical island: fouling studies and new records in a recent marina on Madeira Island (Eastern Atlantic Ocean). *Aquat. Inv.* 8(3), 261-270.

Coen LD, Brumbaugh RD, Bushek D, Grizzle R, Luckenbach MW, Posey MH, Powers SP, Tolley SG. 2007. Ecosystem services related to oyster restoration. *Marine Ecology Progress Series*. 341:303-307.

Dade WB, Hogg AJ, Boudreau BP. 2001. Physics of flow above the sedimenet- water interface. In: *The benthic boundary layer* (Eds. B. P. Boudreau and B. B. Jørgensen). Oxford University Press, Inc. New York, NY.

Darwin C. 1881. The formation of vegetable mould through the action of worms with observation on their habits. John Murray, London

Davies D. 2003. Understanding biofilm resistance to antibacterial agents. *Nature reviews Drug discovery*. 2(2):114.

Decho AW. 1990. Microbial exopolymer secretions in ocean environments: Their role(s) in food webs and marine processes. *Oceanogr Mar Biol Annu Rev*. 28:73-153.

Dorgan KM. 2018. Kinematics of burrowing by peristalsis in granular sands. *J Exp Biol*. 1:jeb-167759.

Dorgan KM, Arwade SR, Jumars PA. 2007. Burrowing in marine muds by crack propagation: kinematics and forces. *J. Exp. Biol*. 210:4198-4212

Du Clos KT. 2014. Visualizing subsurface burrowing by the polychaete Alitta virens with particle image velocimetry. *Limnology and Oceanography: Methods*. 12(10):703-12.

Fenchel T. 1996. Worm burrows and oxic microniches in marine sediments. 1. Spatial and temporal scales. *Marine Biology*. 127(2):289-95.

Field B. 1981. Marine Biofouling and its Control: History and State-of-the-Art Review. In *OCEANS* 81:542-544. IEEE.

Fong PP. 1987. Particle-size utilization in the introduced polychaete *Neanthes succinea* in San Francisco Bay. *Pacific Science*. 41(1):37-43.

Forster S, Graf G. 1995. Impact of irrigation on oxygen flux into the sediment: intermittent pumping by *Callianassa subterranea* and "piston-pumping" by *Lanice conchilega*. *Mar. Biol.* 123(2):335–346

Froelich P, Klinkhammer GP, Bender ML, Luedtke NA, Heath GR, Cullen D, Dauphin P, Hammond D, Hartman B, Maynard V. 1979. Early oxidation of organic matter in pelagic sediments of the eastern equatorial Atlantic: suboxic diagenesis. *Geochimica et cosmochimica acta*. 43(7):1075-90.

Ghasemi AF, Taheri M, Jam A. 2013. Does the introduced polychaete Alitta succinea establish in the Caspian Sea? *Helgoland marine research*. 67(4):715.

Glud RN. 2008. Oxygen dynamics of marine sediments. *Marine Biology Research*. 4(4):243-89.

Grant J, Daborn G. 1994. The effects of bioturbation on sediment transport on an intertidal mudflat. *Netherlands Journal of Sea Research*. 32(1):63-72.

Gray JS. 1974. Animal–sediment relationships. *Oceanogr. Mar. Biol. Annu. Rev*. 12:223–261.

Hall-Stoodley L, Costerton JW, Stoodley P. 2004. Bacterial biofilms: from the natural environment to infectious diseases. *Nature reviews microbiology*, *2*(2):95.

Holland AF, Mountford NK, Mihursky JA. 1977 Temporal variation in upper bay mesohaline benthic communities: I. The 9-m mud habitat. *Chesapeake Science*. 18(4):370-8.

Jones CG, Lawton JH, Shachak M. 1994. Organisms as Ecosystem Engineers. *Oikos*. 69:373-386.

Jovanovic Z, Larsen M, Organo Quintana C, Kristensen E, Glud RN. 2014. Oxygen dynamics and porewater transport in sediments inhabited by the invasive polychaete *Marenzelleria viridis*. *Mar Ecol Prog Ser* 504:181-192.

Jumars PA. 2013. Boundary-trapped, inhalant siphon and drain flows: Pipe entry revisited numerically. *Limnology and Oceanography: Fluids and Environments*. 3(1):21-39.

Kristensen E. 1983. Comparison of polychaete (*Nereis* spp.) ventilation in plastic tubes and natural sediment. *Marine ecology progress series*. 12(3):307-9.

Kristensen E. 2000. Organic matter diagenesis at the oxic/anoxic interface in coastal marine sediments, with emphasis on the role of burrowing animals. In: Life at interfaces and under extreme conditions. pp. 1-24. Springer, Dordrecht.

Kristensen E, Penha-Lopes G, Delefosse M, Valdemarsen T, Quintana CO, Banta GT. 2012. What is bioturbation? The need for a precise definition for fauna in aquatic sciences. *Marine Ecology Progress Series*. 446:285-302

Kumar CG, Anand SK. 1998. Significance of microbial biofilms in food industry: a review. *International journal of food microbiology*. 42(1-2):9-27.

Lauder GV and Madden PGA. 2006. Learning from fish: Kinematics and experimental hydrodynamics for roboticists. *International Journal of Automation and Computing*. 4:325-335.

Molino PJ, Wetherbee R. 2008. The biology of biofouling diatoms and their role in the development of microbial slimes. *Biofouling*. 24:365-379.

Murphy EAK, Dorgan KM. 2011. Burrow extension with a proboscis: mechanics of burrowing by the glycerid *Hemipodus simplex*. *J. Exp. Biol*. 214:1017-1027

Murphy EAK, Reidenbach MA. 2016. Oxygen transport in periodically ventilated polychaete burrows. *Marine biology*. 163(10):208.

Murphy EAK, Barros JM, Schultz MP, Flack KA, Steppe CN, Reidenbach MA. 2017. The Turbulent Boundary Layer Structure Over Diatomaceous Slime Fouling. Proceedings of the 10th international symposium on turbulent shear flow phenomenon. Chicago, IL USA

Muus BJ. 1967.The fauna of Danish estuaries and lagoons. Distribution and ecology of dominating species in the shallow reaches of the mesohaline zone. *Meddr. Danm. Fisk.-og Havunders*. 5:1-316.

Patek SN. 2014. Biomimetics and evolution. *Science*. 345(6203):1448-1449. DOI: 10.1126/science.1256617

Plutarch. 1870. Plutarch's Morals (translated from the Greek by several hands corrected and revisedby William W. Goodwin with an introduction by Ralph Waldo Emerson). Little, Brown & Co., Boston.

Proskurina YS. 1980. The state of introduced species in the Aral Sea and the prospects for their spread. *Hydrobiol J* 15:30–34

Rasmussen H, Jørgensen BB. 1992. Microelectrode studies of seasonal oxygen uptake in a coastal sediment: role of molecular diffusion. *Marine Ecology Progress Series*. 30:289-303.

Rhoads DC, Boyer LF. 1982. The effects of marine benthos on physical properties of sediments. In *Animal-sediment relations*. 3-52. Springer, Boston, MA.

Ridd PV. 1996. Flow through animal burrows in mangrove creeks. *Estuarine, Coastal and Shelf Science.* 43(5):617-25.

Schultz MP. 2000. Turbulent boundary layers on surfaces covered with filamentous algae. *Journal of fluids engineering*. 122(2):357-63.

Schultz MP, Swain GW. 1999. The effect of biofilms on turbulent boundary layers. *Journal of Fluids engineering*. 121(1):44-51.

Schultz MP, Swain GW. 2000. The influence of biofilms on skin friction drag. *Biofouling*. 15(1-3):129-39.

Schultz MP, Walker JM, Steppe CN, Flack KA. 2015. Impact of diatomaceous biofilms on the frictional drag of fouling-release coatings. *Biofouling*. 31:759-773.

Schultz MP, Bendick JA, Holm ER, Hertel WM. 2011. Economic impact of biofouling on a naval surface ship. *Biofouling*. 27(1), 87-98.

Shikuma NJ, Hadfield MG. 2010. Marine biofilms on submerged surfaces are a reservoir for *Escherichia coli* and *Vibrio cholerae*. *Biofouling*. 26(1):39-46.

Snelgrove PVR, Butman CA. 1994. Animal-sediment relationships revisited: cause versus effect. *Oceanogr. Mar. Biol. Annu. Rev*. 32:111–177.

Snelgrove PV. 1997. The importance of marine sediment biodiversity in ecosystem processes. *Ambio*. 1:578-83.

Stamhuis EJ, Videler JJ. 1998. Burrow ventilation in the tube-dwelling shrimp callianassa subterranea (Decapoda: thalassinidea). II. The flow in the vicinity of the shrimp and the energetic advantages of a laminar non-pulsating ventilation current. *J Exp Biol*. 201(14):2159-70.

Hall-Stoodley L, Costerton JW, Stoodley P. 2004. Bacterial biofilms: from the natural environment to infectious diseases. *Nature reviews microbiology*. 2(2):95.

Sturdivant SK, Shimizu MS. 2017. In situ organism-sediment interactions: Bioturbation and biogeochemistry in a highly depositional estuary. *PloS one*. 12(11):e0187800.

Townsin RL. 2003. The ship hull fouling penalty. *Biofouling*. 19, 9-16.

Urban-Malinga B, Warzocha J, Zalewski M. 2013. Effects of the invasive polychaete Marenzellaria spp. on benthic processes and meiobenthos of a species-poor brackish system. *J Sea Res* 80:25−34

Vogel S. 1996. *Life in moving fluids: the physical biology of flow*. Princeton University Press.

Volkenborn N, Polerecky L, Wethey DS, Woodin SA. 2010. Oscillatory porewater bioadvection in marine sediments induced by hydraulic activities of *Arenicola marina*. *Limnol. Oceanogr*. 55:1231-1247

Volkenborn N, Meile C, Polerecky L, Pilditch CA, Norkko A, Norkko J, Hewitt JE, Thrush SF, Wethey DS, Woodin SA. 2012a. Intermittent bioirrigation and oxygen dynamics in permeable sediments: an experimental and modeling study of three tellinid bivalves. *Journal of Marine Research*. 70(6):794-823.

Volkenborn N, Polerecky L, Wethey DS, DeWitt TH, Woodin SA. 2012b. Hydraulic activities by ghost shrimp *Neotrypaea californiensis* induce oxic-anoxic oscillations in sediments. *Mar Ecol Prog Ser.* 455:141–156

Wake N, Asahi Y, Noiri Y, Hayashi M, Motooka D, Nakamura S, Gotoh K, Miura J, Machi H, Iida T, Ebisu S. 2016. Temporal dynamics of bacterial microbiota in the human oral cavity determined using an *in situ* model of dental biofilms. *NPJ biofilms and microbiomes*. 2:16018.

Waldbusser GG, Marinelli RL, Whitlatch RB, Visscher PT. 2004. The effects of infaunal biodiversity on biogeochemistry of coastal marine sediments. *Limnology and Oceanography.* 49(5):1482-92.

Walker JM, Sargison JE, Henderson AD. 2013. Turbulent boundary-layer structure of flows over freshwater biofilms. *Experiments in fluids*. 54(12):1628.

Wenzhofer F, Glud RN. 2004. Small-scale spatial and temporal variability in coastal benthic O_2 dynamics: Effects of fauna activity. *Limnol. Oceanogr.* 49:1471-1481.

Wohlgemuth SE, Taylor AC, Grieshaber MK. 2000. Ventilatory and metabolic responses to hypoxia and sulphide in the lugworm *Arenicola marina* (L.). *J Exp Biol*. 203(20):3177-88.

Ziebis W, Forster S, Huettel M, Jørgensen BB. 1996. Complex burrows of the mud shrimp *Callianassa truncata* and their geochemical impact in the sea bed. *Nature*. 382(6592):619.

Chapter 1

Oxygen transport in periodically ventilated polychaete burrows

Elizabeth A. K. Murphy and Matthew A. Reidenbach

Department of Environmental Sciences, University of Virginia, Charlottesville 22904, USA

Note: This chapter was published in *Marine Biology* in 2016, and is presented here is a slightly modified form. The citation is: Murphy EAK, Reidenbach MA. 2016. Oxygen transport in periodically ventilated polychaete burrows. *Marine biology*. 163(10):208. doi:10.1007/s00227-016-2983-y

Abstract

Burrowing organisms play a critical role for the functioning of coastal marine sediments, in part due to their pumping of oxygenated water through the burrow. In cohesive sediments, oxygenated burrow water allows for the diffusive flux of oxygen across the burrow wall and into the sediment, where it is consumed. In this study, we quantified the burrow excurrent velocities, volume of water ventilated, and oxygenation patterns within the burrow of the polychaete *Alitta succinea.* We determined that periodic ventilation of the burrow results in oscillations of the flux

of oxygen across the burrow wall and oxygen concentration within the sediment near the burrow wall. Additionally, we investigated the effects of temperature changes on oxygen dynamics in the burrow. The volumetric flow rate and frequency of burrow ventilation increased with temperature. Correspondingly, the frequency of the oscillations in oxygen flux across the burrow walls also increased with temperature. However, the time averaged flux of oxygen across the burrow wall did not change with temperature (1.5 ± 0.3 mmol m^{-2} d^{-1}), and the distance of oxygen penetration into the burrow wall decreased with temperature (from 3.4 ± 0.5 mm at 6 °C to 1.6 ± 0.1 mm at 33 °C). Thus seasonal changes in the volume of oxygenated sediment, as well as the pattern of oxygenation that sediment experiences, is expected to be significant while the total oxygen flux is expected to remain relatively uniform. We show that burrower ventilation behavior mediates the effects of temperature on sediment oxygen uptake.

Introduction

Sediments play a critical role in the cycling of nutrients and carbon in marine systems (Boudreau and Jørgensen 2001). Within coastal sediments, a rich array of burrowing organisms, such as ghost shrimp, razor clams, polychaete worms and nemerteans burrow to seek refuge from predation and search for food (Wilson 1990). Marine sediments, ranging from muds to sands, possess specific mechanical properties. Muds are characterized as cohesive sediments due to the organic mucopolymer matrix that binds sediment grains (Dorgan et al. 2006), preventing advective transport of solutes in low-permeability muddy sediments (Glud 2008). Sandy sediments are typically permeable, allowing advective pore water transport (Janssen et al. 2005).

Many types of burrowing animals build permanent or semi- permanent burrows flushed with overlying water. Stagnant burrow water is quickly depleted of oxygen, due to the respiration of the burrower and microbes that live within the burrow walls (Kristensen 1985). In order to

maintain a favorable chemical environment, many burrowers flush their burrows with overlying, oxygenated water, a process referred to as burrow ventilation. Some animals also ventilate their burrows for other reasons, including feeding, removal of toxic metabolites or irritants, release of gametes, and environmental sensing (Wells and Dales 1951; Riisgård 1989; Kristensen and Kostka 2005; Smee and Weissburg 2006). In cohesive, low- permeability sediments, burrow ventilation results in enhanced diffusive transport of solutes between sediments and the water column by increasing the surface area available for diffusion, in some cases by as much as 400% (Ziebis et al. 1996). Solute transport between the water column and sediments due to burrow ventilation is known as bioirrigation (Kristensen et al. 2012), and this process has important biogeochemical consequences. Enhanced microbial breakdown of organic matter in bioirrigated sediments is a result of increased numbers of microbes and meiofauna, with higher numbers of microbes often found in oxic burrow walls than at either the sediment surface or anoxic subsurface sediments (e.g. nereidid burrow walls have an increase in bacterial abundance of 2.7-4.5 times the surrounding ambient sediment, depending on the species (Papaspyrou et al. 2006)). This also results in enhanced nutrient cycling and regeneration (Kristensen 2000; Karlson et al. 2005), such as an increase in nitrate fluxes from the sediment in the presence of burrowers, dependent on ventilation behavior (Henriksen et al. 1983), and 3- 5 fold increases in ammonium fluxes out of the sediment, dependent on burrow density (D'Andrea and DeWitt 2009).

Oxygen is typically diffusion limited in marine cohesive sediments, and therefore these sediments are anoxic below a thin layer (on the order of a few millimeters) at the sediment surface that is supplied with oxygen by diffusion (Gundersen and Jørgensen 1990). Oxygen is depleted within the sediment due to the consumption of oxygen during microbial respiration or the oxidation of reduced compounds (Jørgensen and Revsbech 1985; Glud 2008). Burrow

ventilation is therefore important for organic matter processing not only because it effectively increases the sediment- water interface, but the activity also introduces oxygen deep into otherwise anoxic sediments in a spatially and temporally heterogeneous manner. In many coastal sediments the total oxygen uptake is higher than the diffusive flux of oxygen across the sediment- water interface (Glud et al. 1994, 2003). This discrepancy is typically due to enhanced oxygen uptake mediated by burrowing macrofauna (Meile and Van Cappellen 2003). Organic matter remineralization in marine sediments is primarily due to microbial degradation of organic matter, the rate of which is controlled in large part by the availability of electron acceptors (especially oxygen) and the accumulation of toxic metabolites such as sulfide (Aller and Aller 1998). Burrowing organisms stimulate microbial respiration, and therefore rates of organic carbon remineralization, by introducing oxygen into anoxic sediments and flushing out toxic metabolites (Kristensen 2000).

Burrow ventilation is accomplished through different mechanisms by different types of organisms. Many polychaetes use peristaltic or undulating movements to pump water through their burrow, or use cilia to drive water movement. (Wells and Dales 1951; Riisgård and Larsen 2005). Many animals that ventilate their burrows do so periodically, alternating between periods of active pumping and periods of rest, with the frequency and duration highly species dependent (Kristensen and Kostka 2005). This intermittent ventilation results in periodic oxygenation of the burrow (Boudreau and Marinelli 1994), and oscillating redox conditions within the burrow wall (Volkenborn et al. 2012a, b). Organic matter is remineralized faster under these intermittently oxic conditions than under constantly oxic or anoxic conditions (Aller 1994).

In this study we address how burrower pumping behavior influences the pattern of oxygenation in the burrow, and the flux of oxygen across the burrow walls. We hypothesize that

increases in the rate of pumping will enhance oxygen transport into the sediments, and that the rate of pumping and oxygen transport will vary seasonally due to temperature changes. We chose a common coastal polychaete, *Alitta succinea* (Leuckart 1847; formerly *Nereis succinea*) as our study organism. This species is found in intertidal and subtidal coastal sediments worldwide, and has been recorded occurring in densities up to 1600 m^{-2} (Bartoli et al. 2000). It is thought to be introduced in some locations (Carlton 1979) and its presence has been shown to impact sediment biogeochemistry, including oxygen uptake by sediments and denitrification rates (Bartoli et al. 2000). Like many nereidid polychaetes, *A. succinea* builds burrows with at least two openings and periodically ventilates the burrow by undulating its body, with waves passing from the head towards the tail (Kristensen 1981).

Relatively few studies have measured oxygen levels in burrows, and fewer still have measured oxygen fluxes across the burrow wall (Vopel et al. 2003; Polerecky et al. 2006; Pischedda et al. 2012); most studies measure the temporally and spatially averaged oxygen uptake of bioirrigated sediment. This approach neglects to address the underlying oxygen dynamics over small scales in time and space that drive oxygen fluxes into the sediment. Planar optodes are a relatively new instrument that allow for detailed study of oxygen dynamics in marine sediments, highlighting the spatial heterogeneity of oxygen levels in the burrow (Glud et al. 1996), and have been used to measure oxygen fluxes across burrow walls (Pischedda et al. 2008; Pischedda et al. 2012).

In addition, shallow coastal waters in many regions exhibit high seasonal temperature variability, with temperature affecting the ventilation patterns of many burrowing marine invertebrates (Kristensen 1983; Stanzel and Finelli 2004). Here, we measure pumping behavior and oxygen flux across burrow walls over a range of temperatures, providing insight into how

the link between environmental variables, in this case temperature, and sediment- water fluxes are mediated by burrower behavior.

Within this study we address four questions: (1) How does the oxygen level vary in the burrow water of intermittently pumping *A. succinea*? (2) How does the magnitude of the flux of oxygen across the burrow walls fluctuate over time? (3) Does the volume and velocity of water pumped through the burrow change with temperature variations typically seen across seasons? (4) Do changes in temperature alter these patterns of oxygenation and oxygen flux? This study aims to link the effects of polychaete pumping behavior with sediment oxygen uptake, and the influence of temperature on both.

Materials and methods

Animal and sediment collection

Specimens of *Alitta succinea* were collected from intertidal mudflats on the southern, Atlantic side of the Delmarva Peninsula, VA, USA. Moderately sized (wet weight between 0.05 and 0.2 g) specimens were chosen for experiments. Animals were kept at room temperature in glass aquaria consisting of mudflat sediments overlain with aerated seawater until use. Sediment for use in experiments was collected from Chimney Pole marsh (37° 27' 45.5" N, 75° 42' 58" W), an intertidal mudflat in the same region where animals were collected. Sediments were collected using a corer, from which a subsample was extracted into the experimental aquaria. The natural structure of the sediment was preserved and sediment was not used if macrofauna were present. The porosity of the sediment at Chimney Pole was previously measured as 0.70 ± 0.02 vol/vol (McLoughlin 2011).

Field conditions

Submersible temperature loggers (HOBO Pendant Temperature/Light Logger UA-002; Onset Computer Corporation, Bourne, MA, USA) were deployed in 3 intertidal mudflats similar to that where animals were collected. 3 HOBOS were buried at each location, at 3 cm, 10 cm and 20 cm depth. The temperature within the sediment was measured every 10 minutes for a year, from September 2013 to September 2014. The 20 cm depth HOBO at site 2 stopped recording after Dec 17th, 2013 due to a sensor malfunction. The variance in temperature over different timescales (day, week, and month; Table 1.1) was calculated by dividing the temperature time series from each location at each depth into day-long, week-long and month- long series, then computing the variance for each of these time periods.

Table 1.1. Temperature dynamics within the sediment of intertidal mudflats.

		3 cm depth (N = 3)	**10 cm depth (N = 3)**	**20 cm depth**
Temperature	Mean temp (°C)	16.0 ± 0.1	16.0 ± 0.1	16.0 ± 0.2 (N = 2)
	max temp (°C)	33.9 ± 0.9	30.1 ± 0.4	27.4 ± 0.6 (N = 2)
	min temp (°C)	-2.1 ± 0.6	-0.7 ± 0.3	1.2 ± 0.9 (N = 2)
Variance	Daily timescale	3.1 ± 0.9	0.9 ± 0.2	0.2 ± 0.1 (N = 3)
	Weekly timescale	5.2 ± 1.4	2.4 ± 0.4	1.0 ± 0.2 (N = 3)
	Monthly timescale	9.3 ± 1.5	5.9 ± 0.5	4.2 ± 1.1 (N = 3)

Values are mean ± s.e. N, number of sites measurements were taken at.

A. succinea *abundance*

We determined *A. succinea* population density on two intertidal mudflats on the Delmarva Peninsula similar to those from which animals were collected for the experiment and

temperatures were measured. On each mudflat, one sediment core, 25 cm in diameter and 10 cm deep, was taken approximately every 15 m for 75 m along a transect perpendicular to the water line, providing 5 cores per site. Sediment from the core was sieved through 1 mm mesh and *A. succinea* individuals from each core were counted and killed using carbonated water and wet weight and length were measured.

Oxygen measurement system

We used a planar optode to simultaneously measure oxygen levels within the burrow and in the sediment of the burrow walls with high spatial and temporal resolution over a period of hours, and thus determine how the flux of oxygen into the burrow wall fluctuates over time. Oxygen concentration in a 2- dimensional plane was measured using a planar optode system (PreSens GmbH, Regensburg, Germany) that performs ratiometric luminescence imaging of oxygen. The system consisted of thin, fluorescent, oxygen sensitive foils (SF-RPSu4) and a detector unit (DU01). The foils consist of three layers: (1) An optical isolation layer to prevent color or fluorescent interference from the sample. This layer is 20 - 50 μm thick, oxygen transparent but not reactive, and in direct contact with the sample. (2) An oxygen sensitive layer with the two fluorescing dyes. This layer is 6 - 8 μm thick. (3) A support layer that the oxygen sensitive layer is attached to. This layer is transparent and is attached to the wall of the aquarium. The system is described in Hofmann et al. (2013). The oxygen sensitive layer is coated with two dyes. One dye emits red light with a wavelength that peaks at 650 nm when excited by violet light (400 - 420 nm wavelength), the other dye emits green light that peaks at 510 nm when excited by violet light. Oxygen molecules quench the emission of the red- emitting dye but do not interact with the green- emitting dye. Importantly, the sensors consume no oxygen, can be used repeatedly, and offer long- term stability. The response time of the foils is 30 seconds or

less. Because both large changes in burrow oxygen levels, as well as burrow ventilation activities, occur over several minutes, this response time should be adequate.

The detector unit provides epi- illumination of the foil with blue led lights, and also detects the emitted light with an enhanced color CMOS chip (a type of RGB chip). Images were digitally recorded through a USB connection on a laptop PC as PNG files. The detector unit's sampling rate and exposure settings were controlled by software provided by the company (VisiSens AnalytiCal 1). The exposure was kept constant throughout all recordings.

We performed a two- point calibration for the sensor foil, at 0% O_2 saturation and 100% O_2 saturation. The 0% calibration measured the red: green ratio in anoxic sediment and the 100% saturation calibration measured the red: green ratio in air saturated distilled water mixed with Instant Ocean to a salinity of 35. The average red: green ratio of pixels in a small area in each calibration image was used. The two- point calibration was performed at 6, 24 and 33 °C.

A custom MatLab program (MathWorks Inc., USA) was used to convert RGB images to oxygen concentration. For each image in the recording, the calibration curve was applied to the ratio of red: green in each pixel of the PNG images to calculate the oxygen saturation. We converted air saturation values to O_2 concentration using the solubility of O_2 in water at salinity 35 at the appropriate temperature.

Experimental setup

Experiments were performed in a narrow glass aquarium (20 x 20 x 5 cm) filled with marine sediment to approximately 5 cm from the top, and topped with aerated seawater (Fig. 1.1). The O_2 sensitive foils were 4 x 4 cm squares, but for some experiments these were cut into four 2 x 2 cm squares. The foils were affixed to the inside of the glass aquaria with silicon glue

approximately 5 cm below the surface of the sediment. Foils could be and were reused between experiments, however, if they were damaged during the removal of sediment from the aquaria they were replaced with a new foil. Care was taken during application of the foil to avoid any air bubbles between the foil and the aquarium wall.

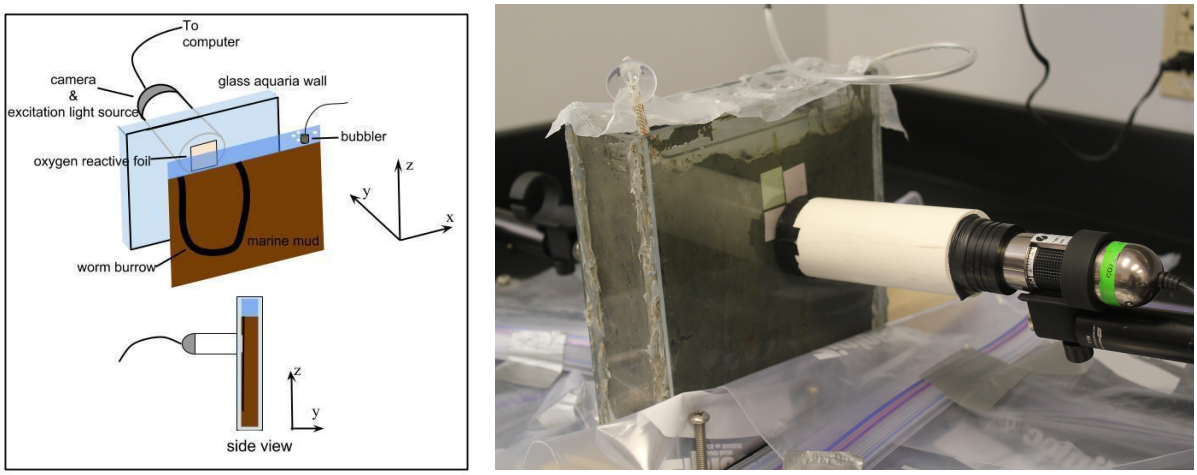

Figure 1.1. (A) Schematic of the Experimental setup. Not to scale. (B) A photograph of the experimental setup. An oxygen sensitive foil was glued to the inside wall of a narrow glass aquaria (20x 20x 5 cm) which was filled with muddy marine sediment with overlying, oxygenated seawater. An *Alitta succinea* individual was placed in the aquaria, and built a burrow along the wall behind the foil. The foil was excited with violet light, and the emission from the foil was recorded with the camera

A worm was introduced to the aquarium after sediment had been inserted, and was allowed to burrow into the sediment near the wall of the aquarium. Likely due to altered mechanical properties at the aquarium wall (Dorgan et al. 2005), worms tended to build burrows up against the aquarium wall. However, when the animal did not construct a burrow behind an oxygen foil new worms were added until one created a burrow behind a foil. Therefore, in some experiments multiple individuals were present in the aquaria prior to recording. This was

unlikely to have any effect on recorded oxygen concentrations because oxygen in burrows only diffuses a few millimeters into the sediment. Each recording was made using the same burrow, under the assumption that animals did not switch burrows.

Once an appropriate burrow had been established behind a foil (i.e. the burrow is bisected by the wall of the aquaria), and the worm began ventilation activity, recording was started. Images were taken every 5 or 15 seconds for 1 to 8 hours using the detector unit. Ambient light between the camera and front of the aquarium was blocked using dark piping. The system was also affixed such that the detector unit was at a constant distance from the foil for all experiments. An example of an oxygenated burrow recorded by the detector unit is given in Figure 2.1A.

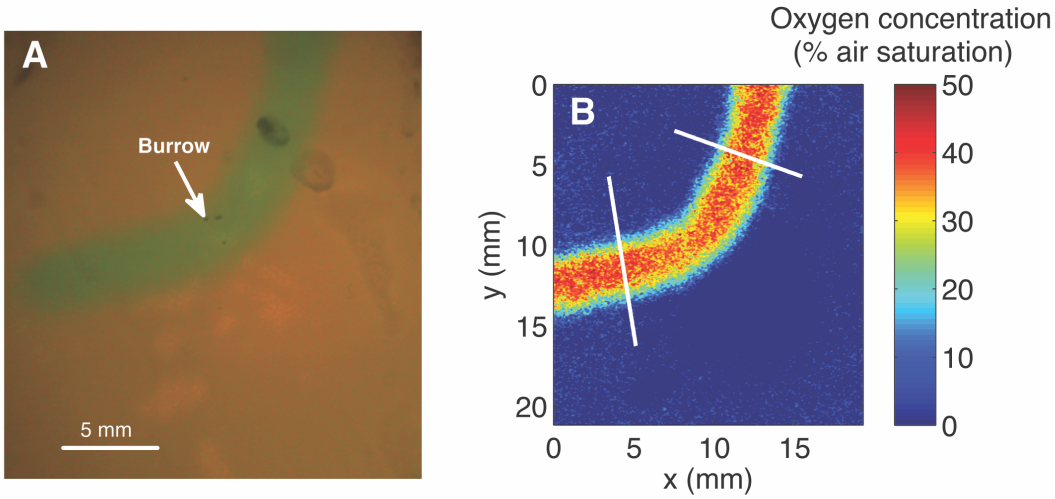

Figure 1.2. Example of oxygen data. (a) Image of oxygenated burrow. The burrow is behind an oxygen- sensitive foil that is illuminated with excitation light of a specific wavelength. The burrow is clearly visible in green due to a high concentration of dissolved oxygen in the burrow water. The porewater of the surrounding sediment is not green because it is oxygen depleted. The scale bar is 5 mm. (b) A calibration curve was applied to every pixel in (a). Warmer colors indicate higher dissolved oxygen levels. The white lines are locations along which oxygen gradients through the burrow and into the burrow wall were calculated

Calculation of oxygen flux

Oxygen profiles within the sediment perpendicular to the burrow wall were used to calculate the flux of oxygen from the burrow across the burrow wall, according to Rasmussen and Jørgensen (1992) and Epping and Helder (1997).

The oxygen consumption rate was assumed the same regardless of distance from the burrow wall, and that it followed zero- order kinetics (Hall et al. 1989). Sediment porosity was assumed constant with distance from the burrow wall. Results of oxygen gradient measurements in *Hediste diversicolor* burrows by Fenchel (1996) support our assumptions. Additionally, he showed that the burrow walls, lined with a thin layer of mucus, did not impede diffusion of oxygen.

With the above assumptions, and neglecting advective transport , the steady state concentration of a solute within the sediment is described by the following equation (Epping and Helder 1997):

$$D_s \frac{\partial^2 C(r)}{\partial r^2} - R = 0 \quad (1.1)$$

where D_s is the porosity corrected diffusivity of oxygen in the sediment; $C(r)$ is the oxygen concentration; r is the radial distance from the burrow wall and R is the oxygen consumption rate. Although this flux is in the radial dimension, we used a planar coordinate system due to the presence of the planar optode. Therefore,

$$C(r) = \frac{R}{2D_s} r^2 + C_1 \mathrm{r} + C_2 \quad (1.2)$$

where C_1 and C_2 are constants. The oxygen gradient within the sediment was selected perpendicular to the burrow wall from the middle of the burrow to beyond where the oxygen concentration dropped to zero within the sediment (Fig. 1.2B). Along this line (1 pixel in width) the oxygen concentration was calculated by applying the calibration curve to the red: green ratio

at each pixel. The sediment- water interface was determined by locating a distinct change in slope along the oxygen gradient, with a steeper slope within the sediment than in the burrow water (Fenchel 1996). The oxygen concentration profile was determined using a running-average of 6 pixels (0.2 mm). To ensure that the middle of the burrow was adjacent to the optode, profiles were only used if a distinct break in the slope of the oxygen concentration at the sediment- water interface within the burrow was observed. In addition, the burrow diameter within optode measurements, with an average of 2.8 + - 0.2 mm, was compared to particle image velocity measurements of excurrent flows obtained at the burrow opening, which had an average burrow openings diameter of 3.2 + - 0.2 mm. This agreement indicated that the optode nearly bisected the burrows for the concentration profiles utilized.

A second order polynomial was fitted to the smoothed oxygen profile within the sediment:

$$C(r) = ar^2 + br + c \qquad (3)$$

where a, b, and c are fitting parameters of the parabola. The flux (J) across the burrow wall (r = 0) was calculated using Fick's Law (Rutgers van der Loeff et al. 1984):

$$J = -D_s b \quad (1.4)$$

The diffusion coefficient of oxygen in the sediment was calculated using the relationship presented in Ullman and Aller (1982)

$$D_s = D\varphi^{m-1} \quad (1.5)$$

where D_s is the diffusivity in sediment, D is the diffusivity of oxygen in water, corrected for temperature and salinity, φ is the porosity, and m is an empirically derived constant. We used a value of 3 for m, which Ullman and Aller (1982) determined for sediments with a porosity of 0.7.

Depth of penetration of the oxygen was calculated by locating the vertex of the parabola fitted to the oxygen concentration gradient. The flux was calculated for 9 line transects across the burrow which were parallel and adjacent to each other. Due to the varying lengths of the burrows which formed along the optode, between two to six sets of transects across each burrow were used to calculate the oxygen flux and penetration depth during each time series (Fig. 2B). Transect locations were chosen where a sufficiently clear sediment- water interface at the burrow wall could be found- indicating that the optode in this location bisected the burrow. The time series flux data at each location was smoothed using a Savitzky-Golay smoothing function and the time series oxygen penetration depth was filtered using a Butterworth filter. An example of each data treatment with raw data is provided in Appendix i. The dominant frequency of burrow oxygenation and oxygen flux oscillations at each temperature was calculated by a fast Fourier transform (FFT) of the time series. Only recordings lasting 4 or more hours were used.

The limitations of the planar optode system in measuring oxygen concentration gradients around cylindrical objects are discussed in Glud (2008). The presence of the planar optode essentially removes sediment that would otherwise consume oxygen, resulting in a small increase in the measured distance of oxygen penetration and decrease in flux versus what would occur without the presence of the optode (Frederiksen and Glud, 2006). In our case, only burrows which were bisected by the optode were used, minimizing this issue, so a correction was not employed (Zhu et al. 2006).

Temperature experiments

Oxygen measurements were taken at 6 °C, 24 °C, and 33 °C, temperatures that are within the seasonal range we observed, with an accuracy of ±1 °C. Animals were first recorded at 24 °C, then 33 °C, and finally 6 °C. Two individuals were recorded at 24 °C after the 33 °C

recording, and the frequency of burrow oxygenation was very similar (within $3.2x10^{-5}$ Hz) before and after the animal was exposed to heat.

All individuals were held at 24 °C for at least 24 hours before recording began. Individuals were not acclimated to the 33 °C and 6 °C temperatures beyond the time it took for the system to reach the desired temperature (approximately 2 hours to reach the cold temperature and 4 hours to reach the hot temperature). We did not observe any mortality from either the high or low temperature experiments. Note that animals were collected during the summer months, when temperatures ranged between 20 and 34 °C temperature tended to oscillate around 25 °C on a 12-hour cycle. Though we examined the effects of biologically relevant temperatures, acclimatization times to the high and low temperatures were much shorter than would occur in the field.

The 33 °C temperature was achieved using a heat lamp located above and to the side of the aquaria. While a uniform temperature was likely not achieved, we ensured that the temperature of the surface water and the sediment to the depth of the foil was at 33 ± 1 °C. The 6 ± 1 °C temperature was achieved by placing the entire setup in a refrigerator.

Ventilation flow measurements

We measured ventilation flow characteristics using a flow visualization technique, particle image velocimetry (PIV) (Adrian 1991), to measure ventilation flow dynamics. The PIV system (described further in Whitman and Reidenbach 2012) consists of a light sheet that is created by shining a laser (Laserglow Technologies© 300 mW, 532 nm) through a convex lens (Melles Griot© 20° convex lens). The light sheet illuminated neutrally buoyant particles (11 micron silver coated hollow glass spheres, Potter Industries©) in the water overlying the sediment. The flow field was imaged with a digital camera (Sony High Definition HC7) for 4

hours at a frame rate of 30 Hz with a spatial resolution of 620 ± 3 pix cm^{-1}. We used a hybrid digital PIV technique (Cowen and Monismith 1997) to calculate a vector field of flow velocity in a 512 pixel high by 256 pixel wide window directly above a burrow entrance. Cross correlation analysis (Sveen 2004) using MatPIV version 1.6.1 resulted in a velocity field with a resolution of 32 x 32 pixels, or 0.52 x 0.52 mm.

To get the frequency of pumping events over the four hours of recording, a velocity field was calculated every 5 seconds and by a fast Fourier transform (FFT) on the average vertical velocity over the burrow. The velocity within the worm burrow was measured as the outflow directly above the burrow entrance. Because laminar flow within a pipe has a parabolic profile across the pipe diameter (Stamhuis and Videler 1998) the flow in the burrow was modeled by fitting a 2^{nd} order polynomial to the velocity profile across the diameter of the burrow entrance at the sediment- water interface. To calculate the tube flow velocity and volumetric flow rate during pumping events, between one and three pumping events were chosen, based upon the orientation of the excurrent flow, and five consecutive instantaneous velocity fields (separated by $1/30^{th}$ of a second) every 90 seconds were calculated. The time average of the five consecutive velocity fields was used to calculate the tube flow parameters. The midline velocity is the apex of the parabola and the mean velocity in the pipe is one half that. The volumetric flow rate is the mean velocity multiplied by the area of the burrow entrance and the total volume pumped during a pumping event is the volumetric flow rate integrated over the pumping event duration.

To avoid wall effects on the outflow velocity due to a burrow opening too close to the wall, we glued a false wall of 0.6 cm thick plexiglass inside the aquarium walls, with the top flush with the sediment surface. This allowed the burrow to be up against the plexiglass false wall while the burrow opening and excurrent jet was kept away from the glass wall. PIV data

could not be collected simultaneously with oxygen data due to interference of the laser used in PIV with the planar optode. Velocity measurements for each individual were recorded at three temperature treatments 9°C, 24°C and 33°C. The low temperature for this experiment was 2- 3°C higher than that used for the oxygen measurements due to equipment constraints, but this did not appear to affect the behavior response.

Statistics

To analyze the effect of temperature on ventilation parameters and burrow oxygenation, we used a 2- way ANOVA testing the effects of individual and temperature. A one- way ANOVA was used to analyze the effect of temperature on the frequency of the oscillation of oxygen flux across the burrow wall. Results are reported as the mean ± 1 standard error, with N as the number of individuals and n as the number of time series analyzed.

Results

Field conditions

While the average temperature was the same at all three sediment depths, shallower depths experienced greater temperature extremes, both high and low. At 3 cm depth, the maximum and minimum recorded temperatures were 33.9 ± 0.9 and -2.1 ± 0.6 °C (number of sites (N) = 3), respectively. The temperatures at 20 cm had very low variance (0.2 ± 0.1 °C) on a 24- hour timescale, whereas the temperature at 3 cm depth had higher variance (3.1 ± 0.9 °C) on a 24- hour timescale. The variance increased, at all depths, when the timescale over which variance was measured increased (Table 1.1, Fig. 1.3).

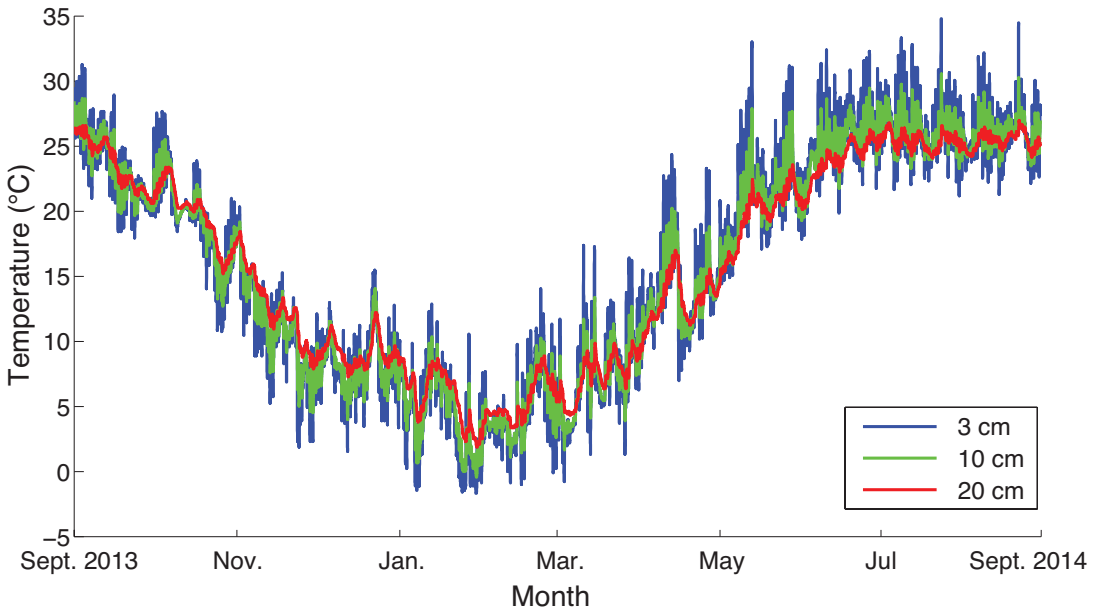

Figure 1.3. A year of temperature measurements from three depths in the sediment of an intertidal mudflat. Data is from September 2013 to September 2014. Temperature series shown are from one location. Temperatures were taken at 3, 10 and 20 cm deep in muddy intertidal sediment similar to where *A. succinea* specimens were collected. Temperatures were recorded every 10 minutes

Alitta succinea *abundance*

The abundance of *A. succinea* individuals was found to be highly variable in intertidal mudflats. There were between 0 and 6 individuals per 0.05 m^2 sediment sample. One mudflat site had an average of 3.8 ± 1.0 individuals per 0.05 m^2 (76 ± 19 ind. m^{-2}) and the other had an average of 0.4 ± 0.4 individuals per 0.05 m^2 (8±8 ind. m^{-2}). The mean wet weight of *A. succinea* individuals was 0.17 ± 0.02 g (N = 18) and the mean length was 4.9 ± 0.4 cm (N = 16).

Ventilation behavior

At all temperatures, active pumping was intermittent, with the frequency of pumping events increasing tenfold from 9 °C to 33 °C (Table 1.2). The time- averaged volumetric flow rate increased with temperature (two-way ANOVA, $F(2,2) = 13.62$; $P = 0.0003$, n = 22, N = 3). During active pumping events, the instantaneous maximum volumetric flow, the volumetric flow rate and the total flow volume, and the duration of pumping events did not exhibit a trend with temperature (Table 1.2, Fig. 1.4). The total flow volume ejected from the burrow during a single period of active ventilation was 24.7 ± 10.2 cm^3 and the average duration of an active ventilation period was 270 ± 33 seconds (Table 1.2). A representative example of the velocity field over a burrow is given in Figure 1.5.

Table 1.2. Burrow ventilation flow velocity and volumetric flow rate during active pumping events. N = 3 individuals, with n being the number of pumping events analyzed. Q is the volumetric flow rate.

	Ventilation periodicity ($x10^{-4}$ Hz)	**Time averaged Q ($cm^3\ hr^{-1}$)**	**Instantaneous maximum Q ($cm^3\ s^{-1}$)**	**Total flow volume during single pumping event (cm^3)**	**Duration of single pumping event (s)**
9 °C (n = 6)	1.8 ± 0.1	101 ± 43	0.16 ± 0.07	18.0 ± 11.0	255 ± 90
24 °C (n = 9)	15.0 ± 2.2	248 ± 22	0.23 ± 0.04	35.7 ± 16.7	296 ± 19
33 °C (n = 7)	18.2 ± 0.7	338 ± 130	0.22 ± 0.06	20.4 ± 4.6	258.9 ± 57.7

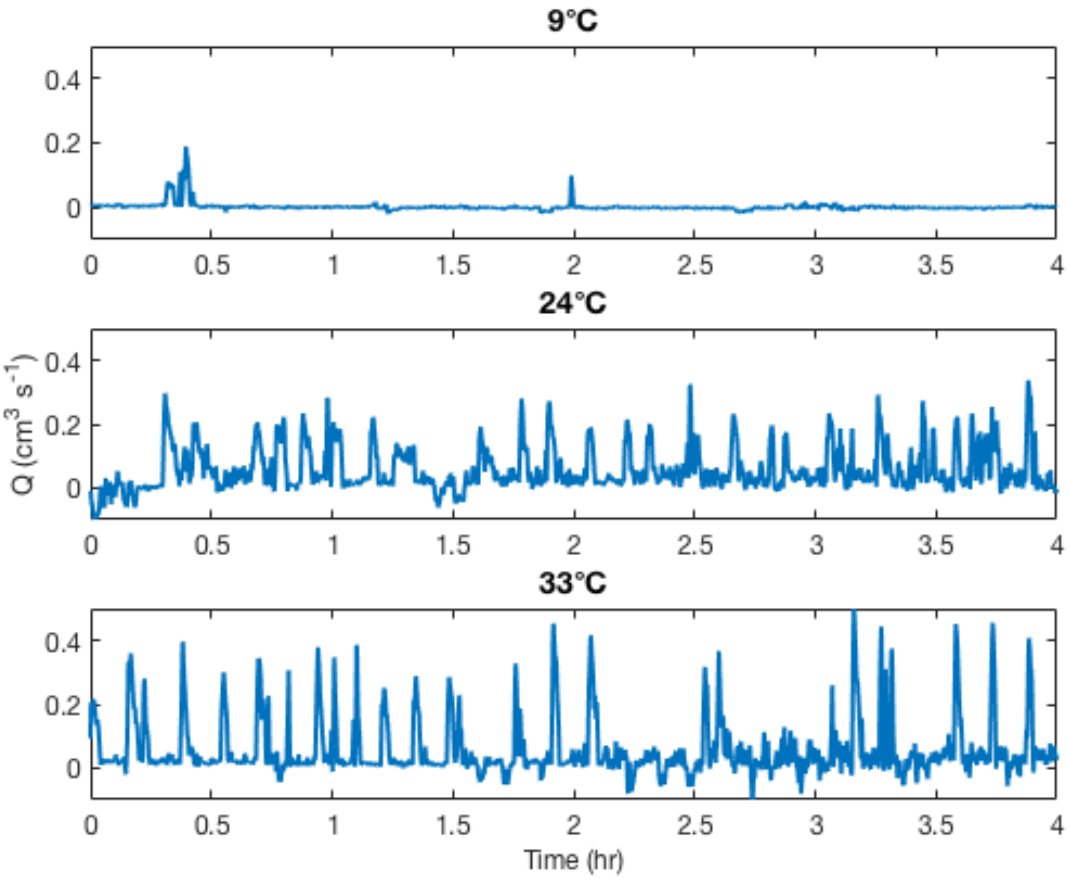

Figure 1.4. Volumetric flow rate (Q) over time, at three temperatures. All data are from one individual. The velocity field from which Q was calculated was measured at a frequency of 30 Hz for the entire 4 hours, and Q was smoothed using a moving average with a winder of 15 seconds

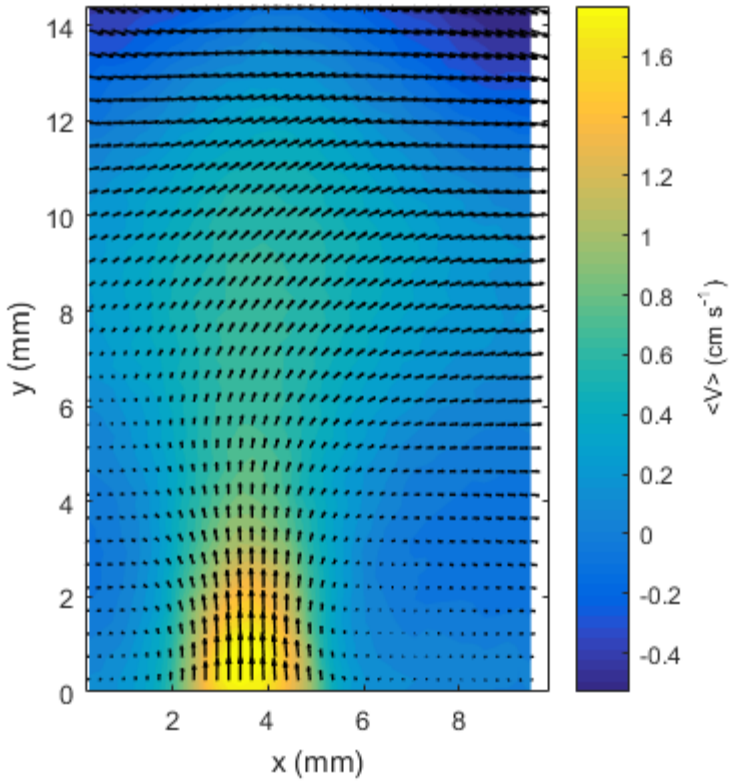

Figure 1.5. Time- averaged vertical velocity (<*V*>) during a single ejection event at 24°C. The length and direction of the arrows are relative to the magnitude and direction of the velocity

Burrow oxygen dynamics

As a result of burrow ventilation, each burrow was periodically flushed with oxygenated surface water, while the surrounding sediment was oxygen- depleted (Fig. 1.2). Burrows contained oxygenated water (defined here as greater than 20% air saturation) for 98 ± 1.3 % of the time at 24 °C and 60 ± 28 and 54 ± 6 % of the time at 6 and 33 °C, respectively. Oxygen levels in the middle of the burrow periodically rose and fell. Burrow oxygenation varied between 80 ± 20 and 150 ± 20 µM (18 ± 3 and 44 ± 5 % air saturation) at 6 °C and 20 ± 3 to 60 ± 2 µM (11 ± 1 to 32 ± 1 % air saturation) at 33 °C. See Appendix ii for burrow oxygenation patterns at

the three temperature treatments. Oxygen levels in the burrow fluctuate periodically as a result of periodic irrigation, with drops in oxygen concentration occurring approximately every 15 to 30 minutes at 24 °C, followed by a steep rise when pumping ensued. Oxygen diffused into the sediment near the burrow wall and was quickly consumed. Oxygen penetration into the burrow wall varied over time (Fig. 1.6), and these fluctuations were damped with distance from the burrow wall (Fig. 1.7). The distance that oxygen diffused into the sediment responded to temperature, with a lower temperature resulting in oxygen transport a greater distance into the sediment (Fig. 8B; Table 1.3; Online Resource 3). This effect was significant (2- way ANOVA, $F(2,3) = 31.45$, $P = 0.0097$, n = 15).

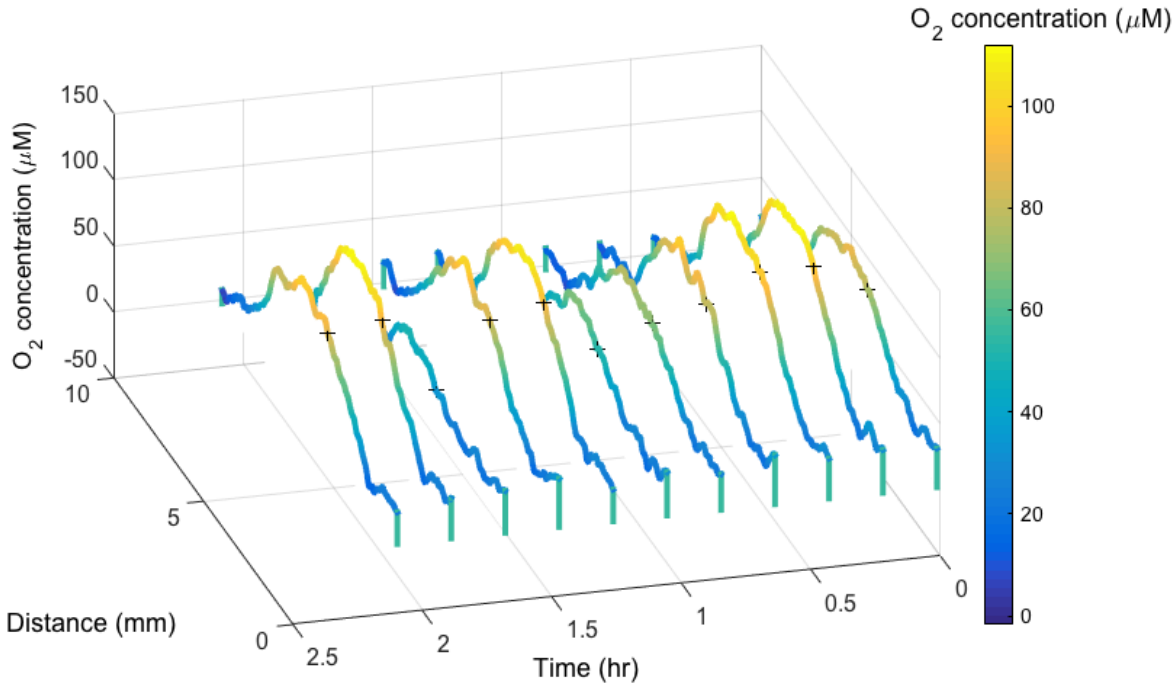

Figure 1.6. Changes in oxygen concentration over time along a transect across a burrow and into the sediment. Concentration profiles are an average of 9 pixels (.28 mm) along the length of the burrow. The profiles were smoothed using a moving average of 13 pixels (.41 mm). The + marks the sediment- water interface at the burrow wall. These measurements were taken at 6 °C

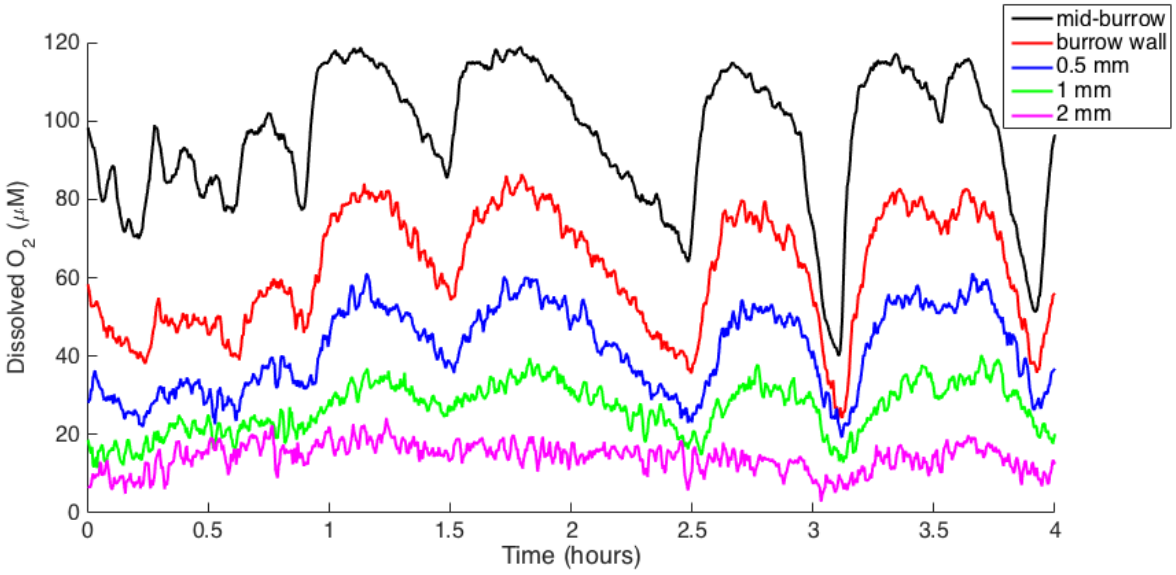

Figure 1.7. Oxygen levels within the sediment at different distances from the burrow wall. Data is from a representative sequence. The black line shows the oxygen concentration in the burrow water. These measurements were taken at 6 °C

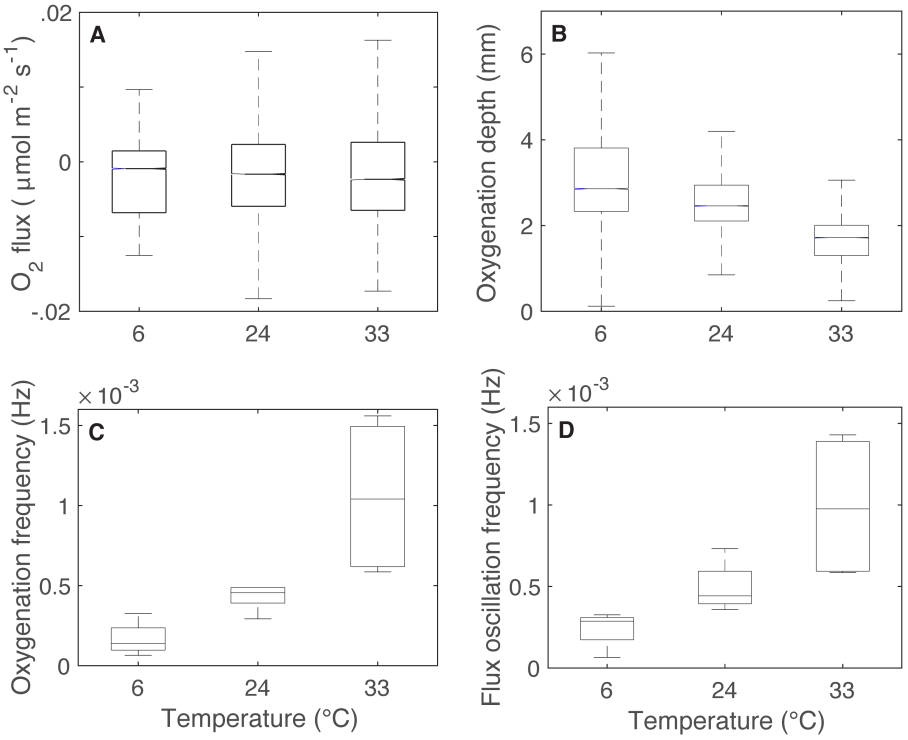

Figure 1.8. Box plots summarizing all measurements of the **(**a) flux, (b) oxygenation distance, (c) oxygenation frequency and (d) oxygen flux oscillation frequency. Flux and oxygenation data was calculated for every frame in every sequence. The total number of hours of oxygen data recorded was 20 h at 6°C, 24.2 h at 24°C and 17.8 h at 33°C. The number of sequences recorded were 4, 6 and 5 for 6°C, 24°C and 33°C, respectively. N = 4 individuals

Table 1.3. Oxygen levels in the sediment adjacent to the burrow walls. Each sequence is an average of measurements taken from between one and six locations along the burrow. There was at least one sequence at each temperature per individual.

	Mean oxygen concentration (µM (% air saturation)) (N=4)			
Distance from burrow wall (mm)	0	0.5	1	2
6 °C (n=4)	72 ± 16 (24±5)	59 ± 13 (19±4)	45±11 (15±4)	22±4 (7±1)
24 °C (n=6)	41±5 (19±2)	29±5 (14±2)	20±4 (9±2)	14±4 (6±2)
33 °C (n=5)	13±5 (7±2)	9±4 (5±2)	5±3 (2±2)	2±2 (1±1)

Values are mean ± s.e. N, the number of individuals; n, the total number of sequences measurements were taken over.

The flux of oxygen into the sediment across the burrow wall also rose and fell periodically, and tended to follow the pattern of oxygenation (Fig. 1.8). The periodicity of burrow oxygenation and the flux across the burrow wall varied with temperature. An increase in temperature resulted in an increase in the frequency of burrow oxygenation and flux oscillations (Fig. 1.9 and Fig. 1.8C and D). The effect of temperature on the frequency of burrow oxygenation was significant (two-way ANOVA, $F(2,3) = 37.15$, $P = 0.0026$, n = 16). The effect of temperature on the frequency of the flux oscillations was significant (one-way ANOVA, $F(2) = 6.91$, $P = 0.0152$, n = 12). However, the average flux across the burrow wall, 1.5 ± 0.3 mmol m^{-2} d^{-1}, did not respond to temperature (two-way ANOVA, $F(2,3) = 1$, $P = 0.46$, n = 15) (Fig. 8A). See Appendix iii for more data on oxygen flux periodicity under the three temperature treatments, as well as flux and oxygenation penetration distance data.

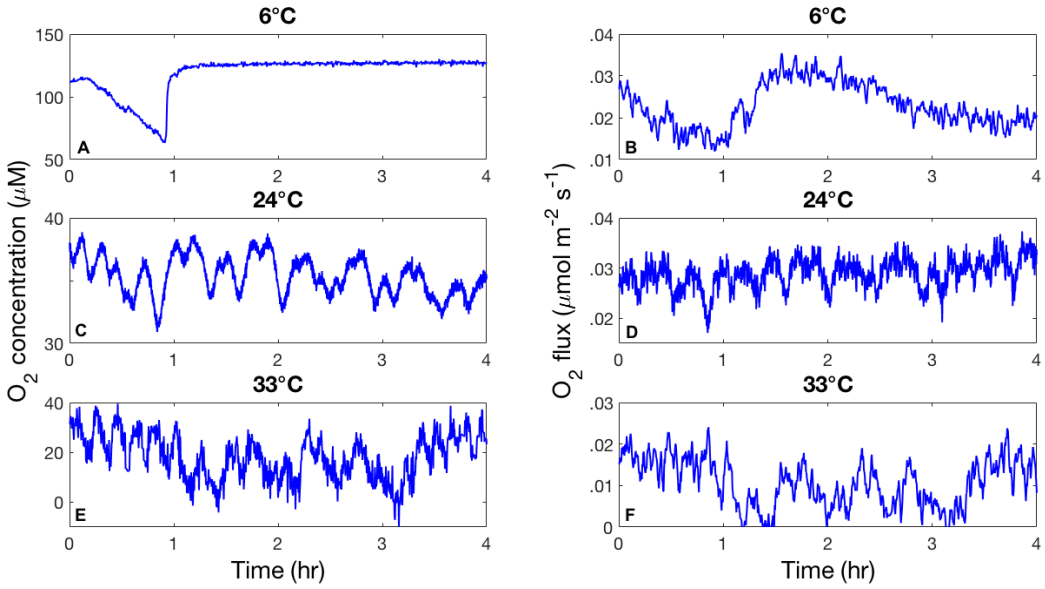

Figure 1.9. Oxygen concentration in the middle of a burrow and the corresponding flux across the burrow wall over time, at three temperatures. All data are from one individual. The frequency of oscillations of the flux conforms to the frequency of burrow oxygenation, and the pattern of

burrow oxygenation changes with temperature. Please note that the y axes limits are inconsistent between panels, in order to highlight the pattern of the fluctuations

Discussion

Burrow oxygenation and oxygen flux

Alitta succinea burrow oxygenation is temporally and spatially heterogeneous due to both ventilation behavior, which controls the temporal patterns of oxygenation, and fluid dynamics within the burrow: Slower- moving fluid is more depleted in oxygen due to microbial consumption at the burrow wall, as well as diffusion into the sediment. During active pumping, the burrow is flushed with oxygenated water. However, the maximum oxygen concentration in the middle of the burrow averaged 44 ± 5 % air saturation, meaning that oxygen levels in the burrow water are depleted within the burrow. This is similar to levels seen in polychaete and bivalve burrows (Volkenborn et al. 2012a; Fenchel 1996).

Our mean oxygen flux value (1.5 mmol m^{-2} d^{-1}) is comparable to values measured in the burrow of another polychaete, *Hediste diversicolor*. Values ranged from 1.92 ± 0.49 to 3.65 ± 0.80 mmol m^{-2} d^{-1} depending on the location in the burrow at which the fluxes were measured (Pischedda et al. 2012). In a separate study, oxygen flux across the burrow walls of *H. diversicolor, Nereis virens*, and *Cyclope neritea*, a bivalve, ranged from 5.2 ± 0.8 to 13.3 ± 3.5 mmol m^{-2} d^{-1}, with similar values in the two polychaete species and higher values in the bivalve burrows (Pischedda et al. 2008). The values for *A. succinea* reported in our study are lower than the values measured for other polychaete species, and may be due in part to shorter pumping durations seen in *A. succinea* (Kristensen 1983), or a result of obstruction of the burrow geometry due to the presence of the optode. Additionally, the maximum fluxes across the

burrow wall measured in our study are 2 to 3 times higher than the average fluxes. This indicates the importance of burrower behavior in controlling the amount of oxygen that is transported into the sediment. The potential flux is higher, but periodic irrigation keeps the oxygen levels in the burrow water and the average flux lower.

The response time of our oxygen sensitive foils, 30 seconds or less, possibly convolutes our periodicity measurements. However, a Welch's power spectral density plot (Welch 1967) of the oxygenation data (a measure of the power of the oxygen signal at different frequencies) indicates a noise floor (where noise dominates the signal) at approximately 2 minutes, meaning that the response time of our foils was at least four times faster than any non- noise fluctuations in oxygen levels. Additionally, the pumping behavior of the worms indicates that changes in ventilation occur on a timescale of minutes, not seconds. For one individual, excurrent velocities were recorded at 30 Hz for a four-hour period across a range of temperatures, and smoothed with a moving average window of 15 seconds (Fig. 1.4). These measurements indicate the oscillations in pumping occur at or slower than one oscillation every 5 minutes. This indicates that the response time of the foils gives a sampling frequency of at least two times, but typically greater, than the highest frequency non- noise fluctuations we see in the oxygen data.

Sediment oxygen uptake

Burrowing macroinfauna, especially those that build and ventilate burrows, greatly increase the oxygen uptake of sediments due to an increase in diffusive flux across the sediment-water interface and, in some cases, pumping induced advective transport into the sediment (Forster et al. 1999; Vopel et al. 2003; Forster and Graf 1995). From our lab observations of a 20 cm deep burrow and, assuming a cylindrical U- shaped burrow with a curvature radius of

approximately 10 cm, *A. succinea* burrows may typically have a length of up to 50 cm. Given measured diameters of 3 mm and abundance data we report in the results (up to 120 ind. m^{-2}), this species increases the area of the sediment- water by up to 57%. Given our idealized *A. succinea* burrow, we estimate the average flux into the sediment per individual burrow to be 7.1 µmol O_2 d^{-1}, and an increase in sediment oxygen uptake of 0.8 mmol O_2 d^{-1} per m^2 of sediment surface due to *A. succinea* ventilation activity. Hume et al. (2011) report a highly variable total oxygen flux into subtidal mudflats ranging from 86.4 to 1010.8 mmol O_2 m^{-2} d^{-1} in a shallow coastal lagoon near our sediment collection and polychaete sampling sites. Assuming similar oxygen uptake in subtidal and intertidal locations, the ventilation activity of this burrower could account for between 1 and 0.1% of the total oxygen uptake in these sediments. This is lower than the fauna- mediated oxygen uptake rates reported in other studies, however this number is highly dependent on burrow size and density of burrows (e.g. *H. diversicolor* burrows contribute between 28 and 92% of the total oxygen uptake at densities of 450 and 600 ind. m^{-2}, respectively (Wenzhöfer and Glud 2004)). Additionally, these studies include the respiration of the worm itself in oxygen uptake measurements, whereas our study only measured oxygen fluxes into the sediment. Far greater densities of *A. succinea* (1200- 1600 ind. m^{-2}) in a coastal lagoon have been reported (Bartoli et al. 2000), where *A. succinea* bioirrigation resulted in sediment oxygen uptake increasing by 31% at a density of 1660 ind. m^{-2}. At an even higher density (3333 ind. m^{-2}) the presence of *A. succinea* increased sediment oxygen uptake from 12.5 to 52 mmol m^{-2} d^{-1} (Bosch et al. 2015). Given our oxygen flux results, this density of polychaetes would result, on average, in an additional flux of 23 mmol O_2 m^{-2} d^{-1} in to the sediment.

Burrow ventilation behavior

As found in previous work (Kristensen 1981), *A. succinea* intermittently ventilate its burrow. As we hypothesized, and similarly to what has been observed for burrowing shrimp (Stanzel and Finelli 2004), the frequency of ventilation increased with temperature, likely due to changes in oxygen uptake in the sediment as well as an increase in *A. succinea* metabolism with temperature (Sturdivant et al. 2015). The increase in ventilation velocity and volumetric flow rate with temperature, reported in this study, is also evident for some species of *Thalassinidea* shrimp (Stanzel and Finelli 2004) and several species of nereidid polychaetes (Kristensen 1983). Because these behavior changes occurred after acute exposure, it is difficult to extrapolate these finding to the field. However, our field temperature data shows fairly large temperature fluctuations over 12 hour timespans (including several instances of an increase of > 8 °C), and we observed no behavior changes over the 4+ hours of data collection at the three temperatures.

Temperature effects on oxygen dynamics

Intertidal organisms in Virginia mudflats experience drastic fluctuations in temperature on tidal and seasonal timescales (Fig. 1.1; Table 1.1). Temperature has been shown to influence the uptake of oxygen by marine sediments, as well as the depth of oxygenation in sediments, with higher oxygen uptake rates at higher temperatures (Hall et al. 1989) and a shallower layer of oxygenated sediment (Glud et al. 2003). Our laboratory measurements indicate that the frequency of the periodic oscillations in the rate of oxygen flux across the burrow walls increased with temperature. We also found that the average and maximum distance of oxygen penetration from the burrow wall decreased with temperature. This signifies that an increase in temperature results in a smaller volume of sediment that experiences oxic conditions. The temperature dependence of oxygenation depth is likely a result of both oxygen in the sediment

being consumed more quickly at a higher temperature (Thamdrup et al. 1998), as well as lower oxygen values within the burrow at these higher temperatures.

The volumetric consumption of oxygen in the sediment (due to both microbial respiration and redox reactions) can be found using the relationship:

$$R = \frac{J^2}{D_s 2 C_0} \qquad (6)$$

where C_0 is the concentration of oxygen at the burrow wall (r = 0) (Rasmussen and Jorgensen 1992). Volumetric oxygen consumption in our study demonstrated a $Q_{10(6\text{-}33°C)}$ value of 1.9 ± 0.2 (N = 4). This is within the range, but at the low end of Q_{10} values (1.5 – 4.3) previously reported in coastal sediments (Thamdrup et al. 1998 and references therein), which may be due to oxygen availability within the burrow (C_0), being mediated by burrower pumping behavior. Decreased oxygen levels within the burrow, due both to decreased solubility as well as altered pumping behavior and increased burrower metabolism, counteract an increase in microbial metabolism within the sediment. Oxygen solubility (at a salinity of 35, oxygen solubility decreases by 40% between 6 and 33 °C. (U.S.G.S. 2011)), rate of diffusion, and consumption by both microbes and redox reactions all change with temperature (Epping and Helder 1997). Thus, the similarity in the magnitude of oxygen fluxes at different temperatures may be because increased oxygen consumption within the sediment at higher temperatures is counteracted by a decrease in oxygen availability within the burrow. This appears to be a result of faster depletion of oxygen within the burrow after the cessation of pumping (Fig. 1.9). The increase in pumping frequency with temperature may be the polychaete attempting to counteract this increased oxygen consumption rate and maintain adequate oxygen levels in the burrow. This may also be compounded by a small decrease in average ventilation duration from the moderate temperature to both the colder and warmer temperatures.

While our results indicate little change in total oxygen flux from worm burrows with temperature, our results suggest a seasonal change in the volume of sediment that experiences oscillating oxygenation conditions due to a burrow. Using the idealized burrow described previously, and the maximum oxygen penetration data we reported, we find that a single burrow would result in a volume of sediment of 26 cm^3 at 33 °C and 90 cm^3 at 6 °C that experiences periodic oxygenation. We would thus expect a maximum of between 3.1 $x10^{-3}$ m^3 and 11 $x10^{-3}$ m^3 of oxygenated sediment due to *A. succinea* burrows per square meter of sediment surface, depending on the temperature.

In conclusion, this study attempts to resolve oxygen dynamics within burrows on small spatial and temporal scales. Periodic burrow ventilation results in similar periodicity in fluxes of oxygen across burrow walls, and the volume of sediment surrounding a burrow that is oxygenated also fluctuates over time. Additionally, the frequency of burrow oxygenation and oxygen flux are temperature dependent, as is the volume of sediment around the burrow that is exposed periodically to oxygen. These results give a detailed understanding of how burrowing organisms mediate the oxygen available to microbes in marine sediment and also show how oxygen availability within sediments surrounding burrows changes with temperature. Here, we show the importance of burrower behavior in linking sediment chemistry with environmental parameters across seasonal timescales.

References

Adrian RJ. 1991. Particle-imaging techniques for experimental fluid mechanics. *Ann Rev Fluid Mech* 23: 261-304

Aller RC. 1994. Bioturbation and remineralization of sedimentary organic matter: effects of redox oscillation. *Chem Geol* 114:331–345

Aller RC, Aller J. 1998. The effect of biogenic irrigation intensity and solute exchange on diagenetic reaction rates in marine sediments. *J Mar Res* 56:905–936

Bartoli M, Nizzoli D, Welsh DT, Viaroli P. 2000. Short-term influence of recolonisation by the polycheate worm *Nereis succinea* on oxygen and nitrogen fluxes and denitrification: a microcosm simulation. *Hydrobiologia* 431:165-174

Bosch JA, Cornwell JC, Kemp WM. 2015. Short-term effects of nereid polychaete size and density on sediment inorganic nitrogen cycling under varying oxygen conditions. *Mar Ecol Prog Ser* 524:155-169

Boudreau BP, Marinelli RL. 1994. A modelling study of discontinuous biological irrigation. *J Mar Res* 52(5):947-968.

Boudreau BP, Jørgensen BB (eds) 2001. The Benthic Boundary Layer: Transport Processes and Biogeochemistry. Oxford University Press, New York

Carlton JT. 1979. Introduced invertebrates of San Francisco Bay. In: Conomos TJ (ed) San Francisco Bay: the urbanized estuary. Pacific Division American Association for the Advancement of Science, San Francisco, p 427-444

Cowen EA, Monismith SG. 1997. A hybrid digital particle tracking velocimetry technique. *Exp Fluids* 22:199−211

D'Andrea AF, DeWitt TH. 2009. Geochemical ecosystem engineering by the mud shrimp *Upogebia pugettensis* (Crustacea: Thalassinidae) in Yaquina Bay, Oregon: Density-dependent effects on organic matter remineralization and nutrient cycling. *Limnol Oceanogr* 54(6):1911-1932

Dorgan KM, Jumars PA, Johnson BD, Boudreau BP, Landis E. 2005. Burrow extension by crack propagation. *Nature* 433:475-475

Dorgan KM, Jumars PA, Johnson BD, Boudreau BP. 2006. Macrofaunal burrowing: The medium is the message. *Oceanogr Mar Biol* 44:85-121

Epping EHG, Helder W. 1997. Oxygen budgets calculated from in situ oxygen microprofiles for Northern Adriatic sediments. *Cont Shelf Res* 17(14):1737-1764

Fenchel T. 1996. Worm burrows and oxic microniches in marine sediments. 1. Spatial and temporal scales *Mar Biol* 127(2):289-295

Forster S, Graf G. 1995. Impact of irrigation on oxygen flux into the sediment: intermittent pumping by *Callianassa subterranea* and "piston-pumping" by *Lanice conchilega*. *Mar Biol* 123(2):335-346

Forster S, Glud RN, Gundersen JK Huettel M. 1999. In situ study of bromide tracer and oxygen flux in coastal sediments. *Estuar Coast Shelf Science* 49(6):813-827

Frederiksen MS, Glud RN. 2006. Oxygen dynamics in the rhizosphere of *Zostera marina*: a two-dimensional planar optode study. *Limnol Oceanogr* 51:1072-1083

Glud RN. 2008. Oxygen dynamics of marine sediments. *Mar Biol Res* 4:243-289

Glud RN, Gundersen JK, Jørgensen BB, Revsbech NP, Schulz HD. 1994. Diffusive and total oxygen uptake of deep-sea sediments in the eastern South Atlantic Ocean: in situ and laboratory measurements. *Deep-Sea Res Part I* 41:1767-1788

Glud RN, Ramsing NB, Gundersen JK, Klimant I. 1996. Planar optrodes: A new tool for fine scale measurements of two-dimensional O_2 distribution in benthic communities. *Mar Ecol Prog Ser* 140: 217-226

Glud RN, Gundersen JK, Roy H, Jørgensen BB. 2003. Seasonal dynamics of benthic O_2 uptake in a semienclosed bay: Importance of diffusion and faunal activity. *Limnol Oceanogr* 48(3):1265-1276

Gundersen JK, Jørgensen BB. 1990. Microstructure of diffusive boundary layers and the oxygen uptake of the sea floor. *Nature* 345:604–607

Hall PO, Anderson LG, van der Loeff, MM, Sundby B, Westerlund SF. 1989. Oxygen uptake kinetics in the benthic boundary layer. *Limnol Oceanogr* 34(4):734-746

Henriksen K, Rasmussen MB, Jensen A. 1983. Effect of bioturbation on microbial nitrogen transformation in the sediment and fluxes of ammonium and nitrate to the overlaying water. *Ecol Bull* 35:193-205

Hofmann J, Meier RJ, Mahnke A, Schatz V, Brackmann F, Trollmann R, Bogdan C, Leibsch G, Wang X, Wolfbeis OS, Jantsch J. 2013. Ratiometric luminescence 2D in vivo imaging and monitoring of mouse skin oxygenation. *Method Appl Fluoresc* 1:045002

Hume A, Berg P, McGlathery KJ. 2011. Dissolved oxygen fluxes and ecosystem metabolism in an eelgrass (*Zostera marina*) meadow measured with the novel eddy correlation technique. *Limnol Oceanogr* 56:86–96

Janssen F, Huettel M, Witte U. 2005. Pore-water advection and solute fluxes in permeable marine sediments (II): Benthic respiration at three sandy sites with different permeabilities (German Bight, North Sea). *Limnol Oceanogr* 50:779-792

Jørgensen BB, Revsbech NP. 1985. Diffusive boundary layers and the oxygen uptake of sediments and detritus. *Mar Ecol Prog Ser* 89:253-267

Karlson K, Hulth S, Ringdahl K, Rosenberg R. 2005. Experimental recolonisation of Baltic Sea reduced sediments: survival of benthic macrofauna and effects on nutrient cycling. *Mar Ecol Prog Ser* 294:35-49

Kristensen E. 1981. Direct measurement of ventilation and oxygen uptake in three species of tubicolous polychaetes (*Nereis* spp.). *J Comp Physiol* 145(1):45-50

Kristensen E. 1983. Ventilation and oxygen uptake by three species of *Neries* (Annelida: Polychaeta). II. Effects of temperature and salinity changes. *Mar Ecol Prog Ser* 12(3):299-306

Kristensen, E. 1985. Oxygen and inorganic nitrogen exchange in a *Nereis virens* (Polychaeta) bioturbated sediment-water system. *J Coast Res* 1:109-116

Kristensen, E. 2000. Organic matter diagenesis at the oxic/anoxic interface in coastal marine sediments, with emphasis on the role of burrowing animals. *Hydrobiologia*. 426(1):1-24

Kristensen, E, Kostka JE. 2005. Macrofaunal burrows and irrigation in marine sediment: Microbiological and biogeochemical interactions. In: Kristensen E, Haese RR, Kostka JE (eds) Interactions between macro- and microorganisms in marine sediments. American Geophysical Union, Washington, D. C., p 125-158

Kristensen E, Penha-Lopes G, Delefosse M, Valdemarsen T, Quintana CO, Banta GT. 2012. What is bioturbation? The need for a precise definition for fauna in aquatic sciences. *Mar Ecol Prog Ser* 446:285-302

McLoughlin SM. 2011. Erosional processes along salt marsh edges on the Eastern Shore of Virginia. Dissertation, University of Virginia, Charlottesville

Meile C, Van Cappellen P. 2003. Global estimates of enhanced solute transport in marine sediments. *Limnol Oceanogr* 48(2):777-786

Papaspyrou S, Gregersen T, Kristensen E, Christensen B, Cox RP. 2006. Microbial reaction rates and bacterial communities in sediment surrounding burrows of two nereidid polychaetes (*Nereis diversicolor* and *N. virens*). *Mar Biol* 148:541-550

Pischedda L, Poggiale JC, Cuny P, Gilbert F. 2008. Imaging oxygen distribution in marine sediments: The importance of bioturbation and sediment heterogeneity. *Acta Biotheor* 56:123-135

Pischedda L, Cuny P, Esteves JL, Poggiale JC, Gilbert F. 2012. Spatial oxygen heterogeneity in a *Hediste diversicolor* irrigated burrow. *Hydrobiologia* 680(1):109-124

Polerecky L, Volkenborn N, Stief P. 2006. High temporal resolution oxygen imaging in bioirrigated sediments. *Environ Sci Technol* 40(18):5763-5769

Rasmussen H, Jørgensen BB. 1992. Microelectrode studies of seasonal oxygen uptake in a coastal sediment: Role of molecular diffusion. *Mar Ecol Prog Ser* 81:289-303

Riisgård HU. 1989. Properties and energy cost of the muscular piston pump in the suspension feeding polychaete *Chaetopterus variopedatus*. *Mar Ecol Prog Ser* 56:157-168

Riisgård HU, Larsen PS. 2005. Water pumping and analysis of flow in burrowing zoobenthos: an overview. *Aquat Ecol* 39(2):237-258

Rutgers van der Loeff MM, Anderson LG, Hall POJ, Iverfeldt A, Josefson AB, Sundby B, Westerlund SFG. 1984. The asphyxiation technique: An approach to distinguishing between molecular diffusion and biologically mediated transport at the sediment-water interface. *Limnol Oceanogr* (29)4:675-686

Smee DL, Weissburg MJ. 2006. Clamming up: Environmental forces diminish the perceptive ability of bivalve prey. *Ecology* 87(6):1587-1598

Stamhuis EJ, Videler JJ. 1998. Burrow ventilation in the tube-dwelling shrimp *Callianassa subterranea* (Decapoda: thalassinidea) II. The flow in the vicinity of the shrimp and the energetic advantages of a laminar non-pulsating ventilation current. *J Exp Biol* 201(14):2159-2170

Stanzel C, Finelli C. 2004. The effects of temperature and salinity on ventilation behavior of two species of ghost shrimp (*Thalassinidea*) from the northern Gulf of Mexico: A laboratory study. *J Exp Mar Biol Ecol* 312(1):19-41

Sturdivant SK, Perchik M, Brill RW, Bushnell PG. 2015. Metabolic response of the Nereid polychaete, *Alitta succinea*, to hypoxia at two different temperatures. *J Exp Mar Biol Ecol* 473:161-168

Sveen JK. 2004. An introduction to MatPIV v. 1.6. 1. Preprint series. Mechanics and Applied Mathematics http://urn. nb. no/URN: NBN: no-23418

Thamdrup B, Hansen JW, Jorgensen BB. 1998. Temperature dependence of aerobic respiration in a coastal sediment. *Microb Ecol* 25:189-200

Ullman WJ, Aller RC. 1982. Diffusion coefficients in nearshore marine sediments. *Limnol Oceanogr* 27: 552-56

Vopel K, Thistle D, Rosenberg R. 2003. Effect of the brittle star *Amphiura filiformis* (Amphiuridae, Echinodermata) on oxygen flux into the sediment. *Limnol Oceanogr* 48:2034-2045

Volkenborn N, Meile C, Polerecky L, Pilditch CA, Norkko A, Norkko J, Hewitt JE, Thrush SF, Wethey DS, Woodin SA. 2012a. Intermittent bioirrigation and oxygen dynamics in permeable sediments: An experimental and modeling study of three tellinid bivalves. *J Mar Res* 70(6):794-823

Volkenborn N, Polerecky L, Wethey DS, DeWitt TH, Woodin SA. 2012b. Hydraulic activities by ghost shrimp *Neotrypaea californiensis* induce oxic-anoxic oscillations in sediments. *Mar Ecol Prog Ser* 455:141-156

Welch P. 1967. The use of fast Fourier transform for the estimation of power spectra: a method based on time averaging over short, modified periodograms. *IEEE Trans Audio Electroacoust* 15:70–73

Wells GP, Dales RP. 1951. Spontaneous activity patterns in animal behaviour: the irrigation of the burrow in the polychaetes *Chaetopterus variopedatus* Renier and *Nereis diversicolor* OF Müller. *J Mar Biol Assoc U. K.* 29(03):661-680

Wenzhöfer F, Glud RN. 2004. Small-scale spatial and temporal variability in coastal benthic O_2 dynamics: Effects of fauna activity. *Limnol Oceanogr* 49(5):1471-1481

Whitman ER, Reidenbach MA. 2012. Benthic flow environments affect recruitment of *Crassostrea virginica* larvae to an intertidal oyster reef. *Mar Ecol Prog Ser* 463:177-191

Wilson WH. 1990. Competition and predation in marine soft-sediment communities. *Annu Rev Ecol Syst* 21:221-241

Zhu Q, Aller RC, Fan Y. 2006. Two-dimensional pH distributions and dynamics in bioturbated marine sediments. *Geochim Cosmochim* 70:4933-4949

Ziebis W, Forster S, Huettel M, Jørgensen BB. 1996. Complex burrows of the mud shrimp *Callianassa truncata* and their geochemical impact in the sea bed. *Nature* 382:619-622

Chapter 2

Pulsatile ventilation flow in polychaete burrows

Elizabeth A. K. Murphy and Matthew A. Reidenbach

Introduction

Because diffusion coefficients in water are orders of magnitude smaller than in air, many aquatic organisms, as well as internal physiological systems, rely on pumps to accomplish advective transport of solutes. Internal biological pumps transport solutes such as oxygen or nutrients throughout the body. Burrow or tube dwelling animals pump fluid through their tubes to transport solutes, and also particles such as plankton for filter feeding, a process referred to as burrow ventilation. Burrow-building organisms are important component of coastal ecosystems. The burrowing and burrow ventilation activities of these organisms alter the chemistry of sediments, transporting oxygen into otherwise anoxic sediments through diffusion across the burrow walls (in cohesive sediments) or advective transport (in permeable sediments). Much of the literature examining tube-dwelling water pumpers focuses on the energetics of filter feeding and the mechanics of particle capture (Riisgård et al. 1992; Riisgård and Larsen 1995; Riisgård 1989; Jørgensen 1986). However, burrow ventilation also occurs for respiratory purposes, and the transport of solutes across the sediment- water interface within the burrow is an important

consequence of burrow ventilation regardless of purpose. Indeed, bioirrigation (the exchange of solutes between porewater and the water column due to burrow ventilation (Kristensen et al. 2012)) is thought to have been critical to stabilizing oxygen cycling and the planet's oxygen reservoir beginning in the early Cambrian (Boyle et al. 2014).

Mechanical forcing of fluid motion through tubes is a ubiquitous biological phenomenon, both externally, such as burrow- dwelling organisms, and internally, such as the circulatory system. Biological pumps occur in many different forms within organisms. Positive displacement pumps generate fluid motion with oscillating pistons, by contracting the walls of a fluid- filled chamber, such as the valve-and-chamber pump of many vertebrate hearts, or by peristaltic waves moving along the tube walls. For the first two types, valves can ensure unidirectionality (Vogel 2007). Peristalsis, such as the waves of contractions driving flow in intestines, or in tunicates (Hennig et al. 1999; Waldrop and Miller 2016), essentially moves the chamber containing the volume of fluid along the tube. Biological pumps can also employ cilia or flagella to drive flow, such as bivalves and sponges, respectively (Larsen and Riisgård 1994; Jørgensen et al. 1988). Burrowers use appendages (e.g. shrimp pleopod beating (Stamhuis and Videler 1998); polychaete parapodia beating (Riisgård 1989)), cilia (polychaetes (Quintana et al. 2011); heart urchin (Hollertz 2002), or muscular body motions, either undulatory (brittle stars (Vopel et al. 2003); polychaetes (Kristensen 1989)) or peristaltic (polychaetes (Riisgård et al. 1996)), to pump water through their burrows. The biological pumps of burrow- dwelling filter feeders tend to operate at low pressures, with high pumping rates and low energy expenditure (Riisgård and Ivarsson 1990). On the other hand, burrowers who ventilate for respiratory purposes operate at higher pressures, with much lower pumping volumes, than filter feeders (Riisgård et al. 1996).

For many species, pumping occurs intermittently, with periods of active burrow ventilation and periods of rest typically occurring on a scale of minutes to tens of minutes (Murphy and Reidenbach 2016; Volkenborn et al. 2012; Riisgård et al. 1992). This intermittency has important consequences for the transport of solutes across the burrow walls (Murphy and Reidenbach 2016). Because undulatory burrow ventilation is characterized as a piston pump (Riisgård and Larsen 1995) (though this is called into question by Vogel (2007), who suggests that the undulatory worm pump, as well as beating appendages, could also act as a peristaltic pump), it is likely that the flow in the burrow is unsteady. However, most studies of the flow dynamics of ventilating zoobenthos do not have high enough temporal resolution of flow data to measure unsteadiness of the flow (Riisgård et al. 1992; Kristensen 1983), or in the case of mud shrimp, find that the flow is steady (Stamhuis and Videler 1998).

On shorter temporal scales, unsteadiness of the flow during active pumping could be important for the energetics of the pump due to viscous interactions between the fluid and the burrow wall, especially at the burrow entrance. Oscillating shear stresses at the burrow wall may have interesting implications for the microbial communities that inhabit sediments, and pressure gradients within the burrow drive percolation into porous sediments, further influencing solute transport- and these parameters could also be altered by unsteady flow dynamics.

Though pressure characteristics, bulk volume flow rates and energetics of burrow ventilation have been reported for various species, because of the opacity of marine sediments, flow data within worm tubes is difficult to come by. Some studies have used artificial tubes, where pumping behavior and flow rate is observed through the walls of a glass or plastic tube, however this method is not particularly realistic and has been shown to alter pumping behavior (Kristensen 1989). Other studies have measured or modeled the flow rate at the burrow entrance

or exit (Murphy and Reidenbach 2016; Jumars 2013). Here, in order to visualize flow within the tube during burrow ventilation we use a transparent mud analog in which a common nereid polychaete, *A. succinea*, readily builds a burrow. Nereid polychaetes are common in coastal sediments, play an important role in nutrient cycling, and some species are an economically important bait fishery. *A. succinea* has been shown to set up oscillating redox conditions near the burrow wall due to ventilation activity (Murphy and Reidenbach 2016). Using simultaneous video recordings of particle movement in the burrow and pumping activity of the worm, we are able to relate the pumping activity to the fluid mechanics in worms of a range of sizes. Specifically, this work addressed the following questions: (1) Is the flow in a piston- pumping polychaete burrow steady or unsteady? (2) How do the pump characteristics and flow characteristics vary with worm size?

Methods

Polychaetes

Alitta succinea specimens and associated sediment were collected from the muddy intertidal zone on the Delmarva Peninsula of Virginia. USA. Animals were kept at room temperature (24 °C) in small plastic tubs filled with mud, overlain with aerated brackish water (10 ppt), until use. Study animals ranged in size from 0.12 g to 1.05 g wet weight.

Mud analog

We developed a transparent sandy mud analog in which our study species, *A. succinea*, readily built tubes. The goal was an optically transparent, non-toxic substrate that worms of a range of sizes would burrow into, and also be able and willing to build a tube. Gelatin is often used in

studies of the kinematics of burrowing by polychaetes (Dorgan et al. 2005; Murphy and Dorgan 2011). However, for this study a substrate with a closer refractive index match to water was desired. Therefore, low density (0.04% by mass) agarose (Sigma Aldrich), an elastic solid, was used, which has a refractive index of 1.3329 (Byron and Variano 2013). Low density agarose is also easily plastically deformed even at low stresses (Normand et al. 2000), so that the small specimens used in this study were able to build permanent burrows. However, smaller worms like the species used here have difficulty burrowing in a pure gelatin or agarose gel, likely due to being unable to generate enough friction to gain a purchase (personal observation; Dorgan 2018). Therefore, to better mimic a sandy mud sediment, we added a relatively transparent granular substance to the agarose to simulate mud with a small amount of granular media. We used Nafion (C. G. Processing, Rockland DE), a recently developed, non-toxic, optically transparent, hydrophilic fluoropolymer with a refractive index, when it has absorbed water by boiling in it, of 1.35 (Leis et al. 2005; Downie et al. 2012). We used granular Nafion, 60-100 mesh (grain size 150 – 250 microns). Agarose gel was prepared by dissolving the agarose powder (4 g agarose per liter of 10 ppt saltwater) over heat. The dissolved agarose was then added to a narrow glass aquaria (20 x 20 x 5 cm), and granular Nafion was added to the solution. The solution was cooled to near room temperature while stirring, then put in a freezer until set and then removed to room temperature until use, within a few hours. The stirring of the agarose solution until setting helped the Nafion to not settle to the bottom of the aquaria before the gel set. Nafion was prepared by first boiling in DI water until optically transparent, then salt water (10 ppt) and baking soda to neutralize it. This is necessary because Nafion is an ion exchange resin, and in contact with salt water, the cations exchange.

Experimental setup

Once the agarose gel was set, overlying saltwater was added and the aquaria brought to room temperature. An *A. succinea* individual was added to the aquaria, and allowed 24 hours to construct a burrow. Particle tracking was used to measure flow velocity in the tube in front of and behind the worm. This system (Fig. 2.1) consisted of a 300 mW green laser beam (532-nm wavelength) (Laserglow Technologies) passed through a convex lens (CVI Melles Griot Inc.), resulting in a thin sheet of laser light. Red fluorescent microsphere particles (peak wavelength 605 nm; fluoresce under 300- 550 nm lasers), 63- 75 microns in diameter, with a density of 0.985- 1.005g/cc (Cospheric) were added to the water and video was recorded at 24 fps using a macro lens on a DSLR camera (Canon Rebel t2i) with a 550 nm long wave pass edge filter (Andover Corp.) affixed to the lens so that only the orange fluorescence from the particles could pass through. Simultaneously, video of the pumping activity of the worm was taken with either a DSLR camera (Nikon) or a video camera (Sony HDR- CX160, Sony Electronics Inc.), both at 24 fps. An example frame and the tracked particles from that sequence are given in Fig. 2.2. Because agarose is not perfectly transparent (Byron and Variano 2013), flow data could only be taken when the burrow was constructed fairly close to the sides of the aquaria.

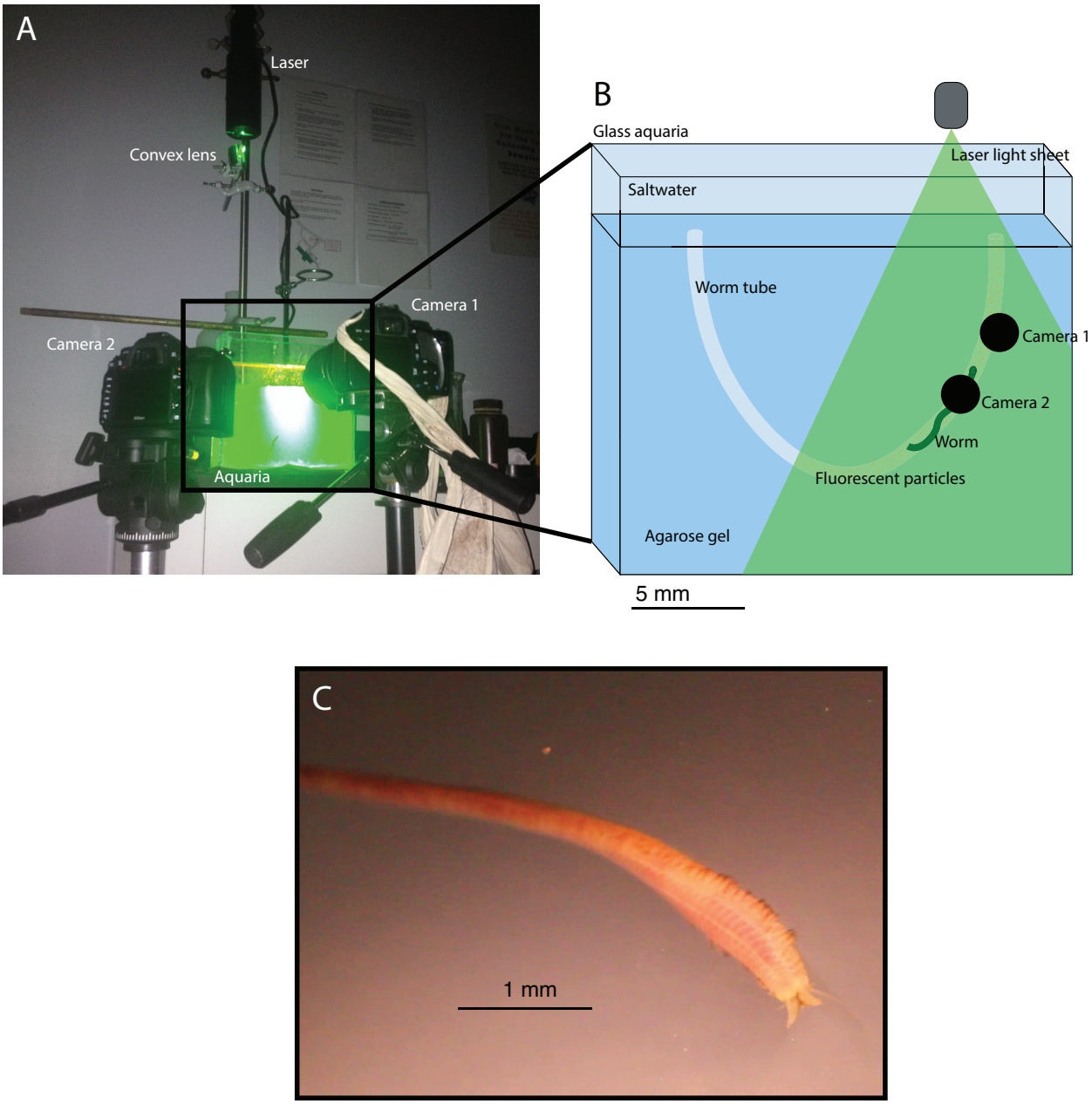

Figure 2.1. (A) Experimental setup. The camera on the right is recording particles in the burrow, and the camera on the left is recording the worm movements lower in the burrow. (B) A schematic of the experimental setup. The aquaria is 20 x 20 x 5 cm. (C) An image of an A. succinea individual burrowing in the agarose mixture. The individual is near the aquaria wall. This image was taken without the laser light sheet for better visibility.

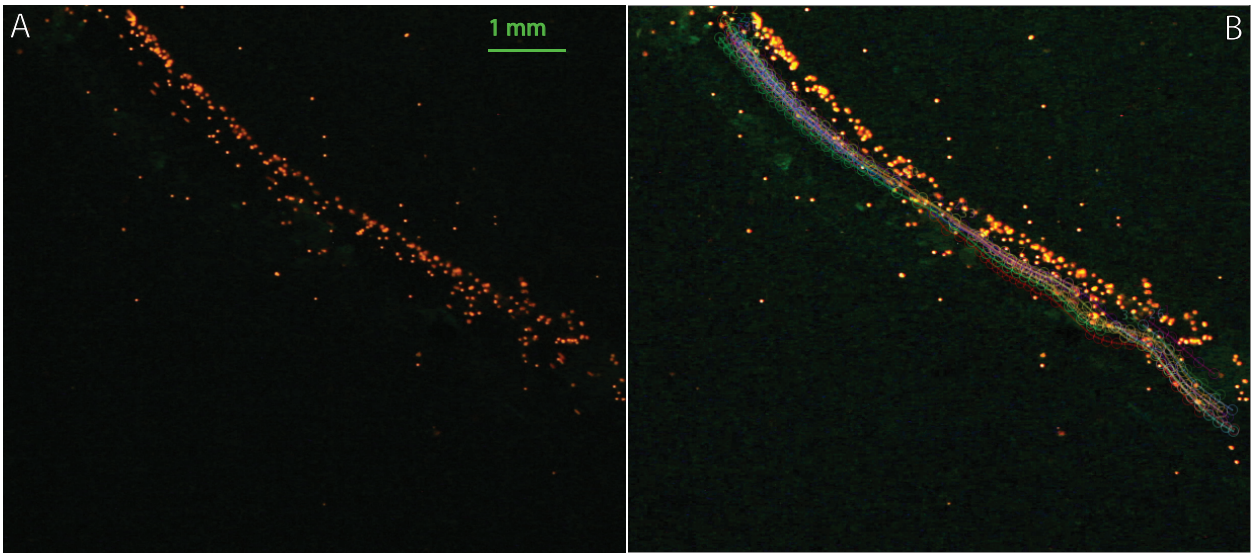

Figure 2.2. A) A still frame from a video of particles being pumped through an *A. succinea* burrow. B) The particle tracks (lines with circles) that were measured to calculate the midline velocity in the burrow over time.

Analysis

Particles in the flow were tracked using ImageJ particle tracking plugin MTrackJ (Meijering et al. 2012). Only particles near the middle of the burrow were tracked (Fig. 2.2), to get the midline velocity in the burrow over time. The average flow in the burrow was estimated as half the midline velocity, which assumes a parabolic flow profile. Where visible, multiple particles were tracked at a given time and the average velocity at that time was taken. The velocity data over time was smoothed using a moving window of 0.2 seconds, and a smoothing spline interpolant was applied to interpolate any missing time slots (where no particles were able to be tracked at that time point). Where possible, video was taken during pumping activity both in front of and behind the worm, however, the shape of the burrow or location of the worm precluded this in some cases. The worm pumping mechanics were determined by measuring the stroke frequency

(strokes per minute), of the pumping activity. Where video was able to be taken of the worm in the lateral orientation to the camera, the peak of the wave passing down the body was tracked through each pump stroke to measure the speed and length of the pump.

Results and Discussion

Worms typically built burrows with two openings. Burrows ranged in size from a diameter of 0.55 to 0.97 mm. We observed that the worms tended to pump with their head near (generally 2- 5 cm from) the burrow entrance and pump water down into that closest tube opening. The inflow of water to the worm pump is clearly pulsatile (Fig. 2.3A). However, once past the worm pump the flow becomes less pulsatile, with lower frequency and less uniform oscillations (Figure 2.3B).

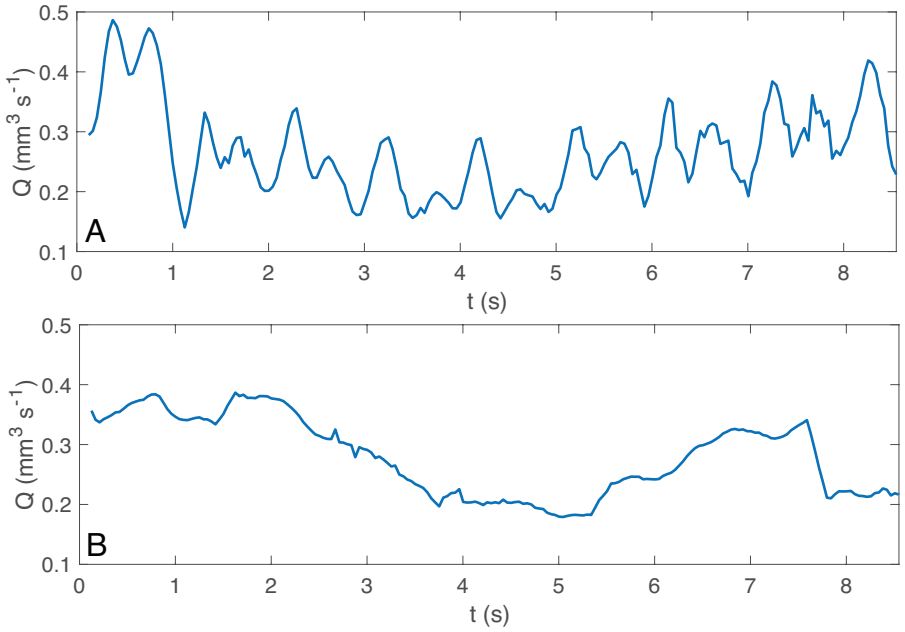

Figure 2.3. Volumetric flow rate in a burrow, near the entrance in front of the worm (A) and behind the worm tail (B). Data is from the same worm and burrow, but taken at different times. Worm was actively pumping during both sequences.

The Reynolds numbers (*Re*) in the tubes fluctuates, but the time- averaged *Re* ranged over a factor of 10, between 0.26 and 2.6 (Table 2.1). The *Re* tended to fluctuate between creeping flow (*Re* < 1) and laminar flow over time in front of the worm pump (Fig. 2.4). Unsurprisingly, the average *Re* of the system increased with increasing worm size (Fig. 2.5). The average flow velocity (*v*) and volumetric flow rate (*Q*) also appear to increase with worm size (Fig. 2.5). However, the frequency of the worm pump did not vary with worm size.

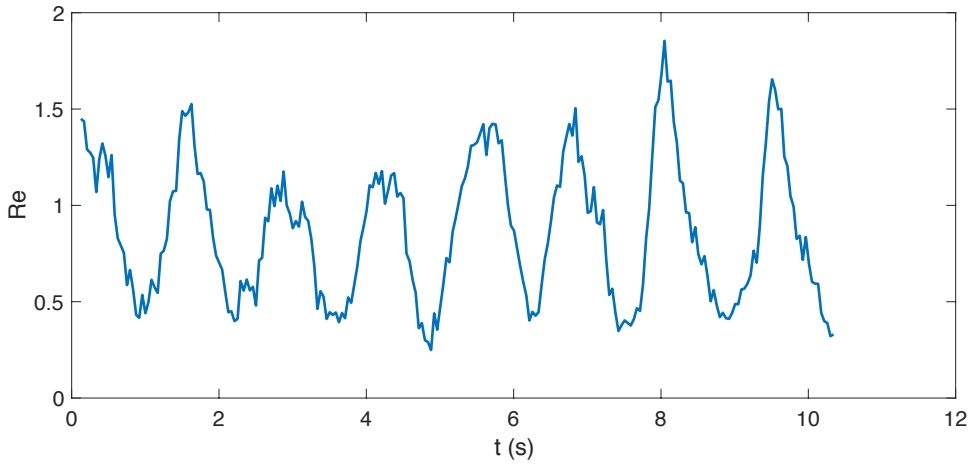

Figure 2.4. An example of Reynolds number (*Re*) fluctuating over time near the entrance to the worm tube.

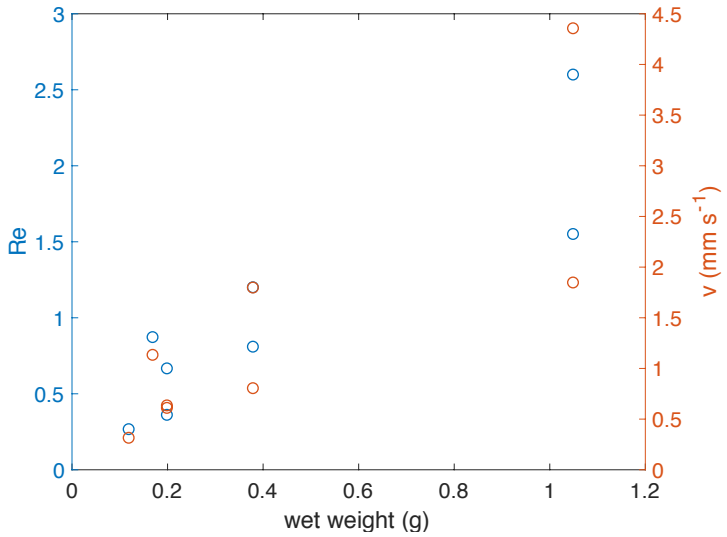

Figure 2.5. The variability of the midline flow velocity (v), and Reynolds number (Re) with worm size (wet weight).

The Womersley number (α) is a measure of the ratio of unsteady inertial forces to viscous forces in pulsatile tubular flow (Womersley 1955)

$$\alpha = r\sqrt{\frac{\omega}{\nu}} \qquad (2.1)$$

where r is the tube radius, ω is the angular frequency of the unsteady flow (where $\omega = 2\pi f_Q$ and f_Q is the frequency of the volumetric flow unsteadiness in Hz), and ν is the kinematic viscosity. The Womersley number is derived from the equation of motion for pulsatile flow driven by an

oscillating pressure gradient. We calculated f_Q by taking a fast Fourier transform (FFT) of the time series. The Womersley number behind the worm pump ranges from 0 (no discernible pulsatile flow) to 0.53 and the Womersley number in front of the worm pump ranges from 0.64 to 1.17, indicating that the flow in the worm tube can either be in a quasi- steady state or the intermediate region (Çarpinlioğlu and Gündoğdu 2001). The variation in the Womersley number does not seem to be driven by the size of the worms (Table 1). In the quasi-steady state, where $\omega < 1$, there is dominance of viscous forces and the pressure oscillations and velocity oscillations are phase matched rather than lagged (Loudon and Tordesillas 1998). The low Womersley numbers here also means that the flow should be parabolic, with steep velocity gradients at the wall, rather than the plug flow which would occur with increased Womersley number (Loudon and Tordesillas 1998). The unsteadiness of the flow entering the burrow could have implications for mass transport across the walls of the burrow, as well as implications for chemoreception by the organism. Higher Womersley number flows result in steeper velocity gradients at the burrow wall, increasing heat and mass transfer. In addition, pulsatile flows can result in discreet odor samples, a strategy used by organisms that "sniff" (Loudon and Tordesillas 1998). Some burrower-dwellers are known to gather chemical information through burrow ventilation (Smee and Weissburg 2006), and flow unsteadiness is thought to be important to the transport of chemical cues (Webster and Weissburg 2009).

Table 2.1. Worm pump and ventilation flow characteristics. * Indicates the individual that had a forked burrow entrance.

Individual	Wet weight *(g)*	Burrow location	Time-averaged *Re*	Time-averaged Q $(mm^3\ s^{-1})$	Q oscillation frequency f_Q *(Hz)*	Pump frequency f_p *(Hz)*	Pump speed $(mm\ s^{-1})$	α
1*	0.2	Near entrance	0.35	0.26	0.80	0.67	2.73	0.64
1*	0.2	Near entrance	0.662	0.30	0.84	0.77	6.75	1.17
2	0.12	Behind worm	0.26	0.08	0	0.77	2.28	0
3	0.17	Near entrance	0.87	0.22	0.75	0.77	-	0.80
4	1.05	Near entrance	1.55	0.44	0.75	0.77	4.93	0.88
4	1.05	Behind worm	2.60	0.52	0.56	0.67	-	0.53
5	0.38	Behind worm	0.81	0.27	0.37	0.96	-	0.74
5	0.38	Near entrance	1.20	0.27	1.03	1.06	-	0.81

In addition, we observed the burrow walls expanding and contracting as the pressure in the tube pulsed with the pumping. Because marine muds are also elastic solids, it is likely that this occurs *in situ* as well, and is another reason using rigid artificial tubes to estimate flow parameters could give erroneous results.

Previous work on polychaete burrow ventilation has measured flow rates and pressure characteristics for peristaltic pumpers *Arenicola marina* (Riisgård et al. 1996), other *Nereid* species (Kristensen et al. 1983), and *Chaetopterus* (Riisgård 1989), all of which are also described as a piston pump, using peristalsis of the body wall, undulatory body waves, or beating parapodia, respectively, to drive the flow in its tube. The worms used in the present study were much smaller than the specimens used in studies of other *Nereid* worm pumps (Riisgård et al. 1992), and there are few flow measurements of flow for zoobenthos of this size (Riisgård 1989; Du Clos and Jiang 2018). For juvenile bivalves, with a similar velocity range and slightly lower *Re* as seen here, the increased resistance to flow of the small diameter of the siphon tube results in greater relative energy expenditure for juvenile clams than adults (Du Clos and Jiang 2018). In the case of the nereid polychaetes investigated here, the relative increase in resistance due to small tube diameter may be more acute due to the unsteadiness of the flow and the length of the worm tube. While we don't have precise measures of the length of tubes built by the individuals in our study, we observed ventilated tubes built to at least 10 cm depth in the aquaria. The power dissipated through viscous interactions a tube have an additional component when the flow is unsteady, resulting in an increase in energy expenditure to power unsteady flow. The unsteady power expenditure is added to the baseline power expenditure of steady flow for the tube. The dissipated power due to unsteady flow ´is given by the following equation (Stamhuis and Videler 1998)

$$P_{unsteady} = \pi D^2 \rho L \overline{U_{osc}}^2 \qquad (2.2)$$

where D is the burrow diameter, ρ is the density of the fluid, $\overline{U_{osc}}$ is the mean of the maximum oscillatory velocity of the flow, and L is the length of the tube. The power dissipated through the burrow due to steady flow, not including entrance effects, is given by

$$P_{steady} = \frac{8\mu L \bar{U}^2}{r^2} \qquad (2.3)$$

where μ is the dynamic viscosity of the fluid. For unsteady flows in the relatively long tubes of *A. succinea*, the additional power expenditure to the flow unsteadiness may be significant. The bigger the amplitude of the imposed velocity oscillation, as well as the bigger the tube diameter, the more of a loss of energy to unsteadiness occurs. Species of burrowing shrimp seem to actively maintain steady flow in the burrow, despite acting as a piston- like pump, possibly to save energy losses due to unsteady flow (Stamhuis and Videler 1998). Bigger burrow diameter and bigger flow speed oscillation amplitude results in greater losses to unsteady flow.

Conclusion

We present a novel method of imaging flow in polychaete worm burrows. We show that, in small Nereid polychaete burrows, flow especially at the burrow entrance is pulsatile. This species does not build a tube that protrudes into the flow, therefore, the burrow entrance acts as a drain flow. Pulsatile flow at the burrow entrance has implications for the energy losses to pipe entry, and therefore the metabolic cost of ventilation (Jumars 2013). Pulsatile flow also alters the dispersion of solutes and particles through the pipe, as well as the diffusion of solutes across the

burrow wall. Future work should examine a wider range of worm sizes in order to estimate the size dependence of pump characteristics and mass transport for this species.

References

Boyle RA, Dahl TW, Dale AW, Shields-Zhou GA, Zhu MY, Brasier MD, Canfield DE, Lenton TM. 2014. Stabilization of the coupled oxygen and phosphorus cycles by the evolution of bioturbation. *Nature Geoscience*. 7(9):671.

Byron ML, Variano EA. 2013. Refractive-index-matched hydrogen materials for measuring flow-structure interactions. *Exp. Fluids*. 54:1456.

Çarpinlioğlu MÖ, Gündoğdu MY. 2001. A critical review on pulsatile pipe flow studies directing towards future research topics. *Flow Measurement and Instrumentation*. 12(3):163-74.

Dorgan KM. 2018. Kinematics of burrowing by peristalsis in granular sands. J. Exp. Biol. 10.1242/jeb.167759

Dorgan KM, Jumars PA, Johnson B, Boudreau BP, Landis E. 2005. Burrowing mechanics: burrow extension by crack propagation. *Nature*. 433(7025):475.

Downie H, Holden N, Otten W, Spiers AJ, Valentine TA, Dupuy LX. 2012. Transparent soil for imaging the rhizosphere. *PLoS One*. 7(9):e44276.

Du Clos KT, Jiang H. 2018. Overcoming hydrodynamic challenges in suspension feeding by juvenile *Mya arenaria* clams. *J Royal Soc Int.* DOI: 10.1098/rsif.2017.0755

Hennig GW, Costa M, Chen BN, Brookes SJ. 1999. Quantitative analysis of peristalsis in the guinea-pig small intestine using spatio-temporal maps. *The Journal of physiology*. 517(2):575-90.

Hollertz K. 2002. Feeding biology and carbon budget of the sediment-burrowing heart urchin *Brissopsis lyrifera* (Echinoidea: Spatangoida). *Marine Biology*. 140(5):959-69.

Jørgensen CB, Famme P, Kristensen HS, Larsen PS, Møhlenberg F, Riisgård HU. 1986. The bivalve pump. *Mar. Ecol. Progr. Ser*. 34:69-77.

Jørgensen CB, Larsen PS, Møhlenberg F, Riisgård HU. 1988. The mussel pump: properties and modelling. *Mar. Ecol. Progr. Ser*. 45:205-216.

Jumars PA. 2013. Boundary-trapped, inhalant siphon and drain flows: Pipe entry revisited numerically. *Limnology and Oceanography: Fluids and Environments*. 3(1):21-39.

Kristensen E. 1983. Ventilation and oxygen uptake in three species of *Nereis* (Annelida: Polychaeta). I. Effects of hypoxia. *Mar. Ecol. Prog. Ser*. 12:289-297.

Kristensen E. 1989. Oxygen and carbon dioxide exchange in the polychaete *Nereis virens*: influence of ventilation activity and starvation. *Marine Biology*. 101(3):381-8.

Kristensen E, Penha-Lopes G, Delefosse M, Valdemarsen T, Quintana CO, Banta GT. 2012. What is bioturbation? The need for a precise definition for fauna in aquatic sciences. *Mar Ecol Prog Ser*. 446:285–302

Larsen PS, Riisgård HU. 1994. The sponge pump. *J Theor. Biol*. 168:53-63.

Leis AP, Schlicher S, Franke H, Strathmann, M. 2005. Optically transparent porous medium for nondestructive studies of microbial biofilm architecture and transport dynamics. *Applied and environmental microbiology*. 71(8), 4801-4808.

Loudon C, Tordesillas A. 1998. The use of the dimensionless Womersley number to characterize the unsteady nature of internal flow. *Journal of theoretical biology*. 191(1):63-78.

Meijering E, Dzyubachyk O, Smal I. 2012. Methods for cell and particle tracking. *Methods in Enzymology*. 504:183-200.

Murphy EAK, Dorgan KM. 2011. Burrow extension with a proboscis: Mechanics of burrowing by the glycerid *Hemipodus simplex*. *J. Exp. Biol*. 214(6):1017-1027.

Murphy EAK, Reidenbach MA. 2016. Oxygen transport in periodically ventilated polychaete burrows. *Mar Biol*. 163: 208. https://doi.org/10.1007/s00227-016-2983-y

Normand V, et al. 2000. New insight into agarose gel mechanical properties. *Biomacromolecules*. 1(4):730–8.

Quintana CO, Hansen T, Delefosse M, Banta G, Kristensen E. 2011. Burrow ventilation and associated porewater irrigation by the polychaete Marenzelleria viridis. *Journal of Experimental Marine Biology and Ecology*. 397(2):179-187.

Riisgård HU. 1989. Properties and energy cost of the muscular piston pump in the suspension feeding polychaete *Chaetopterus variopedatus*. *Mar. Ecol. Progr. Ser.* 56:157-168.

Riisgård HU, Berntsen I, Tarp B. 1996. The lugworm (*Arenicola marina*) pump: characteristics, modelling and energy cost. Marine Ecology Progress Series. 149-56.

Riisgård HU, Ivarsson NM. 1990. The crown-filament pump of the suspension-feeding polychaete *Sabella penicillus*: filtration, effects of temperature, and energy cost. *Mar. Ecol. Progr. Ser*. 62:249-257.

Riisgård HU, Vedel A, Boye H, Larsen PS. 1992. Filter-net structure and pumping activity in the polychaete *Nereis diversicolor*: effects of temperature and pump-modelling. *Mar. Ecol. Progr. Ser.* 83:79-89.

Riisgård HU, Larsen PS. 1995. Filter-feeding in marine macro-invertebrates: Pump characteristics, modelling and energy cost. *Biol. Rev*. 70:67-106.

Smee DL, Weissburg MJ. 2006. Hard clams (*Mercenaria mercenaria*) evaluate predation risk using chemical signals from predators and injured conspecifics. *J. Chem. Ecol*. 32:605-619.

Stamhuis EJ, Videler JJ. 1998. Burrow ventilation in the tube-dwelling shrimp *Callianassa subterranea* (Decapoda: thalassinidea). II. The flow in the vicinity of the shrimp and the energetic advantages of a laminar non-pulsating ventilation current. *J Exp biol.* 201(14):2159-70.

Vogel S. 2007. Living in a physical world X. Pumping fluids through conduits. *Journal of biosciences*. 32(2):207.

Volkenborn N, Meile C, Polerecky L, Pilditch CA, Norkko A, Norkko J, Hewitt JE, Thrush SF, Wethey DS, Woodin SA. 2012. Intermittent bioirrigation and oxygen dynamics in permeable sediments: an experimental and modeling study of three tellinid bivalves. *J Mar Res*. 70(6):794–823

Vopel K, Thistle D, Rosenberg R. 2003. Effect of the brittle star *Amphiura filiformis* (Amphiuridae, Echinodermata) on oxygen flux into the sediment. *Limnology and Oceanography*. (5):2034-45.

Waldrop L, Miller L. 2016. Large-amplitude, short-wave peristalsis and its implications for transport. *Biomechanics and modeling in mechanobiology*. 15(3):629-42.

Webster DR, Weissburg MJ. 2009. The hydrodynamics of chemical cues among aquatic organisms. *Annu. Rev. Fluid Mech*. 41:73-90.

Womersley JR. 1955. Method for the calculation of velocity, rate of flow and viscous drag in arteries when the pressure gradient is known. *The Journal of physiology*. 127(3):553-63.

Chapter 3

Roughness effects of diatomaceous slime fouling on turbulent boundary layer hydrodynamics

Note: Preliminary results from this chapter were published as a refereed conference paper for the 10th International Symposium on Turbulent Shear Flow Phenomenon. The citation is: Murphy EAK, Barros JM, Schultz MP, Flack KA, Steppe CN, Reidenbach MA. The turbulent boundary layer structure over diatomaceous slime fouling. *Tenth International Symposium on Turbulence and Shear Flow Phenomena*. Chicago, IL.

An extended journal article has been submitted to the journal *Biofouling*, and is currently in revision.

Elizabeth A. K. Murphy[1], Julio M. Barros[2+], Michael P. Schultz[3], Karen A. Flack[2], Cecily N. Steppe[4], Matthew A. Reidenbach[1]

[+] Current affiliation Fluid Mechanics Unit, Okinawa Institute of Science and Technology, 1919-1 Tancha, Onna-son, Kunigami-gun, Okinawa, Japan 904-0495, juliomanuel.barrosjunior@oist.jp

[1]Department of Environmental Sciences, University of Virginia, 291 McCormick Rd, Charlottesville, Virginia, 22903, USA, 925-330-2992, eam6vf@virginia.edu

[2]Department of Mechanical Engineering, United States Naval Academy, 590 Holloway Road, Annapolis, Maryland, 21402, USA, 410-293-6440, 410-293-6500, julio.barros.br@usna.edu

[3]Department of Naval Architecture and Ocean Engineering, United States Naval Academy, 590 Holloway Road, Annapolis, Maryland, 21402, USA, 410-293-6440, mschultz@usna.edu

[2]Department of Mechanical Engineering, United States Naval Academy, 590 Holloway Road, Annapolis, Maryland, 21402, USA, 410-293-6501, flack@usna.edu

[4]Department of Oceanography, United States Naval Academy, 572C Holloway Rd, Annapolis, Maryland, 21402, USA, 410-293-6552, natunewi@usna.edu

[1]Department of Environmental Sciences, University of Virginia, 291 McCormick Rd, Charlottesville, Virginia, 22903, USA, 434-243-4937, reidenbach@virginia.edu

Abstract

Biofilm fouling significantly impacts ship performance. Here, the impact of biofilm on boundary layer structure at a ship-relevant, moderate Reynolds number is investigated. Boundary layer measurements were performed over slime-fouled plates using high resolution particle image velocimetry (PIV). The velocity profile over the biofilm shows a downward shift in the log-law region (ΔU^+), resulting in an effective roughness height (k_s) of 8.8 mm, significantly larger than the physical thickness of the biofilm (1.7 ± 0.5 mm) and generating more than three times as much frictional drag as the smooth-wall. The skin-friction coefficient, C_f, of the biofilm is 9.0×10^{-3} compared with 2.9×10^{-3} for the smooth wall. The biofilm also enhances turbulent kinetic energy (*tke*) and Reynolds shear stress, which are more heterogeneous in the streamwise direction than smooth-wall flows. This suggests that biofilms increase drag due to high levels of momentum transport, likely resulting from protruding streamers and surface compliance.

Introduction

Many biological surfaces are rough, and man-made surfaces, such as ship hulls and tidal turbine blades, often become rough due to biological activity, such as the attachment and growth of organisms (biofouling). This roughness typically reduces the performance of these engineered systems (Townsin 2003; Walker et al. 2013a). Surface roughness due to biofouling on ship hulls

has major economic consequences for shipping and Naval activities. For example, for a single class of mid-sized surface vessels alone, biofouling costs the U.S. Navy an estimated $56 million per year due to increased fuel consumption and expenses associated with cleaning and painting the hull (Schultz et al. 2011). Fouling-release and antifouling hull coatings can help control hard fouling, such as barnacles. However, these coatings are often ineffective at preventing slime fouling (Molino and Wetherbee 2008).

The primary biofouling community seen on Navy vessels is biofilm fouling (Schultz et al. 2015). This thin soft-fouling community, also called slime, is found on most aquatic surfaces and tends to be one of the first types of fouling to occur. Biofilms are composed of bacterial or algal cells embedded in viscoelastic extracellular polymeric substances (EPS) (Stoodley et al. 1999), and biofilms found on ship hulls are often composed primarily of diatoms (Zargiel et al. 2011). The species assembly composing a biofilm, as well as the hydrodynamic regime in which it grows, determines a biofilm's physical structure. Diverse biofilm species have distinctive cell surface properties (i.e. hydrophobicity or hydrophilicity) that may influence how the structures interact with the flow within the turbulent boundary layer above the biofilm (de Beer and Kühl 2001). Biofilm thicknesses range from micrometers to centimeters, and the structure of biofilms is highly heterogeneous, often composed of bulbous cell clusters between which are voids that permit fluid flow (de Beer at al. 1996). When grown under shear, biofilms form thin, flexible streamers that protrude from the surface (Taherzadeh et al. 2009).

The Naval Ships' Technical Manual (U.S. Navy 2006) assumes that soft fouling, such as biofilm growth, results in minimal reduction in ship performance. Therefore, soft fouling found during a hull inspection is not considered reason to clean the hull. However, recent work shows that although biofilms typically have low vertical relief and are compliant, biofilm fouling can

induce a steep drag penalty on fouled surfaces. For example, Schultz et al. (2015) indicates that slime fouling can increase the skin friction up to 70% in a laboratory-scale turbulent channel flow. This corresponds to about a 10% increase in required propulsive power for a mid-sized naval surface combatant at cruising speed. Field and laboratory trials indicate that slime on ship hulls significantly increases the resistance and power requirements of the vessel (Schultz 2007; Haslbeck and Bohlander 1992). Therefore, it is important to understand the interactions between biofilms and boundary layer flow in order to better assess the impacts of slime fouling on ship performance.

Fouling affects ship performance by increasing the roughness of the hull surface. Most studies of the effects of roughness on the turbulent boundary layer focus on rigid roughness elements, often with regular spacing (Krogstad and Antonia 1999; Flack et al. 2005; Flack and Schultz 2010). However, in biological systems, compliance and irregularity are the norm. Under some wall boundary conditions, a compliant surface can decrease skin friction by lessening the intensity of turbulence near the wall and reducing the amount of energy carried in streamwise vortices (Xu et al. 2003). Some studies of biofilms and other types of algal growth on already-rough surfaces such as coral reefs or pebble beds, show a reduction of surface roughness as well as a decrease in bed shear stresses compared to the bare roughness elements because the biofilm growth effectively smooths out the surface (Graba et al. 2010; Nikora et al. 2002; Stocking et al. 2016). However, direct measurements show that biofilms can also increase skin friction when they grow on smoother surfaces, such as ship hulls, and analysis of the mean velocity profile over biofilms shows that the effective roughness height (k_s) of the fouled surface can be significantly greater than the physical height of the biofilm itself (Walker et al. 2013b). The effective roughness height is a measure of the magnitude of the roughness effect on the boundary

layer, in terms of the diameter of close-packed sand grains that would result in the equivalent momentum extraction from the flow (Nikuradse 1933).

Given that biofilms can show a large increase in skin friction despite a small physical roughness height, this study examines the spatially explicit effects of a biofilm on the friction velocity, turbulent kinetic energy, instantaneous momentum transport, vortical motion, and coherent structures within the turbulent boundary layer. The goal of this work is to investigate how biofilm fouling alters the turbulent boundary layer and to better understand why biofilms induce such steep drag penalties. In order to assess both the average velocity field over a biofilm as well as the heterogeneous nature of turbulence parameters over a natural living surface, high resolution 2-D particle image velocimetry (PIV) measurements were obtained in the boundary layer of a moderate Reynolds number flow. Preliminary results from this study were presented in Murphy et al. (2017). The results presented are for a large, uniformly-fouled plate with relatively thick biofilm fouling. Both the velocity field throughout the boundary layer, and the spatially-resolved generation of turbulent and shear stresses are measured, and therefore provide insights into the interactions of biofilms with turbulent boundary layer flow.

Materials and Methods

Biofilm and Facilities

A dynamic slime exposure facility, described in Schultz et al. (2015), was used to grow biofilm on large (0.20 m x 1.52 m) acrylic plates affixed to the outside of a rotating drum submerged in brackish water with a salinity of 18 ppt. The drum rotated at 60 *rpm*, creating a peripheral velocity of 1.9 ms^{-1}, so that biofilm growth occurred under shear. The biofilm consisted of four genera of diatoms (*Amphora*, *Achnanthes*, *Entomoneis* and *Navicula*) that are

commonly found on ships, and are also found on antifouling and fouling-release coatings that have been exposed to the marine environment under dynamic conditions (Schultz et al. 2015; Zargiel et al. 2011). The tested fouled plate was exposed in the dynamic slime facility for 10 weeks and had a fairly uniform layer of biofilm that averaged 1.7 ± 0.5 mm thick with a mean peak-to-trough distance of 0.5 mm. The biofilm thickness measurements were made on the wet biofilm in air using a wet film thickness paint gauge, as outlined in Schultz et al. 2015. An image of the biofilm used in this study is given in Fig. 3.1A.

Testing was performed in a recirculating tunnel facility in the United States Naval Academy Hydromechanics Laboratory (Fig. 3.1B). The flow enters the test section through several flow-conditioning devices: a contraction, mesh screens and a honeycomb flow straightener. The freestream turbulence in this facility is less than 0.5% (Volino et al. 2007). The test section of the tunnel is 0.2 m x 0.1 m, with a length of 2 m. The adjustable top wall of the tunnel was set to provide a zero-pressure gradient flow during testing. The free stream velocity was 1.1 ms^{-1}.

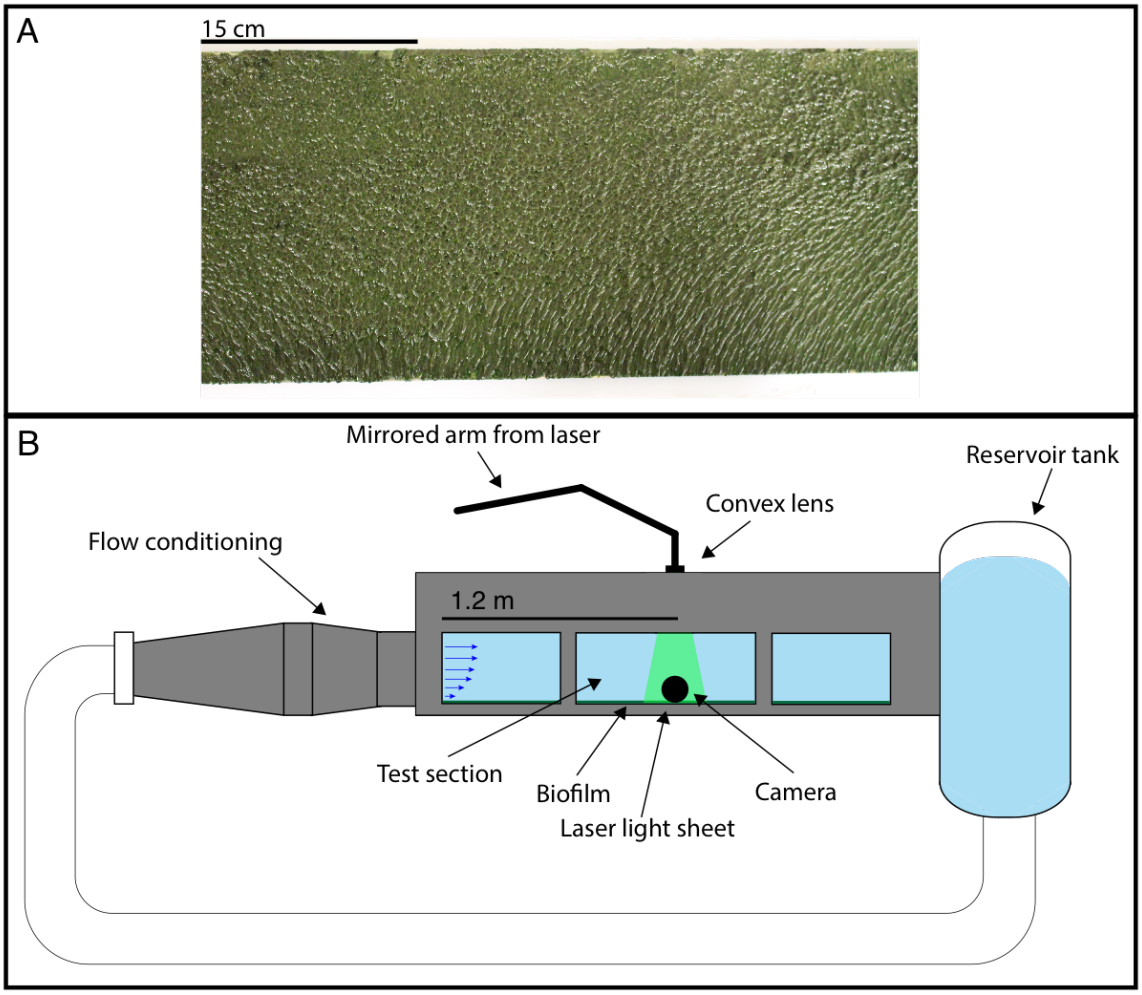

Figure 3.1. (A) A portion of the fouled acrylic plate used in this study, photographed in air and (B) a schematic of the tunnel flow facility, not to scale.

Particle image velocimetry (PIV) was used to capture the flow field in the streamwise - wall-normal $(\boldsymbol{x}-\boldsymbol{y})$ plane. The system consisted of one $6.6k \times 4.4k$ pixels 12 bit frame straddle CCD camera (TSI 29MP) coupled with a 190 mJ per pulse, dual-cavity pulsed Nd:YAG laser (Quantel). A 0.3 mm thick laser lightsheet was formed by a spherical-cylindrical lens configuration. The flow was seeded with 2 μm silver coated glass-sphere particles, and all measurements were performed ~1.22 m downstream of the boundary layer trip, and ~0.42 m

downstream of the leading edge of the fouled plate. The time-delay, *dt*, between the image-pairs was 250 μs. The time-delayed images were interrogated using a recursive two-frame cross-correlation methodology, with a final pass of 32^2 pixels with 50% overlap to satisfy the Nyquist sampling criterion (Insight 4G version 11). Statistical validation tools were employed to identify and replace erroneous vectors, including the replacement with displacement assessed from secondary peaks from the correlation map identified during the interrogation process. All instantaneous fields were then low-pass filtered with a narrow Gaussian filter to remove high-frequency noise. On average, between 1% and 2% of the velocity vectors were erroneous and therefore removed and interpolated across. A total of 4000 statistically independent instantaneous velocity fields were acquired. The field-of-view (FOV) was $2.4\delta \times 1.4\delta$ (δ is the boundary layer thickness) and the final grid resolution was 176 μm, allowing for 406 vertical velocity profiles in each frame, with between 262 and 264 velocity vectors per profile, depending on the height of the biofilm at that location. The boundary layer thickness, δ, was measured from the lowest point of the biofilm in the PIV frame to the point with a mean velocity of 99% of the freestream value.

Additionally, smooth-wall boundary layer data over a non-fouled acrylic plate were taken in the same facility as the biofilm data and used for comparison in this study. Flow parameters for the smooth wall and slime-fouled wall are given in Table 3.1. Spatially explicit smooth-wall data are from PIV analysis as described above, with a $2.3\delta \times 1.5\delta$ window. The spatial resolution of the smooth-wall PIV vector data was 144 μm. For comparison, a smooth-wall mean velocity profile was taken using laser Doppler velocimetry (LDV) at the same location as PIV measurements. The LDV setup was similar to that described in Schultz and Flack (2007).

Table 3.1. Roughness parameters of the biofilm-fouled plate and the smooth plate. δ^+ is the friction Reynold number.

	U_e (m s^{-1})	δ (mm)	$Re_\tau = \delta^+ = \delta U_\tau/\nu$	U_τ (m s^{-1})	ΔU^+	k_s^+	k_s (mm)	C_f
Smooth	1.2	33.5	1.64×10^3	0.047	-	-	-	2.9×10^{-3}
Biofilm	1.1	30.0	2.5×10^3	0.076	12.8	736	8.8	9.0×10^{-3}

Two potential experimental problems should be addressed. First, the direction of flow during testing was perpendicular to the direction of flow during growth of the biofilms. Potentially, this results in streamers with a different morphology or mechanical properties than they would otherwise have. However, this may not be much divorced from real world scenarios of biofilm growth, which often occurs when a ship is in port, where water motion due to waves and currents also does not necessarily have the same direction as the ship's movement underway. Additionally, testing was performed in fresh water, whereas biofilms were grown in brackish water (18 ppt). This may have resulted in some structural changes of the EPS, and death of the biofilm over the course of the experiment. One function of EPS is to protect cells from ionic changes (Decho 1990), potentially lessening the shock of the fresh water.

Mean Velocity Profile Analysis

The log-law equation for flow over a smooth wall,

$$U^+ = \frac{1}{\kappa}\ln(y^+) + C \qquad (3.1)$$

describes the mean boundary layer velocity profile in the log region above the bed. Here, the + superscript indicates that the term is normalized by inner units (U_τ or $\frac{\nu}{U_\tau}$). Both C and κ are

empirically derived universal constants. *C* is the log-law intercept for the smooth wall, here set to 5, and κ is the von Kármán constant, set to 0.41; this is the pair of values used by Volino et al. (2011). The structure of flow over a rough wall is altered, with the addition of a wall datum offset (ε) and the roughness function (ΔU^+), so that the flow in the log-region of a rough wall boundary layer is described by

$$U^+ = \frac{1}{\kappa}\ln(y+\varepsilon)^+ + C - \Delta U^+ \qquad (3.2)$$

where ΔU^+ represents the downward shift of the velocity profile in the log-law region (also called the roughness function), and ε is the vertical displacement of the virtual origin. A note on nomenclature and the rough wall log-law equations can be found in Appendix iv. The addition of these two variables complicates finding the friction velocity, U_τ. Typically, an iterative procedure is used to adjust the values of U_τ and ε until the slope matches that of the smooth wall (Perry and Li 1990). The boundary layer velocity profile in the outer region of the boundary layer can be described in the velocity defect form,

$$U_e^+ - U^+ = -\frac{1}{\kappa}\ln\left(\frac{y+\varepsilon}{\delta}\right) + \frac{2\Pi}{\kappa}w(y/\delta) \qquad (3.3)$$

where $\frac{2\Pi}{k}w(y/\delta)$ is the Coles wake function (Coles 1956), $\prod$ is the wake parameter, and *w* the wake function, which describes the departure of the mean velocity from the log-law in the outer layer. The wake function should be similar between the biofilm and the smooth wall, because the height of the biofilm is small compared to the thickness of the boundary layer (Jiménez 2004;

Flack et al. 2007); in the present study k/δ = 1/60 (using the mean peak-to-trough distance of the biofilm for k). Additionally, Walker et al. (2013b) found outer layer similarity over freshwater biofilm. Therefore, velocity defect similarity between the biofilm surface and a smooth wall was assumed in the present study (Flack et al. 2005, Castro 2007). A goodness-of-fit maximization scheme between the biofilm velocity defect profile and the smooth-wall velocity defect profile was used to calculate U_τ and ε over the biofilm surface. To accomplish this, values of U_τ and ε in equation 3 were independently adjusted, and the combination resulting in the best fit between the biofilm and smooth wall profile was found. Finally, ΔU^+ was calculated by finding the value that resulted in the best match between the log and wake regions of the biofilm and smooth wall mean velocity profiles plotted in inner units. Because the biofilm is permeable, the initial origin was set at 0.5 mm below the bottom of the lowest trough of the biofilm in the PIV frame.

A modified Clauser chart method (as described in Schultz and Flack (2007)) was used to validate the velocity defect matching method (described above) for calculating the wall shear stress. The modified Clauser chart method uses an iterative procedure to calculate U_τ by iteratively shifting ε and ΔU^+, finding the best C_f, and repeating until optimized. The U_τ values for the mean velocity profile calculated by the two methods were compared, as were the values of 4 local velocity profiles. The two methods yielded U_τ values for the mean velocity profile that differed by 1.2%, and local U_τ values that differed by an average of 3.2% and no more than 5.5%. The velocity defect matching method was employed to assess the friction velocities for the individual velocity profiles measured in this study because it could be more easily and reliably implemented in an optimization code than the modified Clauser chart method. The U_τ value for the smooth wall was found using the modified Clauser method. The smooth wall LDV and PIV

data gave slightly different U_τ values (0.047 m s^{-1} for the LDV data and 0.049 m s^{-1} for the PIV data).

Results and Discussion

Mean Velocity Profile Analysis

Figure 3.2 shows the mean velocity profile over the biofilm normalized using inner units (left panel) and outer units in velocity defect form (right panel), with the smooth-wall profile from both PIV and LDV for comparison. The turbulent boundary layer over the biofilm appears to exhibit a standard mean velocity profile, with a log-law region and the expected downward shift (ΔU^+) found in rough-wall flows (Fig. 3.2A).

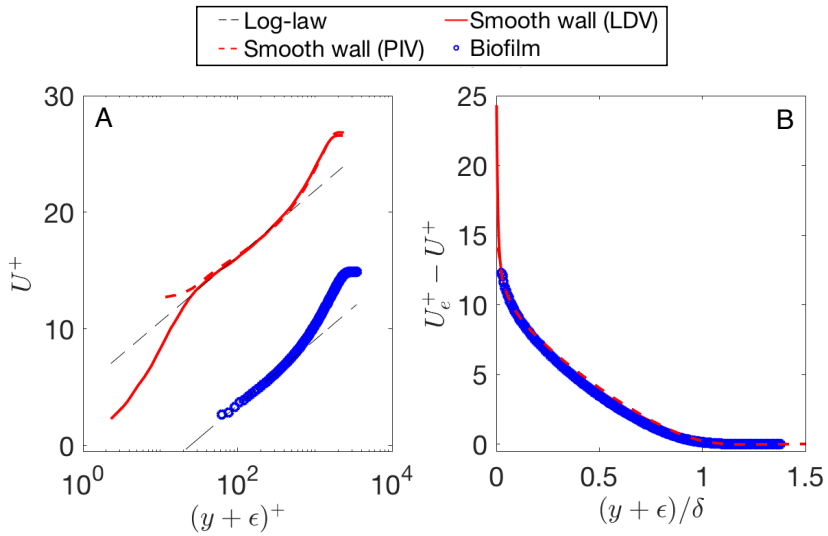

Figure 3.2. Average streamwise velocity profile over the biofilm and smooth wall in (A) inner units and (B) velocity defect form.

The downward shift in the log-law, also termed the roughness function, is ΔU^+=12.8. This corresponds to a roughness Reynolds number of k_s^+ = 736, an order of magnitude higher than the threshold value of k_s^+ = 80 given by Jimenez (2004) indicating that the flow is in the fully-rough regime (Table 3.1). This yields an equivalent sand-grain roughness height (k_s) of 8.8 mm, meaning that the biofilm destroys the viscous sublayer, and the roughness effect on the mean flow is large. The k_s value is significantly larger than the physical height of the biofilm (8.8 mm versus 1.7 mm), indicating that the flapping streamers and possibly the compliance of the biofilm layer may contribute to the large roughness effects of the biofilm. Additionally, the skin-friction coefficient ($C_\mathrm{f} = 2\frac{{U_\tau}^2}{{U_e}^2}$) is significantly increased over the biofilm as compared to the smooth wall (9.0×10^{-3} for the biofilm versus 2.9×10^{-3} for the smooth wall). However, when the biofilm mean velocity profile is presented in the defect form, a good collapse with the smooth-wall data is observed (Fig. 3.2B). This outer layer similarity forms the basis of scaling techniques that aim to model the effects of surface roughness on vessel performance (Schultz 2007).

Figure 3.3 presents the streamwise averaged Reynolds stress profiles (blue circles), normalized in inner units, with smooth wall profiles (red line) for comparison. Additionally, the local profiles (normalized by the local U_τ and ε values) at each streamwise location in the PIV frame are shown (gray lines) to highlight the heterogeneities that the biofilm bed introduces in the roughness sublayer. The streamwise Reynolds stress (Fig. 3.3A) over the biofilm shows significant changes compared with the smooth-wall condition in the roughness sub-layer region (y/δ < 0.5). The expected smooth-wall peak in $< u'u' >$ in the inner region is suppressed, possibly due to the high momentum deficit near the biofilm. Instead, a wider, weaker peak is seen at y/δ ~ 0.3. The peak/plateau region in the Reynolds shear stress (RSS $= -< u'v' >$) over the biofilm is shifted away from the bed, has a sharper shape, and is elevated compared to the

smooth wall (Fig. 3.3B). The upward shift of the peak in both $u'u'$ and $u'v'$ is similarly seen over non-uniform biofilm fouling (Walker et al., 2013b), and is due to the relative increase of friction forces due to drag on the roughness elements and resulting relative decrease in viscous forces. Finally, the streamwise averaged vertical Reynolds stress profile (Fig. 3.3C; blue circles) has a slightly elevated peak compared with the smooth wall profile, however some individual profiles peak at lower values. It is worth pointing out that the streamwise averaged Reynolds stress profiles (blue circles) are located at the higher end of the range of the local profiles (gray lines) because the U_τ calculated from the streamwise average velocity profile was slightly lower than the local U_τ values. All of the Reynolds stress profiles show good collapse in the outer layer.

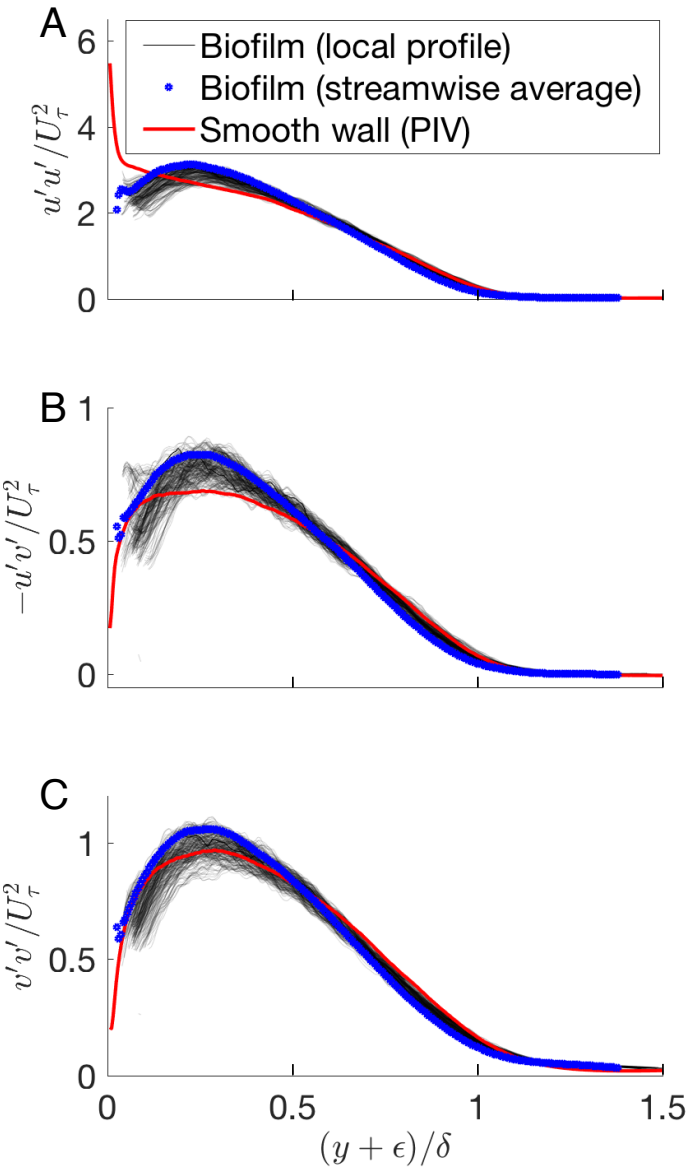

Figure 3.3. Average streamwise Reynolds stresses for the biofilm (blue circles) and smooth-wall (red lines) cases. The local values of the Reynolds stresses above the biofilm (gray lines) are also presented. (A) u'^{2+}; (B) $-u'v'^{+}$; (C) v'^{2+}

Spatially explicit mean flow analysis

Time-averaged streamwise (U) and vertical (V) velocity fields are presented in Fig. 3.4, shown with smooth wall data for comparison and normalized using outer units (δ and U_e). The streamwise velocity over the biofilm exhibits a layer of low-momentum flow in the form of a momentum deficit that is evident just at the biofilm roughness layer when compared with the smooth-wall streamwise velocity field. Even though the variability of biofilm topography in the streamwise direction is considerable (masked white region below the contour values on Fig. 3.4A), the mean streamwise velocity is quite homogeneous in the streamwise direction. In contrast, there is a striking increase in vertical velocity at the bed, as well as spatial heterogeneity in the vertical velocity over the biofilm.

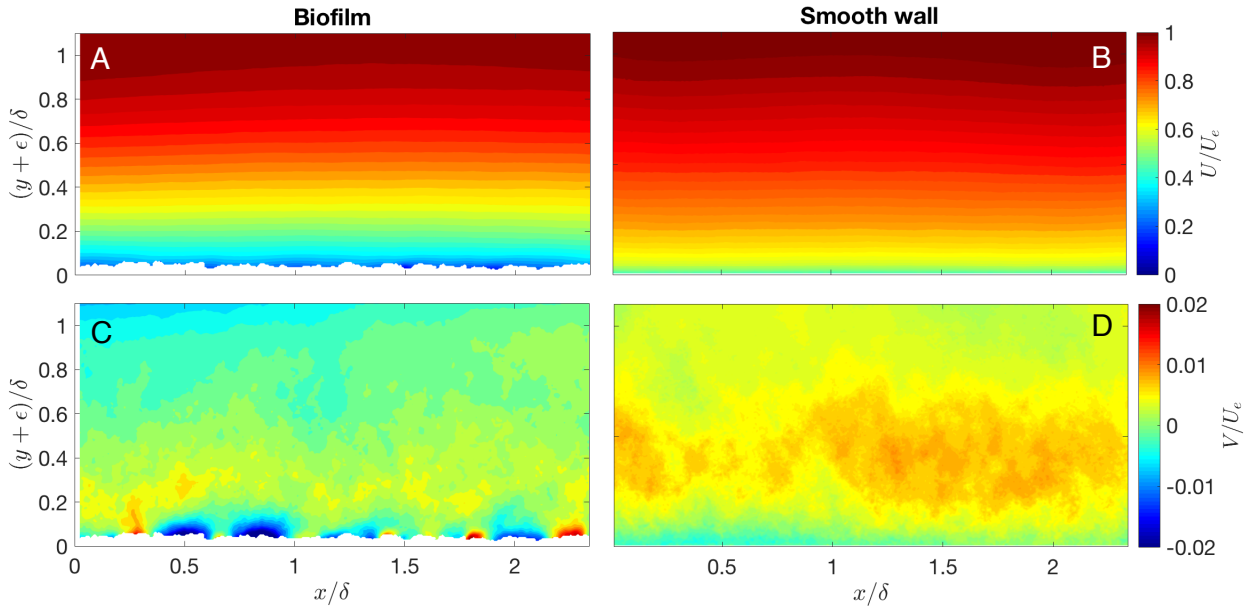

Figure 3.4. Time- averaged streamwise (A and B) and vertical (C and D) velocity over a biofilm (left panels) and smooth wall (right panels). Normalized with outer units: the freestream velocity, U_e and the boundary layer thickness, δ.

Figure 3.5 shows the time-averaged RSS and turbulent kinetic energy ($tke = \frac{1}{2}(u'^2 + v'^2)$), for both the biofouled and smooth wall, normalized by the freestream velocity. The RSS fields (Fig. 3.5 (A, B & C)) show an increase in shear stresses over the biofouled wall, as well as an upward shift in the location of the shear stress maximum. This is similar to what is seen in Fig. 3.3B. There is also enhancement of the 2D *tke* over the biofilm (Fig. 3.5 (D, E & F)). Like the RSS, *tke* also displays high streamwise spatial heterogeneity over the biofilm, and the core of *tke* ($y/\delta > 0.1$ to $y/\delta < 0.4$) is more than 3 times greater than that of the smooth-wall case. The near bed hotspots of *tke* likely indicate increased turbulent transport and vertical mass and momentum transport (Reidenbach et al. 2010), which is important for transport of solutes to and from the bed. This suggests that even over a fairly uniform biofilm, enhancement of access to nutrients due to turbulence is locally variable.

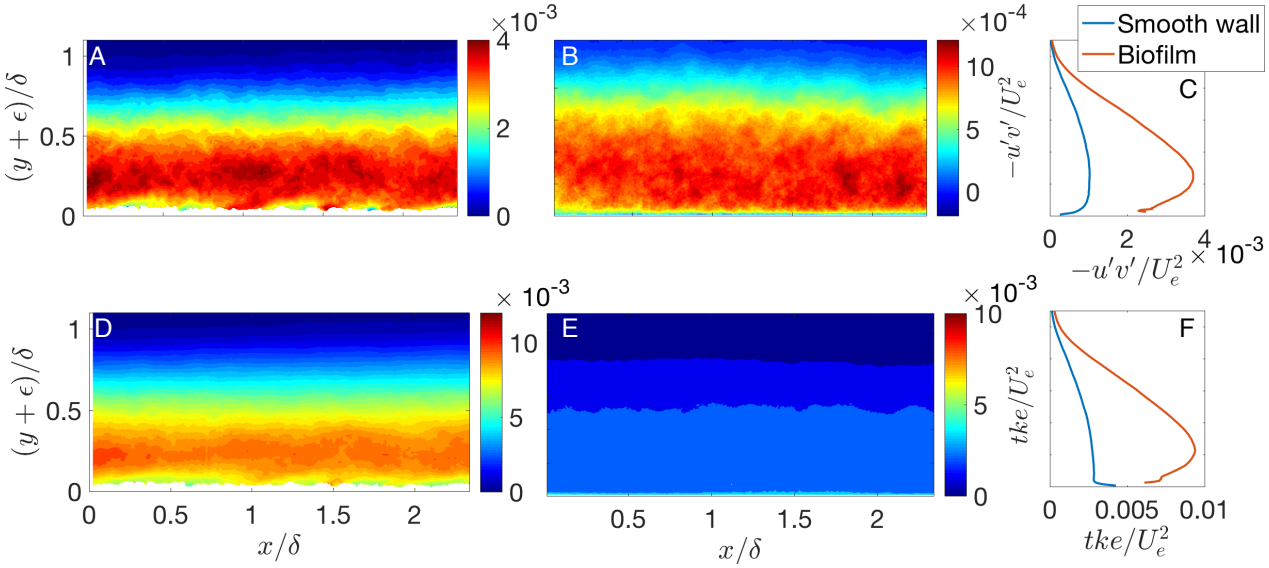

Figure 3.5. The 2D Reynolds shear stress (*RSS*) over the biofilm (A) and over the smooth wall (B) and the turbulent kinetic energy (*tke*) over the biofilm (C) and the smooth wall (D), all normalized by the free stream velocity (U_e^2). Note that the scale of the colorbars differ between the smooth wall and biofilm. To highlight the difference in magnitude of smooth wall and

biofilm *RSS* and *tke* at different heights above the bed, streamwise averages of these values are also plotted (E & F). Note that here the y- axis is the δ normalized height above the bed.

Because of the spatial heterogeneity of the biofilm layer, it is also useful to perform a spatial decomposition of the velocity field

$$\tilde{u} = U - \langle U \rangle_{\Lambda} \tag{3.4}$$

where $\langle U \rangle_{\Lambda}$ is the temporally and spatially (streamwise) averaged velocity field (Kevin et al. 2017). The dispersive stresses are then $\tilde{u}\tilde{v}$. Dispersive stress fields illustrate where spatial variability in the flow, due to the surface topography, results in momentum transport (Coceal et al. 2006). Analysis of the dispersive stress is common in investigations of atmospheric flow over vegetation or urban surfaces, because the dispersive stress contributes to transport of scalar quantities, especially within sparse canopies (Poggi et al. 2004). Over the biofilm, hotspots of spatial variability in the flow are confined to the near-bed region (Fig. 3.6A). These areas of elevated dispersive stresses seem to coincide with the downstream edges of the larger biofilm elements. The dispersive stresses are small compared to the RSS. In the near-bed region, the dispersive momentum flux, $\tilde{u}\tilde{v}$, reaches about 10% of the RSS. The production of *tke* ($P = -u'v'\frac{\partial U}{\partial y}$) is also spatially heterogeneous (Fig. 3.6B). There appears to be strong production of *tke* trailing behind many of the roughness elements of the biofilm. This is similarly seen in gravel beds, where enhanced *tke* production in the wake region behind protrusions results in strong turbulent interactions with the bed and increased vertical transport of mass and momentum (Reidenbach et al. 2010; Mignot et al. 2009).

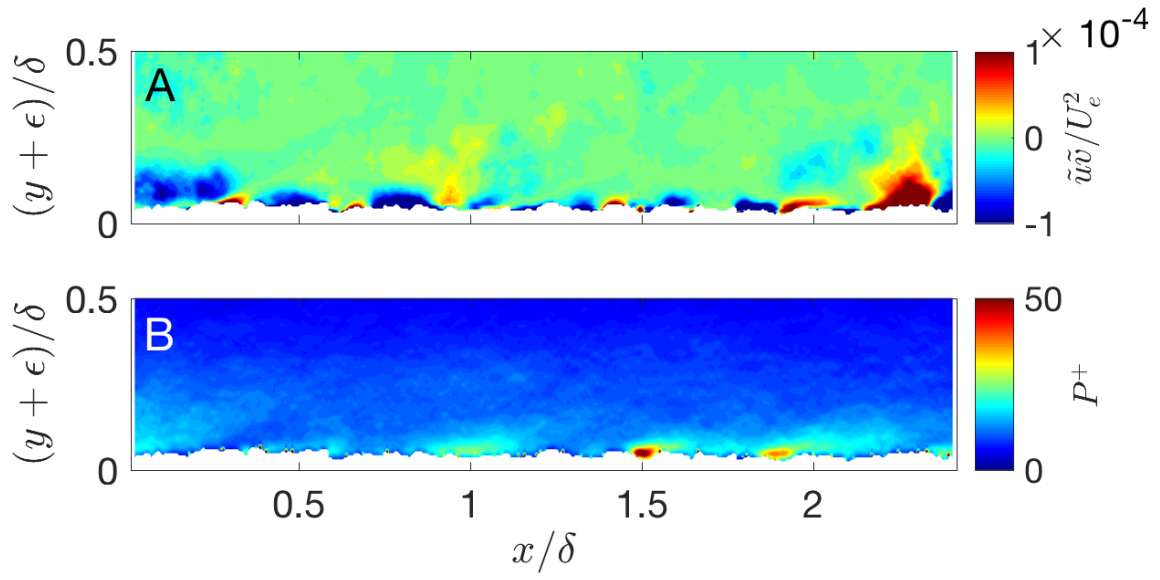

Figure 3.6. Dispersive stresses (A), normalized by U_e^2 and (B) production of *tke* (P), normalized by U_e^3/δ. Each vertical profile of U was smoothed using a smoothing spline before finding $\frac{\partial U}{\partial y}$ in P. Only the near-bed region is shown in order to highlight the spatial heterogeneity of the turbulence quantities.

Spatial Coherence Analysis

Different types of roughness can have similar effects on the mean velocity profile (eg mesh and rods) (Krogstad and Antonia 1999), but different effects on turbulence generation and turbulent stresses. For example, roughness alters the structure of the turbulence itself within the boundary layer, altering the size and coherence of vortices and the generation of turbulence at the wall (Volino et al. 2009; Volino et al. 2011, Wu and Christensen 2010, Mejia-Alvarez and Christensen 2011). However, little is known about how compliant roughness or flapping streamers alters this turbulence structure.

Coherent structures in the turbulent flow over the biofilm were assessed using three methods: two-point correlation, quadrant analysis, and the probability density function of the instantaneous RSS. The inhomogeneous two-point correlation in the streamwise-wall-normal plane is given as

$$\rho_{u_i u_j} = \frac{\overline{u_i(x_{ref},y_{ref})u_j(x_{ref}+\Delta x,y_{ref}+\Delta y)}}{\sigma_{u_i}(x_{ref},y_{ref})\sigma_{u_j}(x_{ref}+\Delta x,y_{ref}+\Delta y)} \quad (3.5)$$

where $\rho_{u_i u_j}$ is the two-point correlation normalized by the standard deviation of the local velocity and the reference velocity, and x_{ref} and y_{ref} denote the reference location. Here we used y_{ref} = 0.15δ and x_{ref} was taken as the middle of the velocity field frame (Fig. 3.7). For the streamwise correlation, the angle of inclination of ρ_{uu} (black line in Figs. 3.7A & 3.7B) is an indication of the angle of the coherent structures that are shed from the wall (Christensen and Adrian 2001; Volino et al. 2007). The angle of inclination of ρ_{uu} is 12.6° for the smooth wall and 16.5° for the biofilm wall and was calculated by finding the point on each contour line that is furthest from the reference point and fitting a line through them. The slight increase in inclination angle over the biofilm may be due to increased vertical momentum transport over the biofilm bed. The streamwise- and wall-normal coherence of ρ_{uu} shows only a small qualitative difference between the smooth-wall and the biofilm flows. In both cases, ρ_{uu} is elongated in the streamwise direction. However, over the biofilm wall, ρ_{uu} appears to be slightly more elongated compared to the smooth wall, which is in contrast with several other rough-wall flows, where a reduction of the streamwise coherence of ρ_{uu} is seen (Wu and Christensen 2010; Volino et al. 2007). The shape of the wall-normal correlation, ρ_{vv}, is thought to be indicative of the size of the

heads of hairpin packets (Wu and Christensen 2010). As has been shown in studies over other types of roughness, the shape of ρ_{vv} does not appear to be affected by the biofilm (Wu and Christensen 2010). The cross correlation ρ_{uv} also appears similar over the smooth wall and the biofilm.

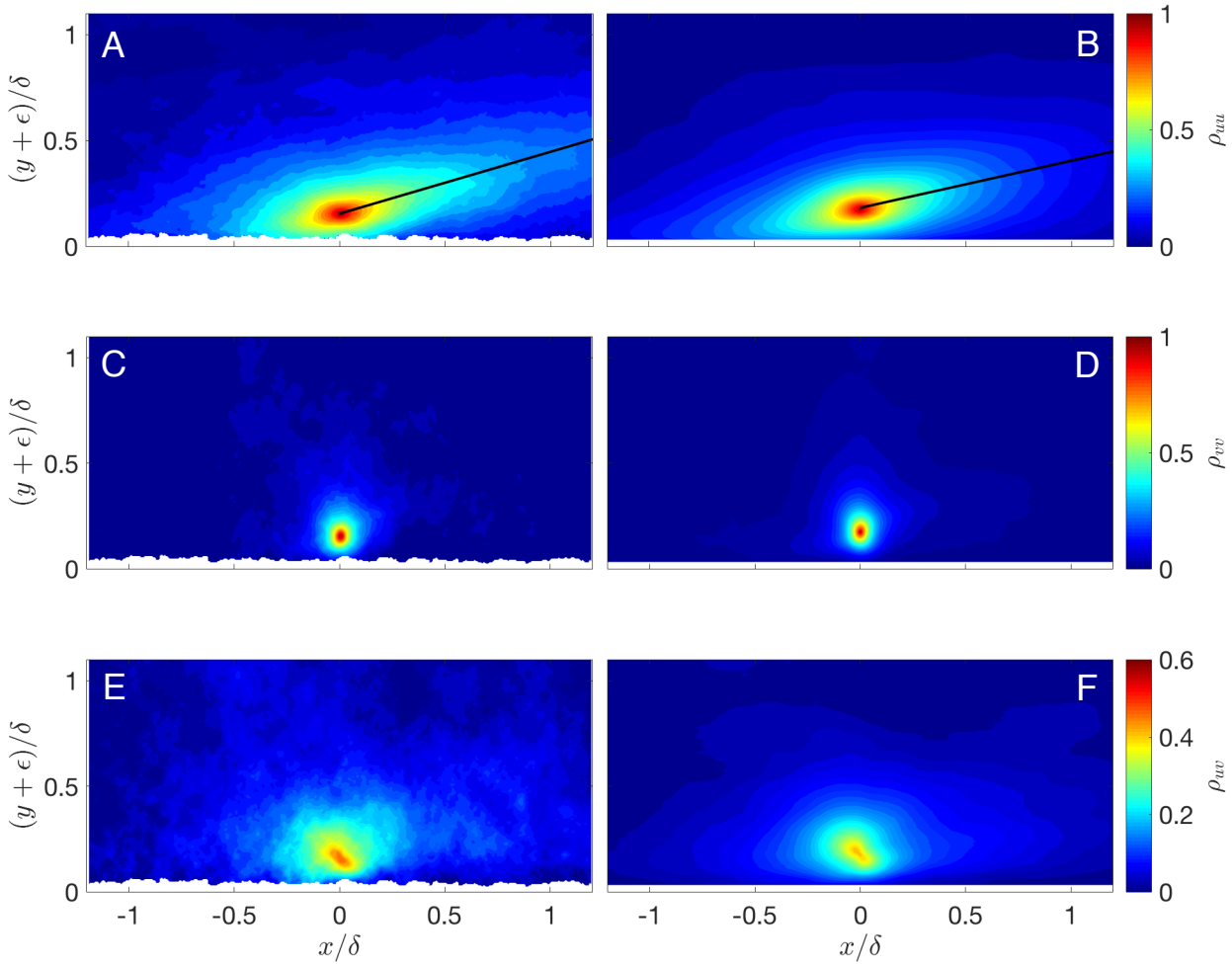

Figure 3.7. The two-point correlations, ρ_{vv} (A & B), ρ_{uu} (C & D) and ρ_{uv} (E & F), shown with data from a smooth wall for comparison. The black line in C and D marks the angle of inclination.

The inclination angle of ρ_{uu} suggests that vortical structures in the flow move coherently away from the biofilm surface at a steeper angle than away from the smooth surface. However,

qualitatively the two-point correlation maps look quite similar. Coherent vortical structures are important in the transport of turbulence in the boundary layer, especially the ejection of low-momentum fluid from near the bed into the outer layer (Moin and Kim 1985). Similarity in shape and angle of the streamwise correlation over the rough biofilm surface and the smooth wall has been seen over other types of 3D roughness, both irregular (Wu and Christensen 2010) and regular (Volino et al. 2007), though these studies also find a small decrease in the streamwise length of the correlation ellipses. Similarity in the shape of ρ_{uv} over a rough and smooth surface was also observed in Volino et al. 2007. This and other studies, however, have shown a reduction in the streamwise length of contours of ρ_{vv} and ρ_{uv} with otherwise similar shapes (Wu and Christensen 2010), which is thought to be due to a decrease in the length scales of large- scale groupings of vortices over rough surfaces. The present results suggest that the biofilm surface increases the coherence of the turbulence slightly, whereas rigid roughness tends to decrease it.

The angle and spatial extent of these correlations appears to show that the mechanisms of energy and momentum transport in the biofilm flow are similar but not identical in structure to that over the smooth wall or over rigid roughness. This may have to do with the way eddies are shed off of the cell clusters, causing three-dimensional flapping of the streamers (Stoodley et al. 1998). Energy and momentum transport in turbulent wall bounded flow is hypothesized to be largely due to the presence of packets of hairpin vortices that entrain fluid and drive turbulent ejections and sweeps (Wu and Christensen 2010).

Quadrant analysis

Quadrant analysis is used to measure the relative contribution of instantaneous turbulent sweeps (Q_4; where $u' > 0, v' < 0$) and ejections (Q_2; where $u' < 0, v' > 0$) to the overall RSS

field. The Quadrant-Hole technique was used to identify only the contribution of high-magnitude instantaneous events (Lu & Willmarth, 1973). The time-averaged Q2 and Q4 fields are presented in Fig. 8 and were calculated by taking the conditional average of local instantaneous events where

$$|u'v'| > H\sigma_u\sigma_v \qquad (3.6)$$

with, here, $\sigma_{u_i} = \sqrt{\langle u_i'^2 \rangle}$ and a hyperbolic hole of size $H = 4$. Only the results for Q_2 and Q_4 are given, as the contributions of Q_1 and Q_3 events (where $u'v' > 0$) are negligible. The Quadrant-Hole results indicate that strong turbulent sweeps are the primary contributors to the RSS near the biofilm surface (Fig. 3.8B), while turbulent ejections become more dominant further from the bed (Fig. 3.8A). This means that there is significant downrushing of high momentum fluid from further up in the boundary layer toward the bed. This Q4 dominance at the bed may in large part be due to prograde vortices (i.e. vortices rotating with the mean shear) being shed off of the biofilm clusters and streamers. This is observed above canopy flows, where prograde vortices shed off of flexible seagrass analogs have strong downward momentum and weaker upward momentum at the top of the canopy (Ghisalberti and Nepf 2006; Raupach et al. 1991; Hansen and Reidenbach 2017). There is also significant streamwise spatial heterogeneity in the strength of sweeps and ejections, because these turbulent events are a result of the bed topography.

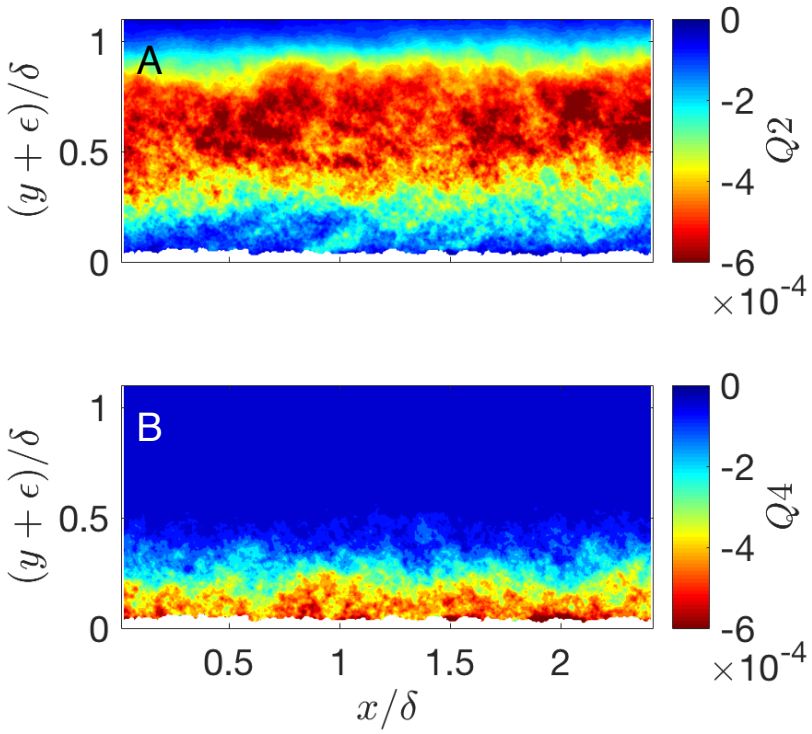

Figure 3.8. The time- averaged contributions of turbulent ejections (Q_2; A) and sweeps (Q_4; B) with $H = 4$.

The probability density function (PDF) of instantaneous RSS is another useful way to quantify the dominant structures of turbulent flow over the biofilm (Fig. 3.9), here presented at four different y/δ positions above the biofilm, along with the RSS PDFs over the smooth wall. It appears that the RSS contributions are similar between the smooth wall and biofilm, and are similar at the different heights over the wall. Over rigid roughness, large 2-D roughness elements tend to have the most divergence in the RSS PDF from the smooth wall, while large and small 3-D roughness elements are far more similar (Volino et al. 2011). Because the biofilm is highly three dimensional, the results shown in Fig. 3.9 fit with previously observed behavior.

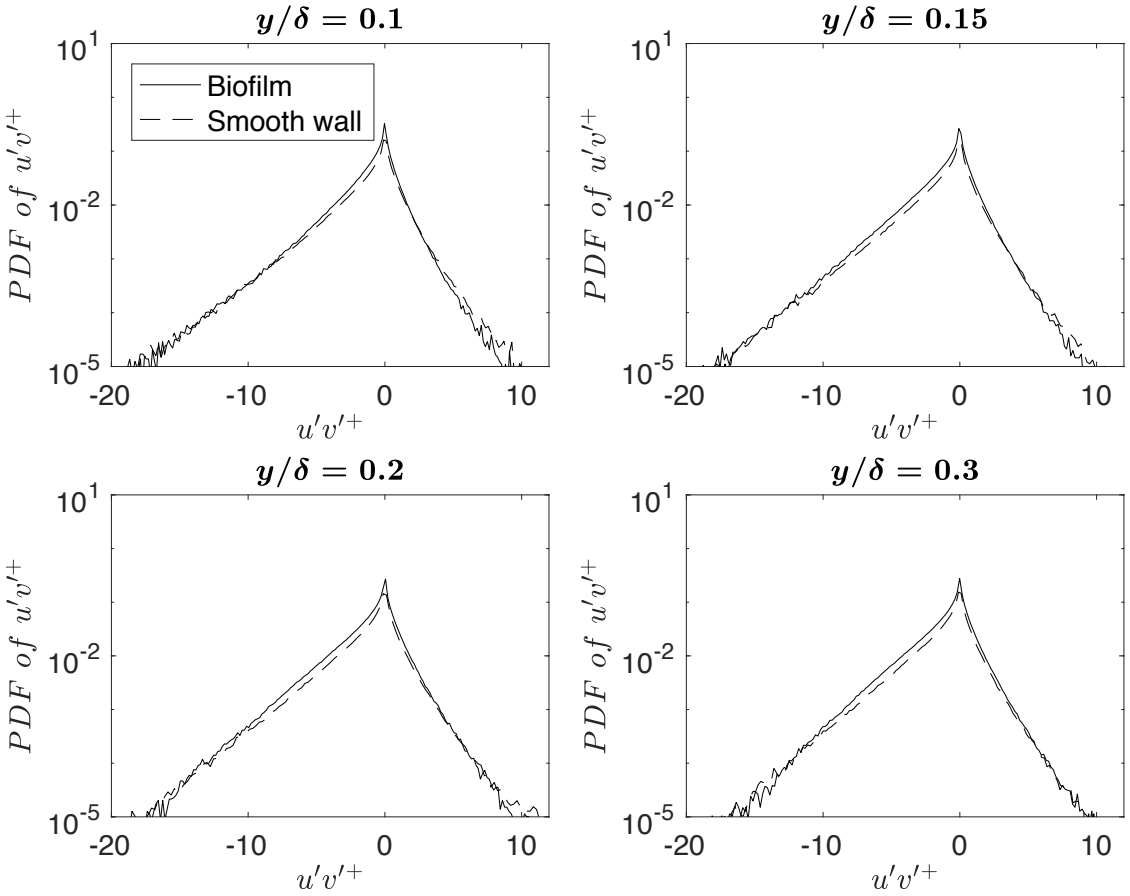

Figure 3.9. The probability density function of the instantaneous RSS over the biofilm (solid line) and smooth wall (dashed line; from PIV data) at four different heights above the bed.

Conclusion

The aim of this study was to address the mechanisms resulting in high drag due to low form, compliant biofilms. To accomplish this, the study addresses the spatially resolved turbulence structure over a biofilm at moderate Reynolds number. The results show that biofilms extract energy from the flow through the roughness of the biofilm surface as well as the flapping streamers, resulting in a larger effective roughness height than the physical roughness.

Additionally, there is large spatial heterogeneity in the turbulence and momentum transport over the bed even though the biofilm was relatively uniform in coverage.

Generally, the mean statistics of the biofilm-fouled surface behaved similarly to a rigid rough wall. Turbulent kinetic energy production appeared dominant at discrete locations along the bed (Fig. 3.5D). Near bed local variability in turbulence production (Fig. 3.6B) and momentum fluxes (Fig. 3.8) indicate that while outer layer similarity is maintained over a biofilm, small scale turbulence structures near the bed, which are important for transport of nutrients to sessile biofilms as well as the hydrodynamic forces that slough biofilm off the surface, are altered by local bed topography created by the biofilm. This dynamic is also observed over coral reefs, where the roughness effects of the reef as a whole determine integrated flow characteristics such as drag coefficient and shear, but at the organismal scale local topography impacts biologically relevant hydrodynamics (Reidenbach et al. 2006). Biofilm growth is highly dependent on fluid motion, even more so than light environment or nutrient concentration (Hondzo and Wang 2002), and it may be that biofilms engineer their near-bed hydrodynamic regime by increasing turbulence in the inner region of the boundary layer, leading to increased vertical transport of nutrients to the biofilm, and transport of metabolic byproducts from the biofilm. This increase in vertical transport is likely beneficial to the biofilm community, however, the increase in shear stresses may also lead to sloughing off of the biofilm. In fact, most ship hulls exhibit sparse or patchy slime fouling. This variability in the physical structure of the biofilm was not addressed in the present work, in order to gain a baseline understanding of flow over a biofilm, but future studies should address the hydrodynamic impacts of patchy biofilms. This added surface roughness due to the biofilm, despite the low vertical relief, results in increased drag due to high levels of momentum transport likely due to flapping streamers and

surface compliance. Integrated over a large surface such as a ship hull, this can result in significant drag penalties.

References

Castro IP. 2007. Rough-wall boundary layers: mean flow universality. J Fluid Mech. 585:469-485.

Christensen KT, Adrian RJ. 2001. Statistical evidence of hairpin packets in wall turbulence. J Fluid Mech. 431:433-443.

Coceal O, Thomas TG, Castro IP, Belcher SE. 2006. Mean flow and turbulence statistics over groups of urban-like cubical obstacles. Bound-Layer Meteor. 121(3):491-519.

Coles D. 1956. The law of the wake in the turbulent boundary layer. J Fluid Mech. 1:191-226.

de Beer D, Kühl M. 2001. Interfacial microbial mats and biofilms. In: Boudreau BP, Jørgensen BB, editors. The Benthic Boundary Layer. Oxford University Press, Inc.

de Beer D, Stoodley P, Lewandowski Z. 1996. Liquid flow and mass transport in heterogeneous biofilms. Water Res. 30:2761-2765.

Decho AW. 1990. Microbial exopolymer secretions in ocean environments: Their role(s) in food webs and marine processes. Oceanogr Mar Biol Annu Rev. 28:73-153.

Flack KA, Schultz MP. 2010. Review of hydraulic roughness scales in the fully rough regime. J Fuids Eng. 132:041203.

Flack KA, Schultz MP, Shapiro TA. 2005. Experimental support for Townsend's Reynolds number similarity hypothesis on rough walls. Phys Fluids. 17:035102.

Flack KA, Schultz MP, Connelly JS. 2007. Examination of a critical roughness height for outer layer similarity. Phys Fluids. 19:095104.

Ghisalberti M, Nepf H. 2006. The structure of the shear layer in flows over rigid and flexible canopies. Env Fl Mech. 6:277-301.

Graba M, Moulin FY, Boulêtreau S, Garabétian F, Kettab A, Eiff O, Sánchez-Pérez JM, Sauvage S. 2010. Effect of near-bed turbulence on chronic detachment of epilithic biofilm: Experimental and modeling approaches. Water Resour Res. 46:W11531.

Hansen JCR, Reidenbach MA. 2017. Turbulent mixing and fluid transport within Florida Bay seagrass meadows. Adv Water Resour. 108:205-215.

Haslbeck EG, Bohlander G. 1992. Microbial biofilm effects on drag- lab and field. In: Proceedings of the SNAME Ship Production Symposium. Paper No. 3A-1. Jersey City, NJ: SNAME; 7p.

Hondzo M, Wang H. 2002. Effects of turbulence on growth and metabolism of periphyton in a laboratory flume. Water Resour Res. 38:1277.

Jiménez J. 2004. Turbulent flows over rough walls. Annu Rev Fluid Mech. 36:173-196.

Kevin K, Monty JP, Bai HL, Pathikonda G, Nugroho B, Barros JM, Christensen KT, Hutchins N. 2017. Cross-stream stereoscopic particle image velocimetry of a modified turbulent boundary layer over directional surface pattern. J Fluid Mech. 813:412-435.

Krogstad PÅ, Antonia RA. 1999 Surface roughness effects in turbulent boundary layers. Exp Fluids. 27:450-460.

Lu SS, Willmarth WW. 1973. Measurements of the structure of the Reynolds stress in a turbulent boundary layer. J Fluid Mech. 60(3):481-511.

Mejia-Alvarez R, Christensen KT. 2010. Low-order representations of irregular surface roughness and their impact on a turbulent boundary layer. Phys Fluids. 22:015106.

Mignot E, Hurther D, Barthelemy E. 2009. On the structure of shear stress and turbulent kinetic energy flux across the roughness layer of a gravel-bed channel flow. J Fluid Mech. 638:423-452.

Moin P, Kim J. 1985. The structure of the vorticity field in turbulent channel flow. Part 1: Analysis of instantaneous fields and statistical correlations. J Fluid Mech. 155:441-464.

Molino PJ, Wetherbee R. 2008. The biology of biofouling diatoms and their role in the development of microbial slimes. Biofouling. 24:365-379.

Murphy EAK, Barros JM, Schultz MP, Flack KA, Steppe CN, Reidenbach MA. 2017. The turbulent boundary layer structure over diatomaceous slime fouling. In: Proceedings of the 10th International Symposium on Turbulence and Shear Flow Phenomena, Chicago, USA.

Nikora VI, Goring DG, Biggs BJ. 2002. Some observations of the effects of micro-organisms growing on the bed of an open channel on the turbulence properties. J Fluid Mech. 450:317-341.

Nikuradse J. 1933. Laws of flow in rough pipes. NACA Technical Memorandum 1292.

Perry AE, Li JD. 1990. Experimental support for the attached-eddy hypothesis in zero-pressure-gradient turbulent boundary layers. J Fluid Mech. 218:405-438.

Poggi D, Katul GG, Albertson JD. 2004. A note on the contribution of dispersive fluxes to momentum transfer within canopies. Bound-Layer Meteor. 111(3):615-621.

Raupach MR, Antonia RA, Rajagopalan S. 1991. Rough-wall turbulent boundary layers. Appl Mech Rev. 44(1):1-25.

Reidenbach MA, Limm M, Hondzo M, Stacey MT. 2010. Effects of bed roughness on boundary layer mixing and mass flux across the sediment-water interface. Water Resour Res. 46:W07530.

Reidenbach MA, Monismith SG, Koseff JR, Yahel G, Genin A. 2006. Boundary layer turbulence and flow structure over a fringing coral reef. Limnol Oceanogr. 51:1956-1968.

Schultz MP. 2007. Effects of coating roughness and biofouling on ship resistance and powering. Biofouling. 23:331-341.

Schultz MP, Flack KA. 2007. The rough- wall turbulent boundary layer from the hydraulically smooth to the fully rough regime. J Fluid Mech. 580:381-405.

Schultz MP, Bendick JA, Holm ER, Hertel WM. 2011. Economic impact of biofouling on a Naval surface ship. Biofouling. 27:87-98.

Schultz MP, Walker JM, Steppe CN, Flack KA. 2015. Impact of diatomaceous biofilms on the frictional drag of fouling-release coatings. Biofouling. 31:759-773.

Stocking JB, Rippe JP, Reidenbach MA. 2016. Structure and dynamics of turbulent boundary layer flow over healthy and algae-covered corals. Coral Reefs. 35:1047-1059.

Stoodley P, Lewandowski Z, Boyle JD, Lappin-Scott HM, 1998. Oscillation characteristics of biofilm streamers in turbulent flowing water as related to drag and pressure drop. Biotechnol Bioeng. 57:536-544.

Stoodley P, Lewandowski Z, Boyle JD, Lappin-Scott HM. 1999. Structural deformation of bacterial biofilms caused by short-term fluctuations in fluid shear: An *in situ* investigation of biofilm rheology. Biotechnol Bioeng. 65:83-92.

Taherzedah D, Picioreanu C, Küttler U, Simone A, Wall WA, Horn H. 2009. Computational study of the drag and oscillatory movement of biofilm streamers in fast flows. Biotechnol Bioeng. 105(3):600-610.

Townsin RL. 2003. The ship hull fouling penalty. Biofouling. 19:9-15.

U.S. Navy. 2006. Naval Ships' Technical Manual Chapter 081 Waterborne Underwater Hull Cleaning of Navy Ships. Oct 1, Revision 5. Direction of Commander, Naval Sea Systems Command. S9086-CQ-STM-010.

Volino RJ, Schultz MP, Flack KA. 2007. Turbulence structure in rough- and smooth-wall boundary layers. J Fluid Mech. 592:263–293.

Volino RJ, Schultz MP, Flack KA. 2009. Turbulence structure in a boundary layer with two-dimensional roughness. J Fluid Mech. 635:75–101.

Volino RJ, Schultz MP, Flack KA. 2011 Turbulence structure in boundary layers over periodic two- and three-dimensional roughness. J Fluid Mech. 676:172-190.

Walker JM, Flack KA, Lust EE, Schultz MP, Luznik L. 2013a. Experimental and numerical studies of blade roughness and fouling on marine current turbine performance. Renew Energ. 66:257-267.

Walker JM, Sargison JE, Henderson AD. 2013b. Turbulent boundary-layer structure of flows over freshwater biofilms. Exp Fluids. 54:1628.

Wu Y, Christensen KT. 2010. Spatial structure of a turbulent boundary layer with irregular surface roughness. J Fluid Mech. 655:380-418.

Xu S, Rempfer D, Lumley J. 2003. Turbulence over a compliant surface: Numerical simulation and analysis. J Fluid Mech. 478:11-34.

Zargiel KA, Coogan JS, Swain GW. 2011. Diatom community structure on commercially available ship hull coatings. Biofouling. 27:955-965.

Chapter 4

Impacts of biofilm patchiness on boundary layer hydrodynamics

Elizabeth A. K. Murphy[1], Julio M. Barros[2+], Michael P. Schultz[3], Karen A. Flack[2], Cecily N. Steppe[4], Matthew A. Reidenbach[1]

[1]Department of Environmental Sciences, University of Virginia, 291 McCormick Rd, Charlottesville, Virginia, 22903, USA, 925-330-2992, eam6vf@virginia.ed

[+] Current affiliation Fluid Mechanics Unit, Okinawa Institute of Science and Technology, 1919-1 Tancha, Onna-son, Kunigami-gun, Okinawa, Japan 904-0495, juliomanuel.barrosjunior@oist.jp

[2]Department of Mechanical Engineering, United States Naval Academy, 590 Holloway Road, Annapolis, Maryland, 21402, USA, 410-293-6440, 410-293-6500, julio.barros.br@usna.edu

[3]Department of Naval Architecture and Ocean Engineering, United States Naval Academy, 590 Holloway Road, Annapolis, Maryland, 21402, USA, 410-293-6440, mschultz@usna.edu

[2]Department of Mechanical Engineering, United States Naval Academy, 590 Holloway Road, Annapolis, Maryland, 21402, USA, 410-293-6501, flack@usna.edu

[4]Department of Oceanography, United States Naval Academy, 572C Holloway Rd, Annapolis, Maryland, 21402, USA, 410-293-6552, natunewi@usna.edu

[1]Department of Environmental Sciences, University of Virginia, 291 McCormick Rd, Charlottesville, Virginia, 22903, USA, 434-243-4937, reidenbach@virginia.edu

Abstract

Algal biofilms are ubiquitous in aquatic systems, including as fouling on ship hulls. Biofilm fouling exerts a steep drag penalty on ships, reducing performance and increasing fuel consumption. This study used high resolution particle image velocimetry (PIV) to examine spatially explicit turbulence in the boundary layer over patchy diatomaceous biofilms at low but ship- relevant Reynolds numbers. The mean velocity profiles over biofilms have a large downward shift due to momentum extracted from the flow, and higher friction velocity and drag coefficient compared to a control plate with no biofilm. Non-uniform biofilms have the greatest

increase in near- bed turbulence production (streamwise average P^+ of 31.4 versus 23.7 for a patchy biofilm vs. the uniform biofilm, respectively), dispersive stresses (with values of $|\tilde{u}\tilde{v}|/U_e^2$ up to three times as high over a non-uniform compared to a uniform biofilm), and rotational flow, compared with a uniform or sparse biofilm. Additionally, more patchy biofilms appear to create a plane mixing layer, which was not seen over the uniform biofilm. Uniform biofilm, however, increases the drag coefficient of the bed more than patchy biofilms (C_f of 9.0e-3 over the uniform biofilm and between 7.4e-3 and 2.9e-3 for non-uniform biofilms). We find that percent cover of a biofilm could be a better indicator of the effect of a biofilm on ship performance than biofilm roughness.

Background

Algal biofilms, which are thin, compliant layers of algal and bacterial cells and excreted EPS (extracellular polymeric substance), are ubiquitous on aquatic surfaces. Biofilms are the most common fouling community on Naval vessels (Schultz et al. 2015), and substantially increase powering costs by increasing the frictional resistance of the ship surface (Schultz et al. 2011). This increased skin friction due to biofilm fouling impacts other engineered systems, such as by decreasing the capacity of hydroelectric canals (Andrewartha et al. 2010). In habitats such as streams and intertidal mudflats, biofilms are considered ecosystem engineers because they alter nutrient cycling and sediment stability (Decho 2000; Battin et al. 2003). On corals, algal biofilm growth can be detrimental to the reef community, damping flow velocity at the coral surface, inhibiting nutrient exchange, and effectively smothering the coral (Stocking et al. 2016).

Biofilms appear to alter boundary layer hydrodynamics in ways that are similar to rigid roughness (Murphy et al. *submitted*.; Walker et al. 2013). Momentum extracted from the flow predictably shifts the mean velocity profile throughout the boundary layer, and increases in turbulent kinetic energy and Reynolds shear stresses are apparent. However, in many instances, a larger increase in the momentum deficit than would be expected from rigid roughness is seen over biofilm. This is likely due to the compliance of the biofilm as well as flexible protrusions (called streamers) that form on the biofilm surface (Walker et al. 2013; Murphy et al. *submitted*). Additionally, biofilm can increase the strength of turbulent sweeps and ejections, similarly to what is seen over other types of vegetation (Hansen and Reidenbach 2012) and flows over rigid structures such as woven mesh (Krogstad et al. 1992). Even over relatively uniform biofilm, turbulence data have shown a high degree of spatial heterogeneity, with hotspots of turbulent kinetic energy (*tke)* production and dispersive stresses at the bed (Murphy et al. *submitted*). While previous research offers a baseline understanding of spatially integrated flow dynamics over biofilms, or only examines uniform biofilms, real-world biofilm fouling is often patchy, due to being sloughed off under shear (Schultz et al. 2003; Schultz 2000) or uneven growth during biofilm development, and spatially explicit data is needed to understand the mechanisms behind biofilm effects on surface bounded flows. Here we compare spatially explicit turbulence structure over patchy biofilm with previous measurements over a uniform biofilm, to address how patchiness alters the roughness effects of biofilm fouling. This study presents detailed flow field analysis of the turbulent boundary layer over patchy biofilms at moderate Reynolds number. Analysis of the turbulence structure and the mean velocity profile was guided by the following questions:

1. How does the drag coefficient on a biofilm fouled surface depend on biofilm morphology?
2. What is the local variability of bed shear stress and turbulence over nonuniform biofilms?
3. Does patchiness alter how biofilms impact coherent turbulent motions in wall bounded flow?

This study provides a unique dataset of detailed flow measurements over algal biofilms in turbulent flow, and addresses the hydromechanics behind the large drag penalty of biofilms using spatially explicit turbulence and momentum transport data, which is relevant to the impacts of biofilms on both ship performance and ecological processes.

Methods

Biofilms

The biofilms tested were grown from a culture of four genera of diatoms (*Amphora*, *Achnanthes*, *Entomoneis* and *Navicula*) collected from fouled plates exposed in the Indian River Lagoon, FL. These diatoms commonly make up slime fouling on ship hulls and other surfaces (Schultz et al. 2015; Zargiel et al. 2011). Brackish (18 ppt) diatom cultures were maintained in a dynamic slime exposure facility at the United States Naval Academy (Annapolis, MD, USA). The dynamic slime exposure facility, described in detail in Schultz et al (2015) is a 450 gallon tank with large (0.20 m x 1.52 m) acrylic plates affixed to a rotating drum (60 *rpm*; peripheral velocity 1.9 m s^{-1}), allowing the biofilm fouling on the plates to occur under shear stress. Biofilms were grown

under grow lights on an 18- hour light 8- hour dark cycle and were fed once weekly with a modified Guillard's f/2 fertilizer with silicate (Florida Aqua Farms, FL), a standard fertilizer used in aquaculture. Fouled plates used in this study were exposed to the biofilm culture for approximately 10 weeks. All plates had thick (approximately 1.7 mm), uniform biofilm fouling (Fig. 1A) after the 10-week exposure. Patchy (Fig. 1B) and sparse (Fig. 1C) biofilm fouling was achieved by spraying the surfaces with a hose and allowing the biofilm to naturally slough off. Four biofilm surfaces were tested, because the two patchy biofilms were one plate, imaged in at the same streamwise location but different spanwise locations, to quantify the semi- local variability of the biofilm. The percent cover and biofilm thickness were determined by measuring the thickness of wet, but air-exposed, biofilm using a wet film thickness paint gage (Schultz et al. 2015) at 33 locations in a grid on each biofilm surface. Presence/ absence of biofilm was used to estimate the percent cover. The peak-to-trough distances were measured in the frame used for PIV measurements, therefore, this is a local measurement of the biofilm roughness. This also means that biofilm roughness was measured under flow conditions, giving a better estimate of the roughness acting on the flow. Biofilm characteristics are presented in Table 1.

Particle Image Velocimetry

High resolution particle image velocimtety (PIV) was used to make detailed measurements of the flow in the streamwise - wall-normal $(\boldsymbol{x-y})$ plane over biofilm fouled acrylic plates in a recirculating turbulent tunnel facility. All measurements were taken ~1.22 m downstream of the boundary layer trip (1.1 m from the upstream edge of the fouled plate). 2-D PIV is a standard flow measurement technique wherein flow is seeded with small, reflective, neutrally buoyant

particles (here, 2 μm silver coated glass-spheres) and illuminated by a thin plane of laser light. Particles were illuminated in successive image pairs, taken 250 μs apart, and a recursive cross-correlation technique was used to find the velocity vectors based on statistically likely particle movement between the two frames in successively smaller interrogation windows. The final pass was 32^2 pixels with 50% overlap, satisfying the Nyquist sampling criterion. We used a commercial 2-D PIV system consisting of a 29 megapixel CCD camera (TSI) coupled to a double pulse laser (Quantel). Both the hydromechanics facility and the PIV system and post-processing (performed using Insight 4G version 11) are described in detail in Volino et al. 2007 and Murphy et al., *submitted*. The field of view and grid resolution of the velocity fields are given in Table 1. Each time- averaged velocity field was composed of 4000 statistically independent velocity fields. Smooth wall data from Murphy et al. *Submitted* are also presented for comparison. These data were taken over a non-fouled acrylic plate in the same facility as the biofilm data, using the same PIV system described above. Additionally, smooth wall flow and turbulence data was measured using laser Doppler velocimetry (LDV), at the same location on the plate as the PIV data and in the same facility. The LDV setup is described in Schultz and Flack (2007).

Results & Discussion

Velocity and turbulence structure

While flow over a fairly uniform biofilm exhibits classic log-law behavior (Murphy et al. 2017), the patchy biofilms appear to create a mixing layer effect downstream of prominent clumps of

biofilm, where the velocity profile is S-shaped. This is indicative of a plane mixing layer, a common feature of canopy flows and rough beds with large protuberances (Mignot et al. 2008). Figure 2 presents selected streamwise velocity profiles over the biofilms, chosen to highlight the flow shape over different topography types (peaks, troughs, and plateaus). The Reynolds shear stress is also plotted, because plane mixing layers typically also feature a peak in RSS. The near-bed region of the velocity profiles that are labeled in Figure 2 are plotted in Figure 3 to highlight the shape of the inversion of the streamwise velocity. In order to be a plane mixing layer, where intense turbulent mixing occurs, the inversion point is in the outer layer of flow, rather than the viscous or roughness sublayer. The streamwise velocity and RSS behavior over the patchy biofilms is similar to what is seen behind large protuberances in a gravel bed (Mignot et al. 2009; Reidenbach et al. 2010), and in canopy flows (Raupach et al. 1996). This has implications for the turbulence budget over patchy biofilms, because these S-shaped velocity profiles indicate areas where there are large, localized contributions to *tke* fluxes, production, and dissipation (Mignot et al. 2008), likely meaning that biofilm patchiness has an outsized effect on boundary layer turbulence. Based on the penetration depth of vortices under the crest of the biofilm roughness, measured as the depth where the turbulent stresses decline to 10% of their maximum value in the water column (Nepf and Vivoni 2000), measurement of the local penetration depth over each biofilm reveals that, in locations where the bed is exposed, momentum exchange occurs all the way to the bed. Where the biofilm covers the bed, we are unable to measure the water velocity within the biofilm layer, however it behaves like a porous media, with a flow velocity in channels within the biofilm that is directly related to the bulk flow velocity (De Beer and Kühl 2000).

Roughness Effects

In the few studies that have addressed the effects of biofilms on, e.g. ship performance or hydroelectric canal efficiency, biofilms are considered as added roughness to the surface (Schultz et al. 2015; Walker et al. 2013; Schultz and Swain 1999; Schultz 2000; Andrewartha et al. 2010). This is because, from an engineered systems perspective, the most important consequence of the biofilm fouling is its effect on the surface drag of an object. In the log-law region of the boundary layer over a rough surface, the velocity profile in inner units (where the terms are normalized by the friction velocity, U_τ, or the ratio of the kinematic viscosity to the friction velocity, $\frac{\nu}{U_\tau}$) is described in the log- law form by

$$U^+ = \frac{1}{\kappa}\ln(y+\varepsilon)^+ + C - \Delta U^+ \quad (1)$$

where ε is the wall datum offset and ΔU^+ is the roughness function. Both C (the log-law intercept) and κ (the von Kármán constant) are empirically derived universal constants, here set to 5 and 0.41, respectively. In the outer region of the boundary layer, where the velocity profiles over relatively low- relief roughness and smooth walls should exhibit similarity (Townsend 1976), the velocity profile can be written in the velocity defect form

$$U_e^+ - U^+ = -\frac{1}{\kappa}\ln\left(\frac{y+\varepsilon}{\delta}\right) + \frac{2\Pi}{\kappa}w(y/\delta) \quad (2)$$

where U_e^+ is the freestream velocity (normalized by inner units), δ is the boundary layer thickness, and $\frac{2\Pi}{\kappa}w(y/\delta)$ is the Coles wake function (Coles 1956), which is constant between

biofilms and the smooth wall (Walker et al. 2013; Murphy et al. *submitted*). $\prod$ is the wake parameter, and *w* the wake function. Because the Coles wake function can be held constant and the roughness function is not present in this equation, this formulation of the velocity profile is useful for calculating U_τ and ε by finding which pair of values gives the best fit of the rough-wall velocity profile to the smooth wall velocity profile (where ε is zero and U_τ is already known).

We used the double-averaged velocity profile (Nikora et al. 2007) to estimate the integrated bed shear stress and skin-friction coefficient over the different biofilm surfaces. To do this, we used a velocity defect matching method based on the assumption that the roughness effects of biofilms are constrained to the inner region of the boundary layer (Townsend 1976; Flack et al. 2005; Walker et al. 2013), described in Murphy et al. (*submitted*), to find U_τ, ε, and ΔU^+. This method iteratively changes U_τ and ε until the best fit between the rough wall velocity defect profile, and a smooth wall flow (taken in the same facility as the biofilm data) is found. Then ΔU^+ is found by matching the rough wall log region, in log-law form, to the smooth wall data. This method was validated using the standard modified Clauser chart for rough walls (Perry and Li 1990; Schultz and Myers 2003), as well as the total stress method (Ligrani and Moffat 1986), which is commonly used in the environmental fluid mechanics literature (Reidenbach et al. 2006; Reidenbach et al. 2009) but is known to be slightly less accurate than the Clauser method (Schultz and Flack 2007).

Our results presented here show that, hydrodynamically, biofilms add roughness to the surface, resulting in a downward shift of the streamwise velocity profile compared with flow over a smooth wall (Fig. 4A) for all tests, except for one of the sparse biofilm plates. Note that the data here are plotted with the vertical dimension (y) on the x axis, and in inner units, for

better comparison with other rough wall analyses. Plotted in velocity defect form (Fig. 4B), good collapse of the mean velocity profiles is achieved through the determination of U_τ.

The downward shift of the log- law velocity profiles is the result of momentum being lost to friction and pressure (form) drag on the roughness elements (Flack et al. 2012), which, integrated over the surface, are the bed shear stress and the pressure distribution, respectively, and make up the total shear stress, τ (Leonardi et al. 2007). The integrated friction velocity (U_τ), determined from the streamwise averaged mean velocity profile, is elevated over the biofilms compared with the smooth wall (Table 2), aside from the sparsest biofilm, labeled Sparse 1. Keeping in mind that the two patchy tests were conducted on the same plate, it is interesting to note that they have very different integrated U_τ values (0.081 and 0.072 m s^{-1}), highlighting the dependence of even the integrated shear velocity on local bed characteristics.

The mean velocity profiles were used to calculate roughness effects on the flow (Table 2). The skin-friction coefficient ($C_\mathrm{f} = 2\frac{{U_\tau}^2}{{U_e}^2}$) appears to be most strongly influenced by the percent cover of the biofilm, as opposed to the physical roughness height (measured as the mean peak-to-trough distance) of the biofilm (Fig. 5). This could be due to the flapping streamers of the biofilm being most important to removing momentum from the flow, as opposed to the roughness elements of the biofilm. The effective sand grain height ($k_s^+ = \exp(\kappa(\Delta U^+ + 3.3))$, as a function of ΔU^+, also appears dependent on the biofilm percent cover more than the physical roughness height (Table 2). However, the calculation of k_s^+ is only valid in the fully rough regime, so values for the sparse biofilms should be taken with caution (Flack et al. 2012).

The local value of U_τ was calculated for each vertical velocity profile in each frame. The local values of U_τ vary considerably in the streamwise direction over all of the biofilms except one of the sparse tests (Sparse 1), with especially pronounced variability over both patchy

biofilms and the Sparse 2 biofilm (Fig. 6B, C & E). This has implications for biofouling community development. As the biofilm matures and is exposed to high shear, biofilm sloughs off, resulting in patchiness. As our results show, this patchiness then enhances local bed shear stresses, potentially resulting in more localized sloughing. Additionally, sloughing off of biofilm can be a dispersal mechanism for biofilms, so patchiness of the biofilm, whether due to biofilm senescence, grazing, or hydrodynamic forces, could then enhance dispersal of the biofilm over the surface. Biofilms are typically the first fouling organisms to colonize aquatic surfaces, and in many cases biofilms act to prime the surface, making it more favorable for the settlement and growth of other fouling organisms such as macroalgaes and invertebrates (Qian et al. 2007). The variability in local bed shear stress observed in this study, especially over the patchy biofilms, may affect where larvae settle on a biofilm fouled surface, and whether the larvae are able to stick to the surface.

As pointed out in Antonia and Krogstad (2001), the roughness function, and by extension U_τ, do not fully describe the characteristics of a rough wall. Different types of roughness, such as 2D versus 3D roughness, can have similar ΔU^+ values but different effects on turbulence structure and, hence, momentum transport. Spatially explicit RSS shows significant heterogeneity of the RSS in the inner and overlap regions (Fig. 7) over the uniform and patchy biofilms (Fig. 7A, C, & G), but is fairly homogeneous over the Sparse 1 biofilm (Fig. 7E). The *tke*, not shown, exhibits similar spatial patterns to the RSS. The spatial variability of RSS (and *tke*), is most pronounced over the patchy biofilms (only Patchy 1 is shown) and the Sparse 2 biofilm. These results also show that the RSS is elevated over all of the biofilms, including the most sparse (Sparse 1), when normalized by the freestream velocity (Fig. 7B, D, F & H).

The streamwise-averaged Reynolds stresses (u'^{2+}, $-u'v'^{+}$, v'^{2+}), normalized by U_τ^2, are given in Fig. 8. The sparse and uniform biofilms demonstrate good collapse with the smooth wall Reynolds stresses in the outer layer, however the patchy biofilms, which collapse with each other, diverge until about $(y+\varepsilon)/\delta = 0.9$ which is well into the outer layer. All of the biofilms elevate the shear and wall-normal stresses compared with the smooth wall, and all of the non-uniform biofilms have elevated shear ($-u'v'^{+}$) and vertical (v'^{2+}) stresses compared with the uniform biofilm (Fig. 8B & C), even the sparse biofilm, when normalized by the shear velocity. Smooth wall streamwise Reynolds stress (u'^{2+}) classically exhibits a peak adjacent to the wall, where viscous forces dominate, which is not seen over the uniform biofilm or over the Patchy 1 biofilm (Fig. 8A), indicating that these biofilms are hydraulically rough (Ligrani and Moffat 1986). Hence, for these surfaces, the roughness of the biofilm is larger than the viscous sublayer and the pressure (form) drag dominates over the viscous stress. The other biofilms, however, appear to have a near-wall peak, indicating that these fouled surfaces are not in the fully rough regime (Brzek et al. 2008). For the hydraulically rough biofilms, the broad peak between about $u'^{2+} = 3$ and $u'^{2+} = 4$ is similar in shape and magnitude to that seen in other studies looking at fresh water and marine biofilms (Walker at al. 2013; Schultz and Swain 1999).

Worth noting as well are the shape and location of the peaks in the Reynolds shear stresses (Fig. 8B). Biofilms Patchy 1, Patchy 2 and Sparse 1 all have a plateau region in the RSS profile, which spans the largest portion of the boundary layer for Patchy 1. The uniform biofilm has a broad peak that I shifted away from the wall in comparison to the smooth wall, whereas the Sparse 2 biofilm has a sharper, near wall peak. The wall-normal Reynolds stress profiles over the biofilms as well as the smooth wall have blunt peaks (Fig. 8C). Biofilm Patchy 1 has a broad peak the furthest from the wall, at about $(y+\varepsilon)/\delta = 0.4$ and Sparse 2 has a sharper peak close

to the wall. This near- wall peak in $v'^{2+}$is also seen over some heavy biofilm fouling (Walker et al. 2013). The sharp, near- wall peak in the Reynolds shear stress and wall-normal stress profiles for the Sparse 1 biofilm are similarly seen over fine mesh 3-dimensional roughness, in comparison with 2-dimensional roughness from rods, which have broad blunt peaks, shifted away from the wall (Antonia and Krogstad 2001), similar to what we see here for the uniform biofilm.

The dispersive stress ($\tilde{u}\tilde{v}$), normalized by the square of the freestream velocity, is increased in magnitude over the patchy biofilms, and sparse biofilm Sparse 1, as compared with the uniform biofilm (Fig. 9). The dispersive stress is highly variable in the streamwise direction. Over a uniform biofilm, there are localized regions of heightened dispersive stress right at the biofilm surface (Murphy et al. *submitted*). Biofilm Patchy 1 has a similar pattern of dispersive stresses to the uniform biofilm, with hotspots of heightened stress located at the biofilm surface that appear to correspond with larger roughness elements (Fig. 10A). Biofilms Sparse 2 and Patchy 2 have larger hotspot areas that are elongated in the streamwise direction (Fig. 10B & C). In addition to near-bed hotspots, these two surfaces have areas of enhanced dispersive stress elevated off the bed, at the height of the crest of the biofilm roughness elements. In all cases, the dispersive stress is considerably smaller than the RSS (Fig. 9). Dispersive stresses are important to mass transport, especially in canopy flows (Poggi et al. 2004), so the layer of increased dispersive stress over the patchy and sparse biofilms may contribute to locally hotspots of nutrient transport related to the canopy flow over the more rugose biofilms. The *tke* production, ($P = -u'v'\frac{\partial U}{\partial y}$), has a near-bed peak that is stronger and sharper for the patchy and uniform biofilms compared with the sparse biofilms (Fig. 11). Spatially explicit plots of P^+ over a patchy and a sparse biofilm reveal that *tke* production is highly localized (Fig. 12). P^+ appears to be

enhanced downstream of some of the protruding biofilm structures, and in the Sparse 1 panel (Fig. 11 B) P^+ is only elevated over the more rough areas of biofilm, with little *tke* production in the low relief area of the biofilm in the middle of the frame.

Coherent structures

Coherent structures in turbulent boundary layer flows are key to momentum and mass transport to and from the bed. Quadrant analysis is a conditional averaging technique used to determine the strength of turbulent sweeps (where high momentum flow in the outer layer travels towards the bed; Q4) and ejections (where low momentum fluid from the near- bed region is ejected higher up into the boundary layer; Q2) (Wallace 2016). Here the quadrant-hole technique (Lu and Willmarth 1973) was used to determine the relative contributions of strong ($|u'v'| > H\sigma_u\sigma_v$; where $H = 4$ and σ_{u_i} is the standard deviation of u_i at a given location) instantaneous vertical turbulent events to the Reynolds shear stress, where these events are located in the boundary layer, and the streamwise variability of the events over the different biofilms (Fig. 13). Q2 events are strongest in the outer layer, while Q4 events dominate at the bed, as is typical over rigid roughness and canopy flows (Raupach 1981; Yue et al. 2007). All of the biofilms, aside from Sparse 1, have similar magnitudes of high energy turbulent ejections near the bed. The magnitude of high energy turbulent sweeps, however, is dependent on the biofilm surface, with the patchy biofilms both having large, sharp peaks (Fig. 14), indicating that for the patchy biofilm, entrainment of high velocity flow down towards the bed is especially important. This may mean that there is stronger vortex shedding from the patchy biofilms, because Q4 events over canopies are a result of prograde (rotating with the direction of flow) vortices being shed off

of the vegetation at the canopy top. This likely results in increased transport of scalar quantities, such as free swimming larvae or sediment, to the biofilm surface (Hendriks et al. 2006).

A measure of the rotational flow is the swirling strength, λ_{ci}, which is similar to the vorticity, ω, however, the vorticity includes shear whereas the swirling strength is a measure solely of the rotational component of the fluid motion (Zhou et al. 1999). The swirling strength is the imaginary part of the complex eigenvalue of the local instantaneous velocity gradient. The λ_{ci} is greatest at the bed, and is elevated over the patchy, and Sparse 1, biofilms compared to the uniform biofilm (Fig. 15). Strong rotational flow extends further into the boundary layer over these biofilms as compared with the uniform biofilm, as well, suggesting stronger vortex shedding over the rougher biofilms. Instantaneous λ_{ci} and velocity fields are also illustrative of this. Therefore, Galilean decomposition was used to investigate the small-scale eddies in the flow. This technique removes the convective velocity from the instantaneous velocity field so that $u_c = u - U_c$, where U_c is the Galilean convection velocity (Adrian et al. 2000; Volino et al. 2007) as a percentage of the freestream velocity. Galilean-decomposed instantaneous velocity fields were examined to identify vortices and coherent structures within the flow. These vortices are identified using the swirling strength, λ_{ci}. Here, the local instantaneous vorticity is used to give a sign (direction of rotation) to the swirling strength so that prograde (rotating in the direction of the mean shear) and retrograde (rotating the opposite direction of the mean shear) can be distinguished (Wu and Christensen 2006)

Galilean-decomposed instantaneous velocity fields over the five biofilms imaged, with a convective velocity of $0.7U_e$ removed, are shown in Figure 16. The Galilean decompositions are plotted over λ_{ci}, the swirling strength, to highlight locations of rotational flow. Location of prograde rotation (rotating in the direction of the flow) are shaded in blue, and locations of

retrograde rotation (rotating in the direction opposite the mean flow) are red. Because most of the freestream velocity is removed from each velocity vector, this highlights lower- speed vortices near the bed, which occur more often in packets. These vortices entrain fluid, moving high-momentum fluid downwards to the bed and low-momentum fluid upwards. As in other turbulent boundary layer flows, this mechanism of momentum transport appears important in biofilm-bounded flow (Volino et al 2009; Wu & Christensen, 2010). The uniform and patchy biofilms appear to have prograde vortex streets being shed from the wall (Fig. 16A, B & C). Biofilm Sparse 1 has noticeably smaller locations of rotating flow (Fig. 16D), and the instantaneous flow appears more disorganized than over the other biofilms.

Conclusions

We found that non-uniform biofilms enhance vertical momentum transport in the boundary layer, at least in part due to setting up local plane mixing layers where the velocity profiles are S-shaped. However, the drag coefficient of the biofilms appears to correlate most strongly with percent cover of the biofilm, rather than peak-to-trough distance, which means that the uniform biofilm has the greatest increase in surface drag despite not having the largest roughness elements. This may be due to the cumulative effects of a larger area of compliant surface, and a larger number of flapping streamers removing momentum from the flow.

Biofilms are also important to fouling community development. Biofilms are typically the first fouling community to settle on an aquatic surface, and biofilm fouled surfaces are more likely to be colonized by other fouling organisms than non- biofilm- fouled surfaces. This can mean that biofilm growth sets the stage for attachment of hard fouling organisms, such as

barnacles, that have an even greater drag penalty on a ship. Larvae may be induced to settle by hydrodynamic cues related to roughness (Fuchs et al. 2007), or by chemical cues released by the biofilm (Hadfield and Paul 2001). Turbulence is critical to larval settlement, both for delivery of larvae to the bed (Eckman 1990; Hata et al. 2017), as well as triggering of sinking behavior when larvae recognize the hydrodynamic cues of a favorable settlement location (Koehl 2007). The results presented here indicate that biofilm topography may influence a biofilm's role in priming a surface for fouling community succession. The generation of stronger turbulent sweeps over patchy biofilms is likely better able to entrain larvae and transport them to the surface (Hata et al. 2017). Additionally, the pockets of lower shear stress and lower momentum flow that are especially evident in the non-uniform biofilm may provide suitable location for the settlement of larvae.

Given the increase in energy of the vortices over the patchy biofilms and the exposed bed under patchy biofilms, non- uniform biofilms may in fact increase vertical fluxes of mass, momentum, and heat to the underlying substrate. While relatively uniform biofilms enhance bed stability of sediments (Decho 2000), and decrease vertical fluxes of solutes to the bed (for example, decreasing nutrient availability to corals), our results show that patchy biofilms increase vertical transport by shedding stronger vortices that can penetrate to the bed, if it is exposed. The high energy loss of biofilms, possibly due to the flapping streamers, combined with the low relief of the biofilms, means that vertical transport can be greatly increased, albeit in a spatially heterogeneous manner. Channel flows over large roughness elements exhibit mixing layer behavior similar to flows over vegetation canopies. The patchy biofilms also demonstrated this mixing layer in some locations over the bed, which may help to explain the larger turbulent momentum fluxes over the non-uniform biofilms and the highly localized increases in P^+.

The growth and morphology of biofilms is dependent on the hydrological conditions, and biofilms themselves alter the hydrodynamics. Biofilms grow patchily, and they can slough off under high shear. As the biofilm community develops, there are feedbacks between the biofilm community and hydromechanics (Besemer et al. 2007). As biofilms get too thick for deeper biofilms to access nutrients, senescence and sloughing, resulting in biofilm patchiness, may enhance turbulent transport of metabolites to the bed, as evidenced by the spike in turbulent sweep strength over patchy biofilms. Algal biofilms are important in many contexts. The complex hydrodynamics of biofilms in turbulent flow are likely to have consequences to ecosystem processes affected by biofilms as well as ship performance.

References

Adrian RJ, Christensen KT, Liu ZC. 2000. Analysis and interpretation of instantaneous turbulent velocity fields. *Experiments in fluids*. 29(3):275-290.

Andrewartha J, Perkins K, Osborn SJ, Walker G, Henderson A, Hallegraeff G. 2010. Drag force and surface roughness measurements on freshwater biofouled surfaces. *Biofouling*. 26:487-496.

Antonia RA, Krogstad, PÅ. 2001. Turbulence structure in boundary layers over different types of surface roughness. *Fluid Dynamics Research*, *28*(2):139-157.

Battin TJ, Kaplan LA, Newbold JD, Hansen CME. 2003. Contributions of microbial biofilms to ecosystem processes in stream mesocosms. *Nature*. 426:439-442.

Besemer K, Singer G, Limberger R, Chlup A-K, Hochedlinger G, Hödl I, Baranyi C, Battin TJ. 2007. Biophysical controls on community succession in stream biofilms. Appl. Environ. Microbiol. 73(15):4966-4974.

Brzek BG, Cal RB, Johansson G, Castillo L. 2008. Transitionally rough zero pressure gradient turbueltn boundary layers. *Exp Fluids*. 44:115-124.

Coles D. 1956. The law of the wake in the turbulent boundary layer. *J Fluid Mech*. 1:191-226.

De Beer D, Kühl M. 2000. Interfacial processes, gradients and metabolic activity in microbial mats and biofilms. p. 374–394. In B.Boudreau and B. B. Jørgensen [eds.], The benthic boundary layer. Oxford Univ. Press.

Decho AW. 2000. Microbial biofilms in intertidal systems: an overview. Continental Shelf Research. 20:1257-1273.

Eckman JE. 1990. A model of passive settlement by planktonic larvae onto bottoms of differing roughness. *Limnol Oceanogr.* 35:887-901.

Flack KA, Schultz MP, Rose WB. 2012. The onset of roughness effects in the transitionally rough regime. *International Journal of Heat and Fluid Flow*. 35:160-167.

Flack KA, Schultz MP, Shapiro TA. 2005. Experimental support for Townsend's Reynolds number similarity hypothesis on rough walls. *Phys. Fluids.* 17:035102.

Fuchs HL, Neubert MG, Mullineaux LS. Effects of turbulence-mediated larval behavior on larval supply and settlement in tidal currents. *Limnology and Oceanography*. 2007 May 1;52(3):1156-65.

Hadfield MG, Paul VJ. 2001. Natural chemical cues for settlement and metamorphosis of marine invertebrate larvae. In: McClintock JB, Baker W (eds) Marine chemical ecology. CRC Press, pp 431–461.

Hansen JCR, Reidenbach MA. 2012. Wave and tidally driven flows in eelgrass beds and their effect on sediment suspension, *Marine Ecology Progress Series*, 448, 271-287.

Hata T, Madin JS, Cumbo VR, Denny M, Figueiredo J, Harii S, Thomas CJ, Baird AH. Coral larvae are poor swimmers and require fine-scale reef structure to settle. *Scientific Reports*. 7:2249.

Hendriks IE, Van Duren LA, Herman PMJ (2006) Turbulence levels in a flume compared to the field: implications for larval settlement studies. *J Sea Res.* 55:15−29.

Koehl MAR. 2007. Mini review: Hydrodynamics of larval settlement into fouling communities. *Biofouling*. 23:357-368.

Krogstad PÅ, Antonia RA. 1999 Surface roughness effects in turbulent boundary layers. Exp Fluids. 27:450-460.

Krogstad PÅ, Antonia RA, Browne LWB. 1992. Comparison between rough- and smooth-wall turbulent boundary layers. J Fluid Mech. 245:599-617.

Leonardi S, Orlandi P, Antonia RA. 2007. Properties of d- and k-type roughness in a turbulent channel flow. *Physics of Fluids*. 19:125101

Ligrani PM, Moffat RJ. 1986. Structure of transitionally rough and fully rough turbulent boundary layers. *J Fluid Mech.* 162:69–98

Lu SS, Willmarth WW. 1973. Measurements of the structure oft he Reynolds stress in a turbulent boundary layer. *J Fluid Mech*. 60(3):481-511.

Mignot E, Barthelemy E, Hurther D. 2008. Double-averaging analysis and local flow characterization of near-bed turbulence in gravel-bed channel flows. *Fluid Mech*. 618:279-303.

Mignot E, Barthelemy E, Hurther D. 2009. On the structure of shear stress and turbulent kinetic energy flux across the roughness layer of a gravel-bed channel flow. *J Fluid Mech.* 638:423-452.

Murphy EAK, Barros JM, Schultz MP, Flack KA, Steppe CN, Reidenbach MA. 2017, The turbulent boundary layer structure over diatomaceous slime fouling. *Tenth International Symposium on Turbulence and Shear Flow Phenomena*, Chicago, IL, USA.

Murphy EAK, Barros JM, Schultz MP, Flack KA, Steppe CN, Reidenbach MA. *Submitted*. Roughness effects of diatomaceous slime fouling on turbulent boundary layer hydrodynamics.

Nepf HM, Vivoni ER. 2000. Flow structure in depth-limited, vegetated flows. J Geophys Res. 105:28547-28557.

Nikora V, McEwan I, McLean S, Coleman S, Pokrajac D, Walters R. 2007. Double-averaging concept for rough-bed open-channel and overland flows: Theoretical background. *J Hydraul Eng*. 133(8):873-883.

Perry AE, Li JD. 1990. Experimental support for the attached-eddy hypothesis in zero-pressure-gradient turbulent boundary layers. J Fluid Mech. 218:405-438.

Qian P-Y, Lau SCK, Dahms H-U, Dobretsov S, Harder T. 2007 Marine biofilms as mediators of colonization by marine macroorganisms: Implications for antifouling and aquaculture. *Mar Biotechnol* **9**, 399-410. (doi:10.1007/s10126-007-9001-9)

Raupach MR. 1981. Conditional statistics of Reynolds stress in rough-wall and smooth-wall turbulent boundary layers. *J Fl Mech*. 108:363-382.

Raupach MR, Finnigan JJ, Brunet Y. 1996. Coherent eddies and turbulence in vegetation canopies: The mixing-layer analogy. Boundary-Layer Meteorology. 78:351-382.

Reidenbach MA, Koseff JR, Koehl MAR. 2009. Hydrodynamic forces on larvae affect their settlement on coral reefs in turublent, wave-driven flow. *Limnol. Oceanogr.* 54(1):318-330.

Reidenbach MA, Limm M, Hondzo M, Stacey MT. 2010. Effects of bed roughness on boundary layer mixing and mass flux across the sediment-water interface. Water Resour Res. 46:W07530.

Reidenbach MA, Monismith SG, Koseff JR, Yahel G, Genin A. 2006. Boundary layer turbulence and flow structure over a fringing coral reef. *Limnol. Oceanogr.* 51(5):1956-1968.

Schultz MP. 2000. Turbulent boundary layers on surfaces covered with filamentous algae. *J Fluids Engin.* 122:357-363.

Schultz MP, Finlay JA, Callow ME, Callow JA. 2003. Three models to relate detachment of low form fouling at laboratory and ship scale. *Biofouling*. 19(S1):17-26.

Schultz MP, Flack KA. 2007. The rough-wall turbulent boundary layer from the hydraulically smooth to the fully rough regime. *J Fluid Mech*. 580:381-405.

Schultz MP, Bendick JA, Holm ER, Hertel WM. 2011. Economic impact of biofouling on a Naval surface ship. *Biofouling*. 27:87-98.

Schultz MP, Myers A. 2003. Comparison of three roughness function determination methods. *Exp. Fluids*. 35:372-379.

Schultz MP, Swain GW. 1999. The effect of biofilms on turbulent boundary layers. *J Fluids Eng* 121:44–51.

Schultz MP, Walker JM, Steppe CN, Flack KA. 2015. Impact of diatomaceous biofilms on the frictional drag of fouling-release coatings. Biofouling. 31:759-773.

Stocking JB, Rippe JP, Reidenbach MA. 2016. Structure and dynamics of turbulent boundary layer flow over healthy and algae-covered corals. *Coral Reefs*. 35(3):1047-1059.

Townsend AA. 1976. The Structure of Turbulent Shear Flow, 2nd edn. Cambridge University Press.

Volino, RJ, Schultz, MP, Flack, KA. 2007. Turbulence structure in rough- and smooth-wall boundary layers. *J Fluid Mech*. 592:263-293.

Volino RJ, Schultz MP, Flack KA. 2009. Turbulence structure in a boundary layer with two-dimensional roughness. *J Fluid Mech*. 635:75–101.

Walker JM, Sargison JE, Henderson AD. 2013. Turbulent boundary-layer structure of flows over freshwater biofilms. *Exp Fluids*. 54:1628.

Wallace JM. Quadrant analysis in turbulence research: History and evolution. *Annu Rev Fluid Mech.* 48:131-158.

Wu Y, Christensen KT. 2006. Population trends of spanwise vortices in wall turbulence. *J Fluid Mech.* 568:55-76.

Wu Y, Christensen KT. 2007. Outer-layer similarity in the presence of a practical rough-wall topography. *Phys. Fluids*. 19:085108.

Wu Y, Christensen KT. 2010. Spatial structure of a turbulent boundary layer with irregular surface roughness. *J Fluid Mech.* 655:380-418.

Yue W, Meneveau C, Parlange MB, Zhu W, Van Hout R, Katz J. 2007. A comparative quadrant analysis of turbulence in a plant canopy. *Water Resources Research*. 43(5).

Zargiel KA, Coogan JS, Swain GW. 2011. Diatom community structure on commercially available ship hull coatings. Biofouling. 27:955-965.

Zhou J, Adrian RJ, Balachandar S, Kendall TM. 1999. Mechanisms for generating coherent packets of hairpin vortices in channel flow. *J Fluid Mech*. 387:353-396.

Tables

Table 2. Biofilm characteristics and PIV parameters.

	Biofilm thickness Mean *(mm)*	Biofilm coverage *(%)*	Mean peak-to-trough dist. *(mm)*	Max peak-to-trough dist. *(mm)*	Velocity vector spatial resolution (μm)	Field-of-view size width (*mm*) × height (*mm*)
Sparse biofilm 1	0.2	55	0.3	0.4	191	78.0×52.1
Sparse biofilm 2	0.6	85	0.8	2.3	210	85.8×57.3
Patchy biofilm 1	1.7	88	0.9	2.0	205	83.7×53.6
Patchy biofilm 2	1.7	88	0.7	1.4	201	82.1×51.2
Uniform biofilm	1.7	100	0.5	0.9	176	72.2×42.0

Table 2. Flow parameters of the biofilm-fouled plates, including the uniform biofilm and smooth wall data from Murphy et al. *Submitted*. $\boldsymbol{\delta^+}$ is the friction Reynold number. *Indicates that these surfaces are likely not in the fully-rough regime, and therefore values for k_s may not be valid

	$\boldsymbol{U_e}$ *(m s^{-1})*	$\boldsymbol{\delta}$ *(mm)*	$\boldsymbol{Re_\tau = \delta^+ = \delta U_\tau / \nu}$ $\times 10^3$	$\boldsymbol{U_\tau}$ Velocity defect *(m s^{-1})*	$\boldsymbol{U_\tau}$ Modified Clauser chart *(m s^{-1})*	$\boldsymbol{U_\tau}$ Total stress *(m s^{-1})*	$\boldsymbol{\Delta U^+}$	$\boldsymbol{k_s^+}$	$\boldsymbol{k_s}$ *(mm)*	$\boldsymbol{C_f}$ $\times 10^{-3}$
Smooth wall	1.2	33.5	1.6	-	0.047	0.044	-	-	-	2.9
Sparse biofilm 1	1.3	25.2	1.3	0.049	0.051	0.050	0	4*	0.1*	2.9
Sparse biofilm 2	1.3	26.2	1.8	0.063	0.069	0.071	6.5	56*	0.8*	4.9
Patchy biofilm 1	1.3	34.5	3.0	0.081	0.083	0.077	11.8	488	5.6	7.4
Patchy biofilm 2	1.3	34.9	2.7	0.072	0.074	0.078	9.4	182	2.3	5.8

Figures

Figure 1. (A) Uniform biofilm; (B) patchy biofilm; (C) sparse biofilm.

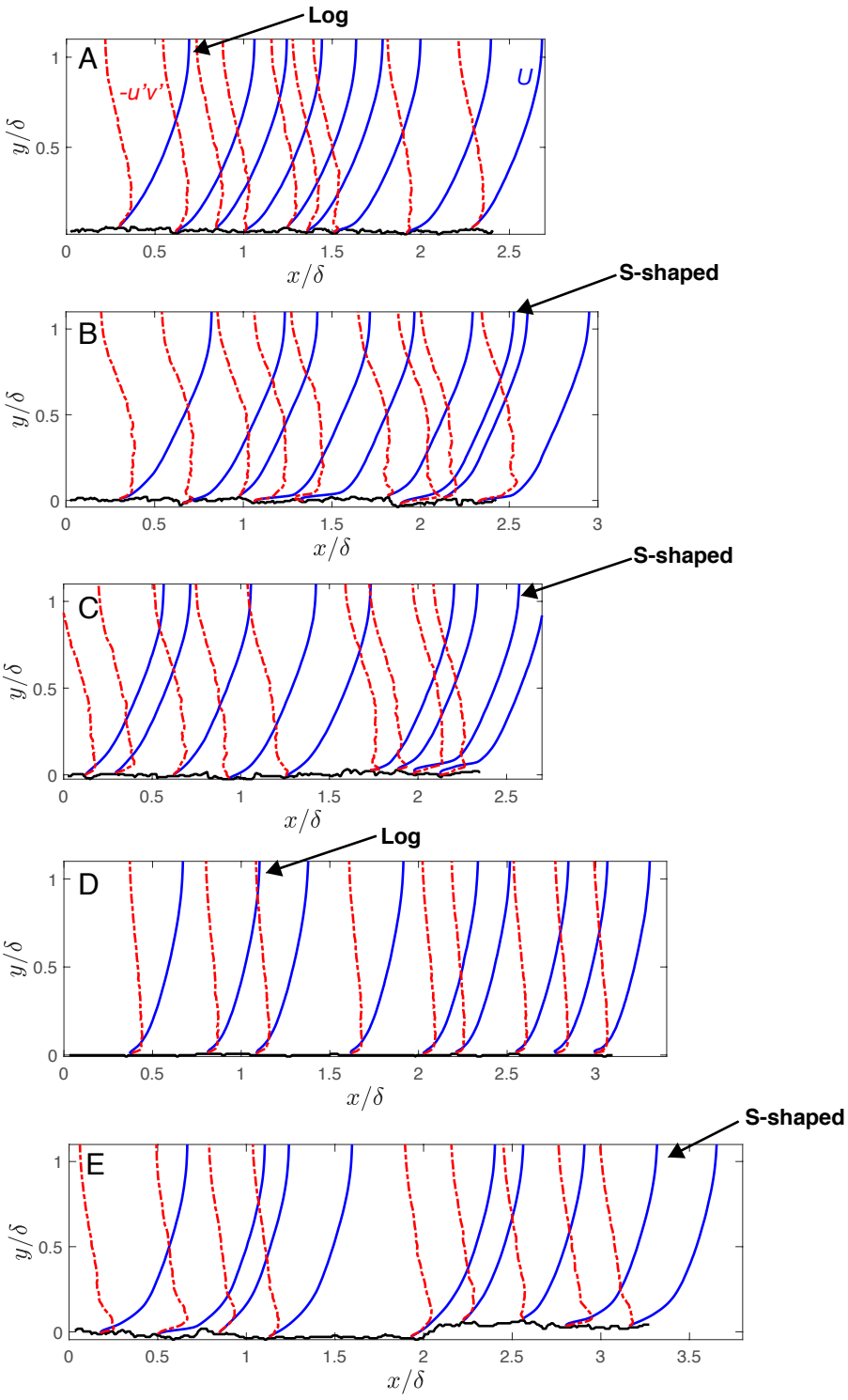
Log
A
-u'v'
U
y/δ
x/δ
S-shaped
B
S-shaped
C
Log
D
S-shaped
E

Figure 2. Selected streamwise velocity profiles (blue solid lines) and Reynolds shear stress profiles (red dashed lines) over uniform biofilm (A), patchy biofilm (B & C) and sparse biofilm (D & E). The solid black line shows the biofilm topography. Selected velocity profiles that demonstrate the log- law and S- shapes are marked, and the near- bed regions of these profiles are shown in Fig. 3.

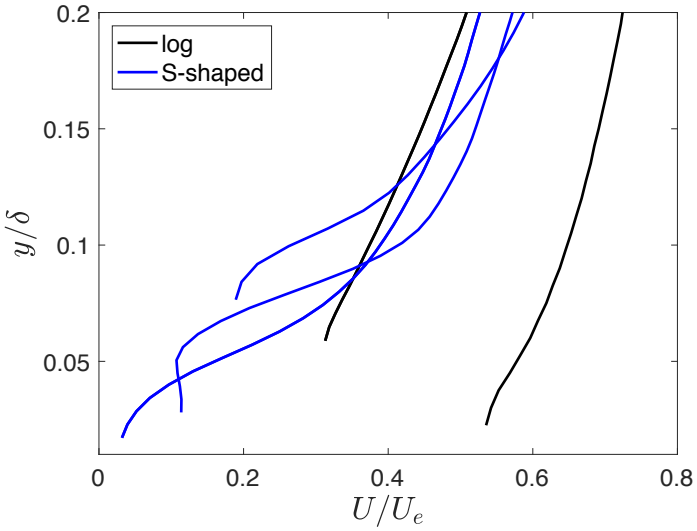

Figure 3. The near-bed region of the S-shaped (blue) and log- law (black) velocity profiles marked in Fig. 2.

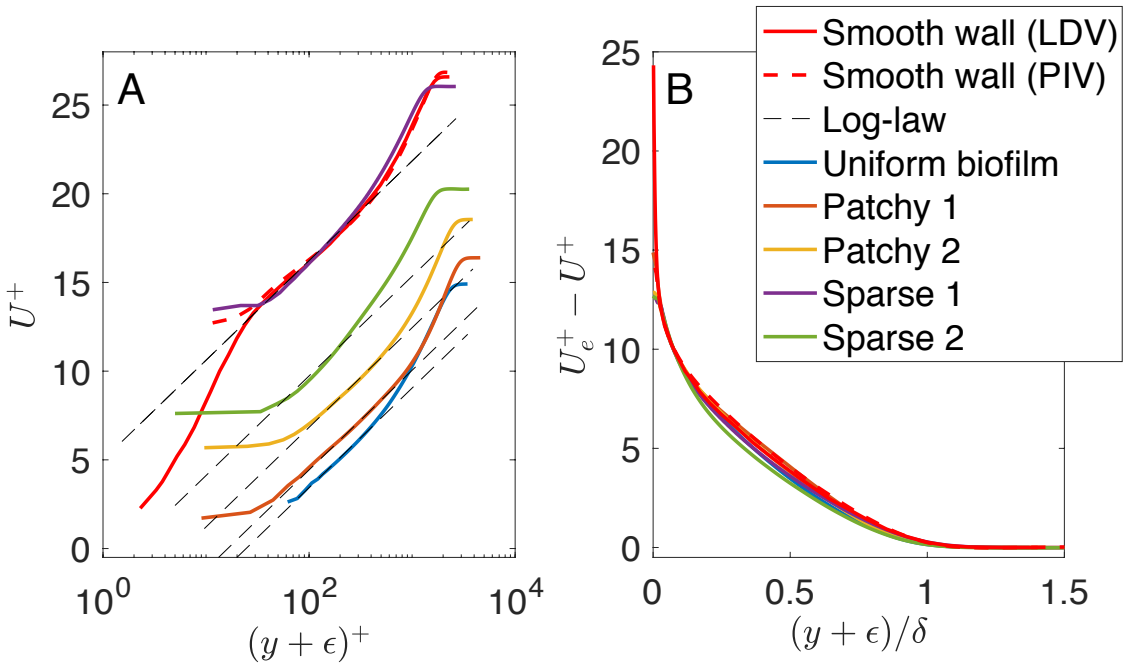

Figure 4. Streamwise averaged mean velocity profile over each biofilm, plotted in inner units (A) and in velocity defect form (B).

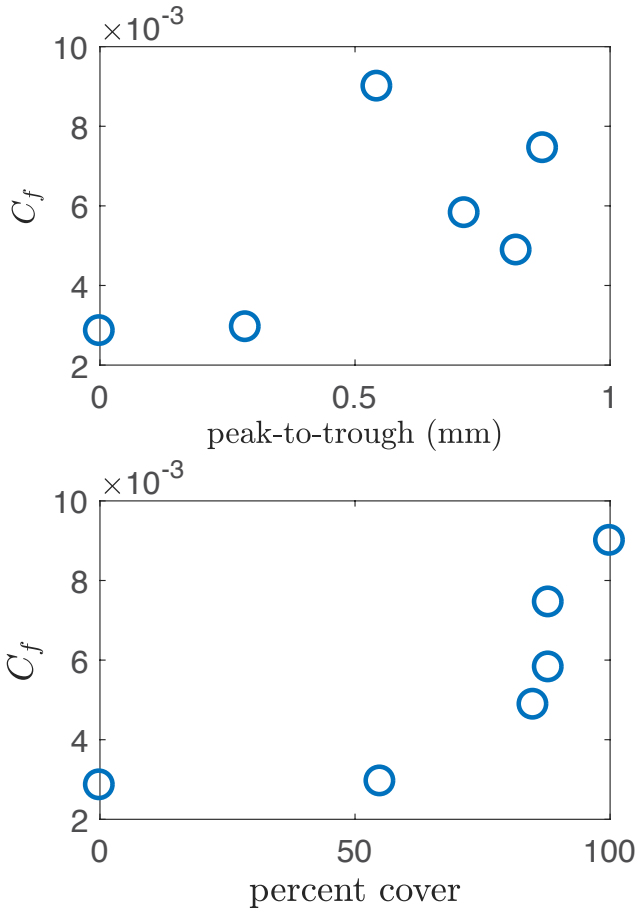

Figure 5. Skin friction and effective roughness height of the biofilm surfaces, plotted against the peak-to-trough distance of the biofilm surface and the percent cover of the biofilm.

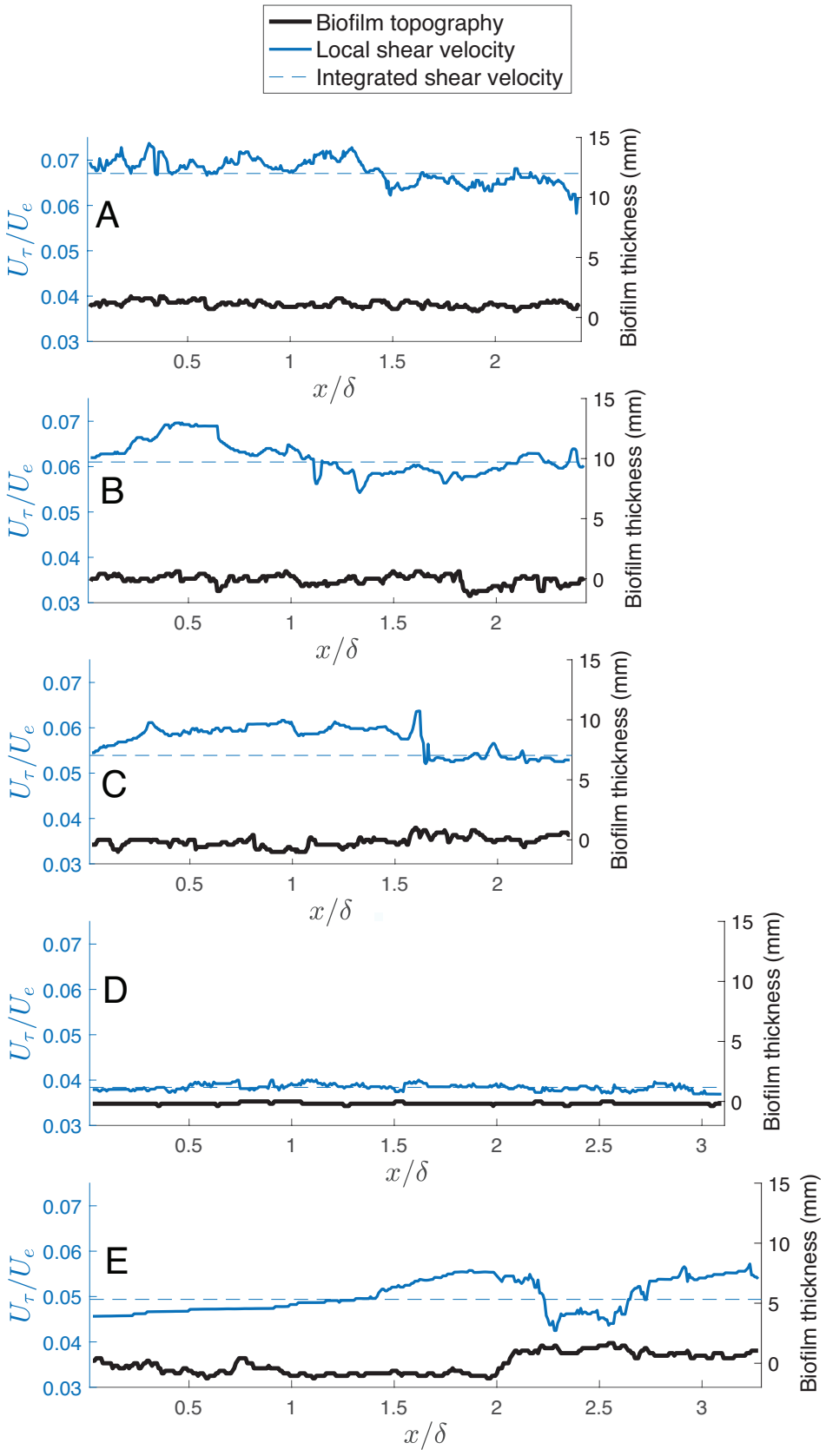
Biofilm topography
Local shear velocity
Integrated shear velocity
A
B
C
D
E
U_τ/U_e
x/δ
Biofilm thickness (mm)

Figure 6. Local shear velocity (U_τ) normalized by the freestream velocity (U_e) (solid blue line), plotted with the biofilm topography in each frame (solid black line). The integrated U_τ is given for comparison (dahed blue line). The biofilms are (A) uniform, (B) patchy 1, (C) patchy 2 (D) sparse 1 and (E) sparse 2.

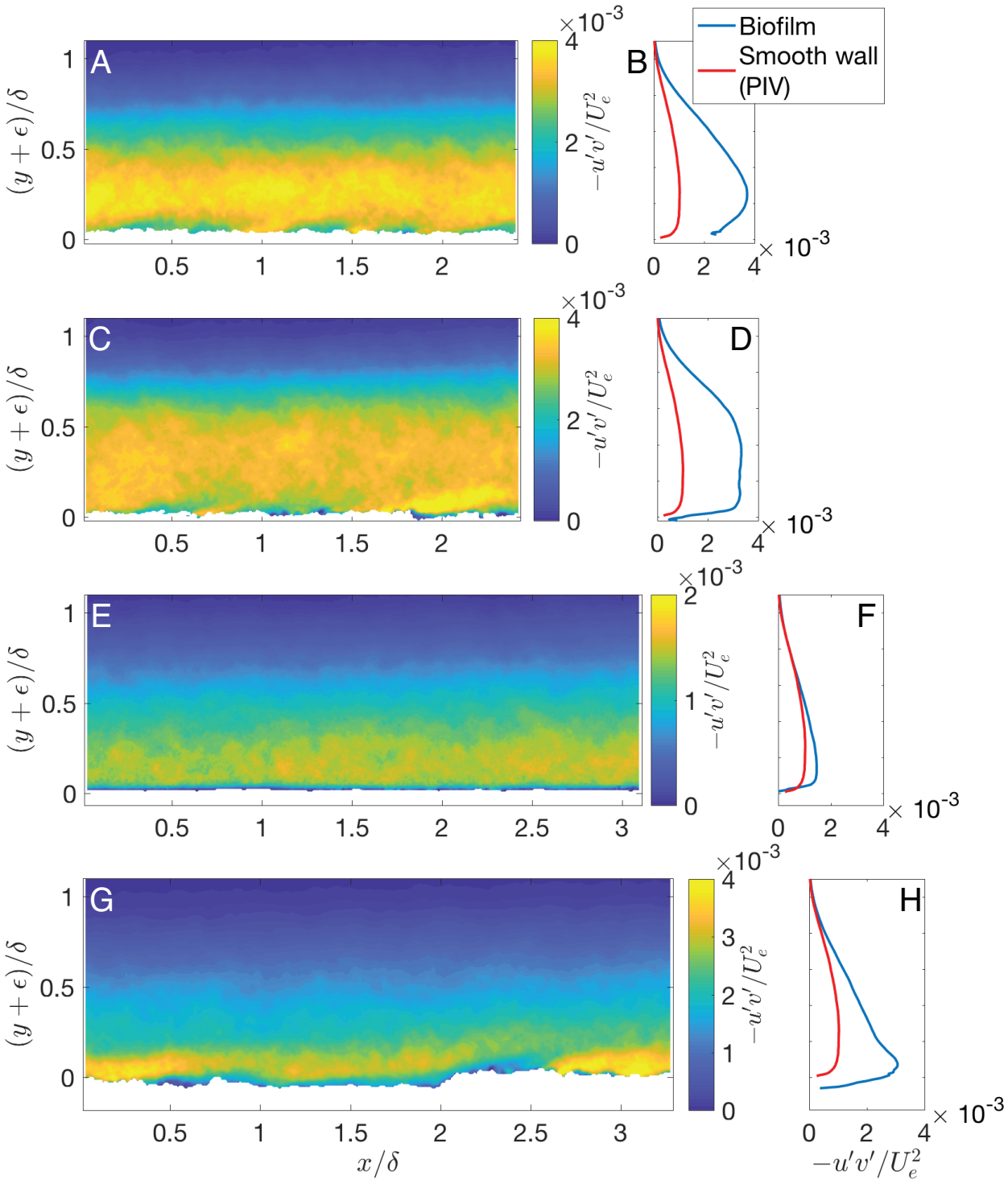

Figure 7. Reynolds shear stress, normalized by the freestream velocity, U_e. The x and y axes are normalized by the boundary layer thickness, δ. (A) Uniform; (C) Patchy 1; (E) Sparse 1; (G)

Sparse 2. To highlight the difference in magnitude of smooth wall and biofilm *RSS*, streamwise averages of these values are also plotted (B, D, F & H). Note that the scale of the colorbar for panel C differs from the rest, to better compare the spatial variability in RSS between the different surfaces. The scale of the x axis of the line plots are consistent for all panels.

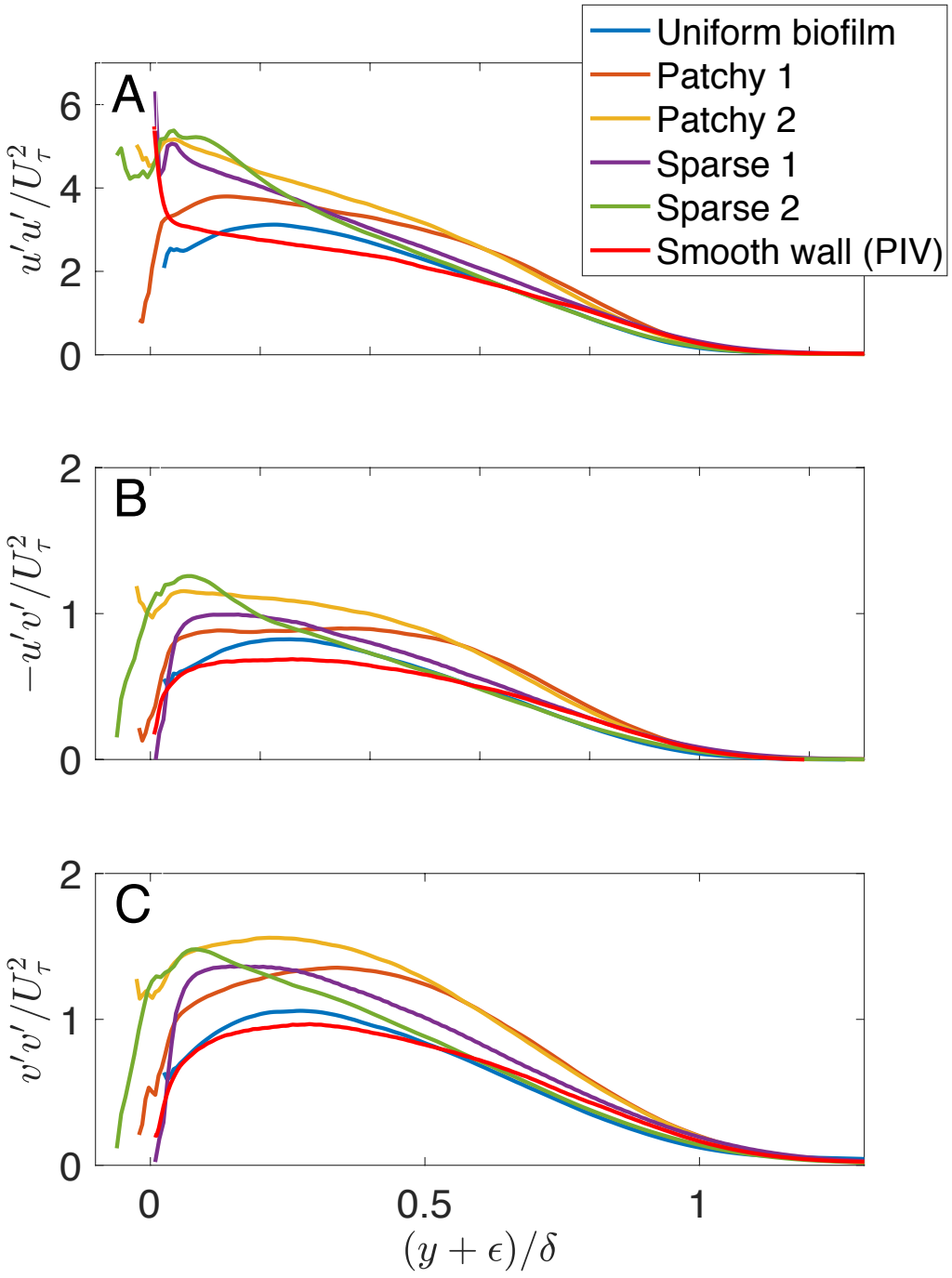

Figure 8. Streamwise averaged Reynolds stress profiles over each biofilm, plotted in inner units. The smooth wall case (red line) is given for comparison. (A) u'^{2+}; (B) $-u'v'^{+}$; (C) v'^{2+}

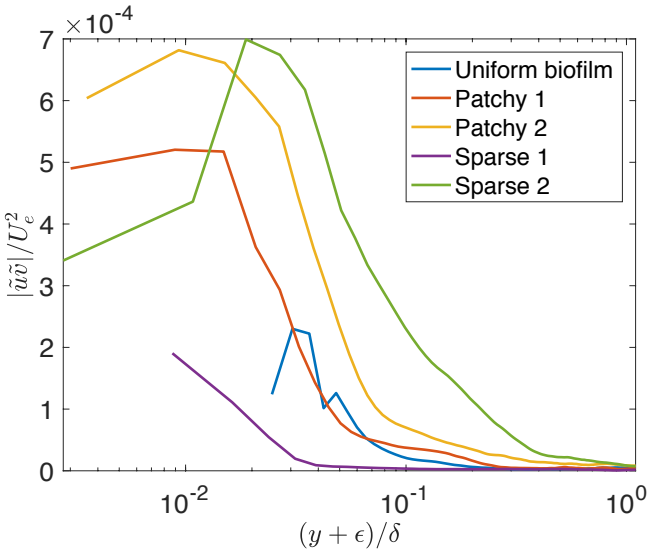

Figure 9. The magnitude of the dispersive stress over the different biofilms. Normalized in outer units.

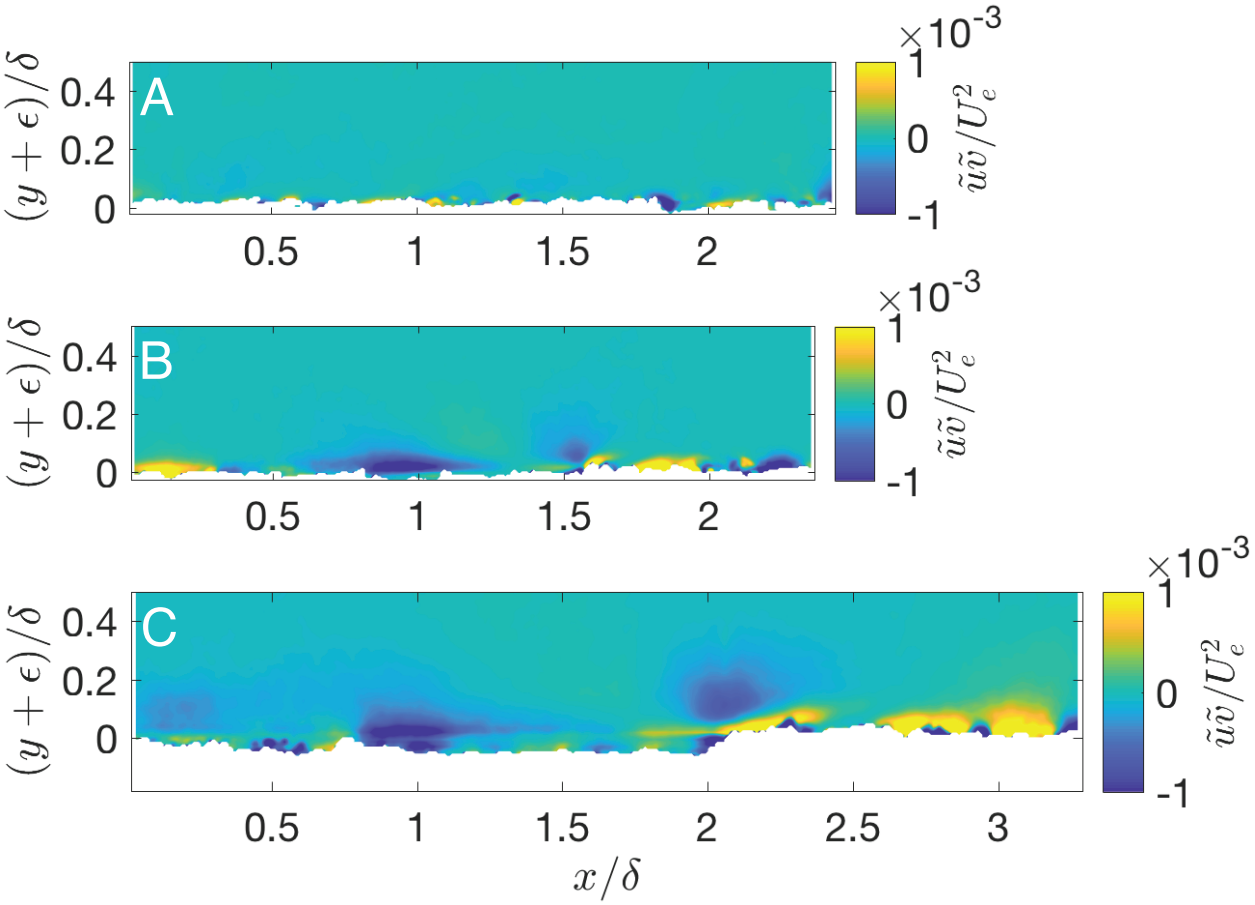

Figure 10. Dispersive stresses over three of the biofilms. (A) Patchy 1; (B) Patchy 2; (C) Sparse 2

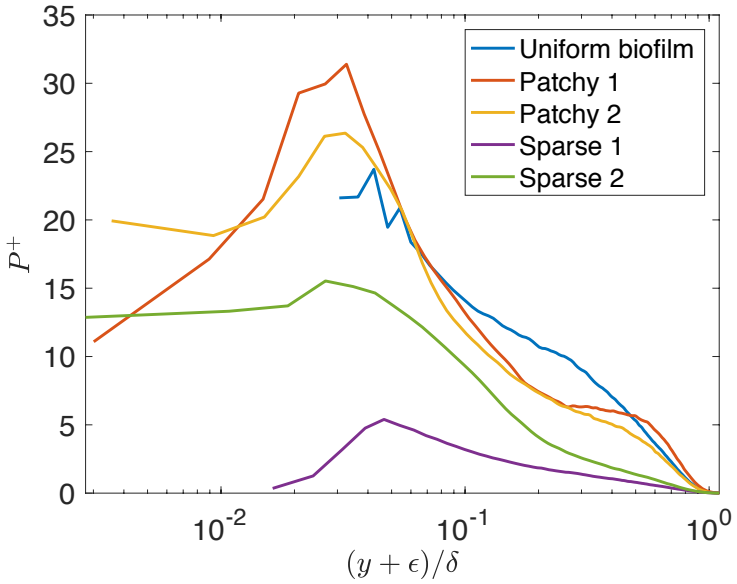

Figure 11. The production of *tke* over the different biofilms. P^+ is normalized by U_e^3/δ.

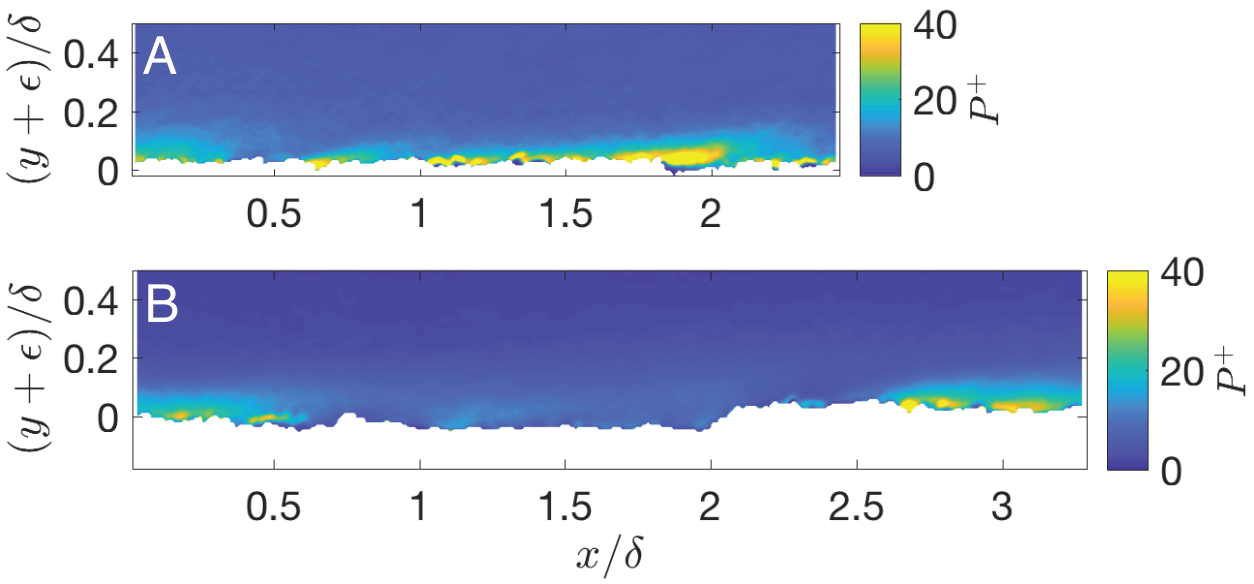

Figure 12. Turbulent kinetic energy production (P^+) over two of the tested biofilms. (A) Patchy 1; (B) Sparse 2. Each local vertical profile of U was smoothed with a smoothing spline before finding $\frac{\partial U}{\partial y}$ in P.

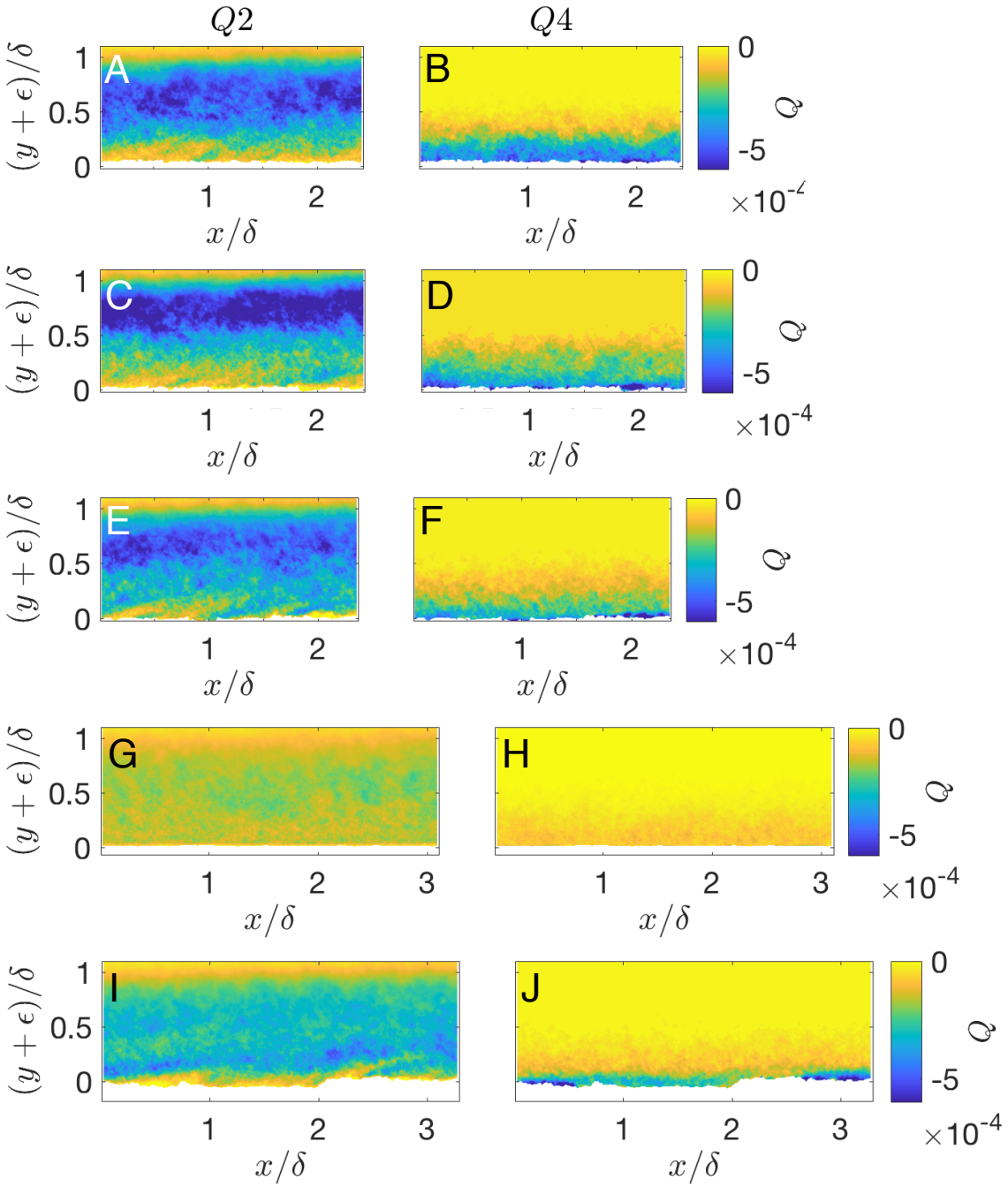
$Q2$
$Q4$
A
B
C
D
E
F
G
H
I
J
$(y+\epsilon)/\delta$
x/δ
∂
$\times 10^{-4}$

Figure 13. Quadrant-hole analysis with $H = 4$. (A & B) Uniform biofilm; (C & D) Patchy 1 biofilm; (E & F) Patchy 2 biofilm; (G & H) Sparse 1 biofilm; (I & J) Sparse 2 biofilm. Q2 and Q4 are normalized by the square of the freestream velocity.

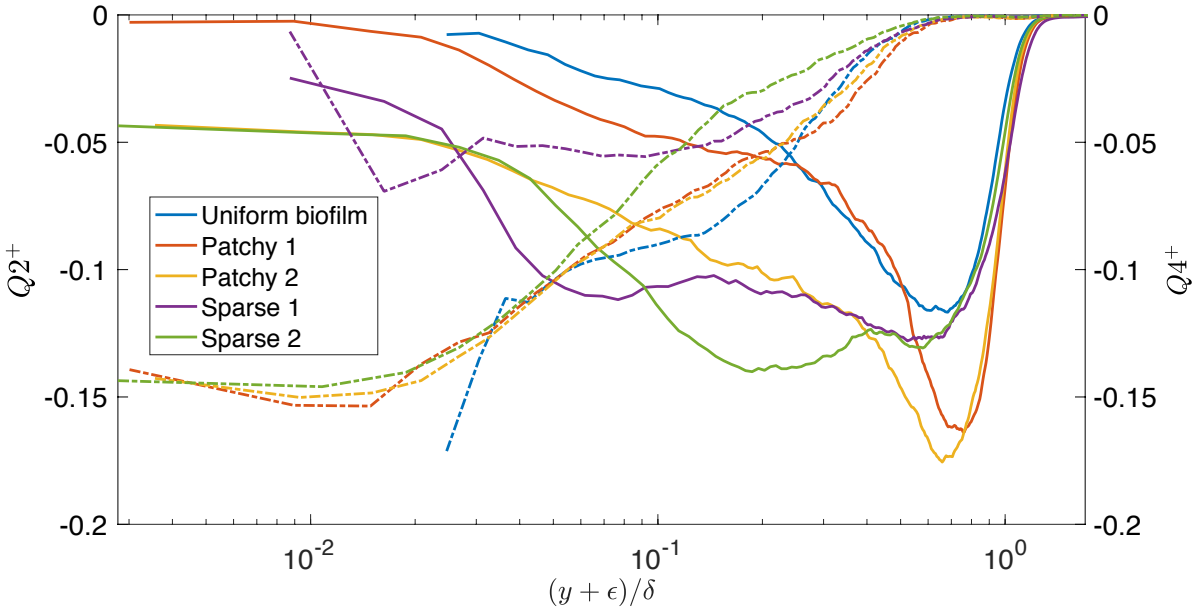

Figure 14. Double averaged quadrant-hole analysis ($H = 4$). Here, Q2 and Q4 are normalized in inner units (U_τ^2). Solid lines show events in Quadrant 2 (turbulent ejections) and dashed lines show events in Quadrant 4 (turbulent sweeps).

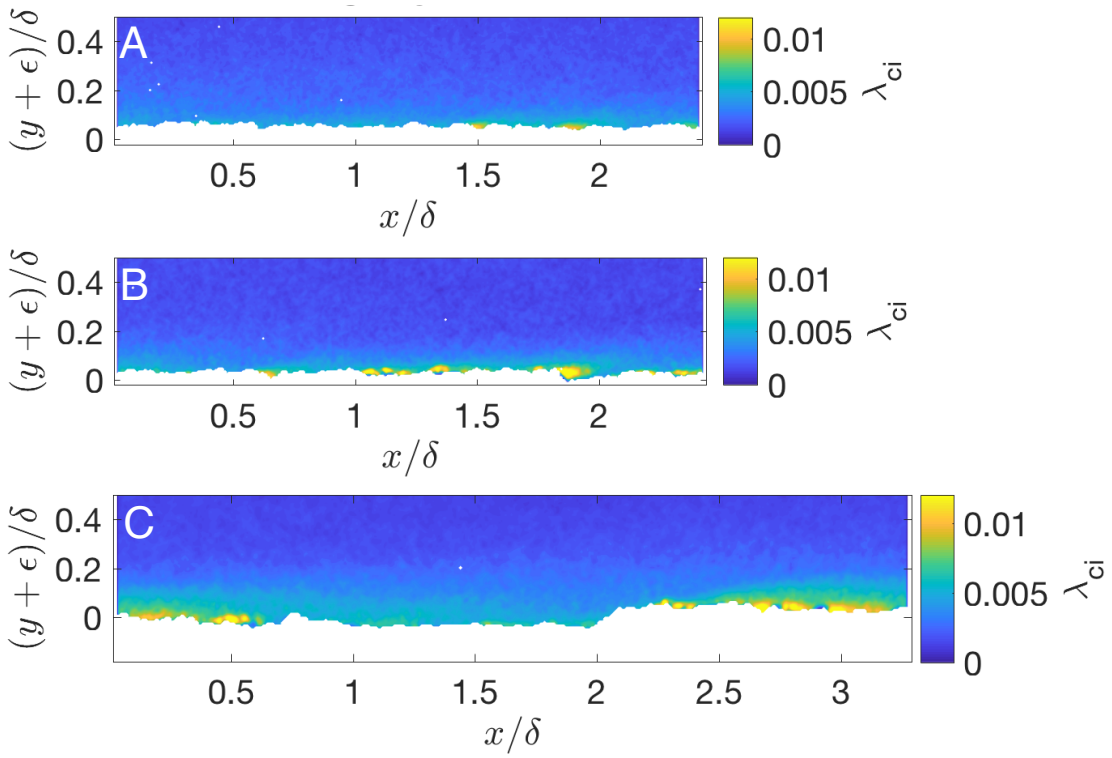

Figure 15. Swirling strength, λ_{ci}, normalized by the sign of the vorticity. (A) Uniform biofilm; (B) Patchy 1 biofilm; (C) is Sparse 2 biofilm.

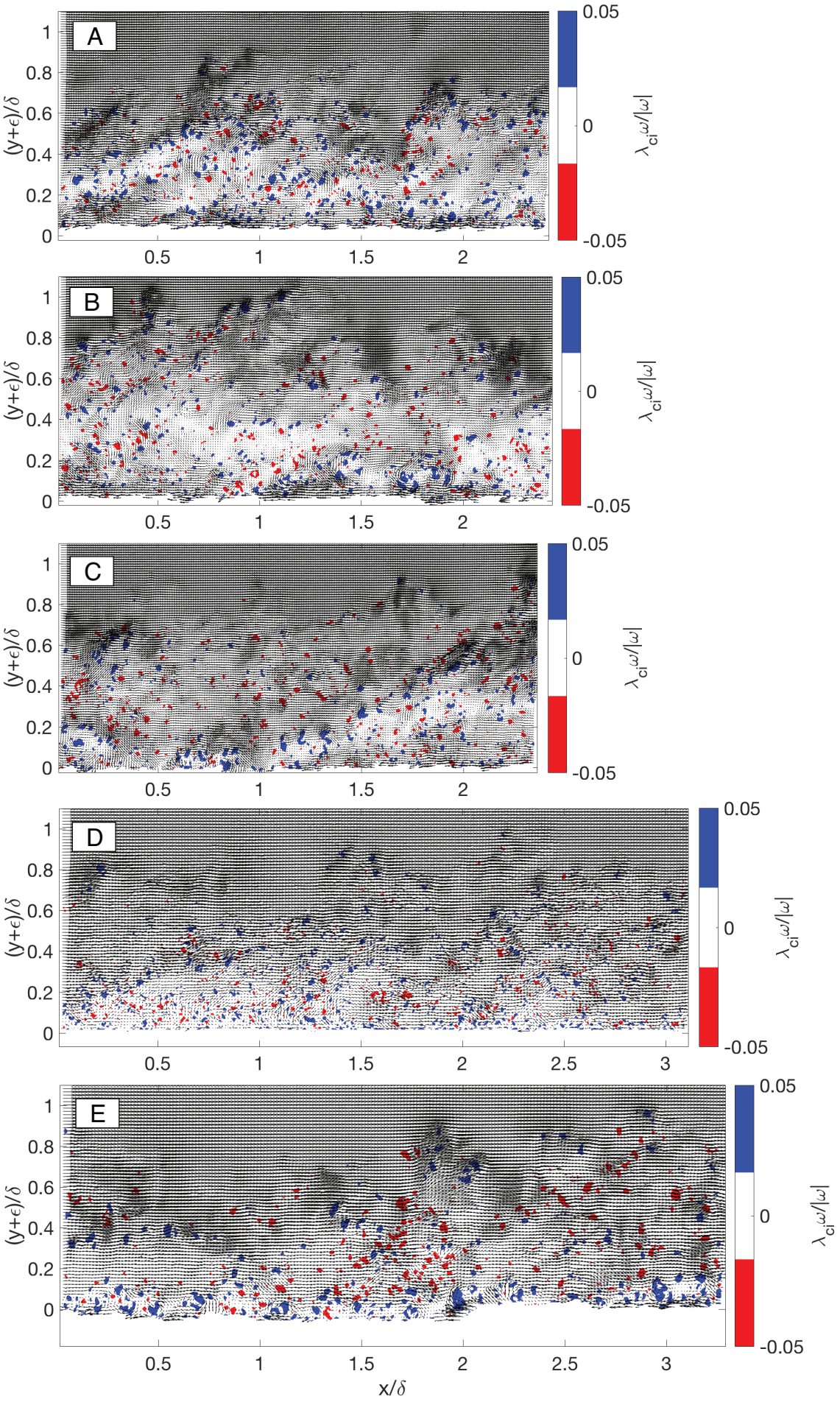
A
B
C
D
E
(y+ϵ)/δ
x/δ
0.05
0
-0.05
$\lambda_{ci}\omega/|\omega|$

Figure 16. Galilean decomposition of an instantaneous flow field over each biofilm, with $0.7U_e$ removed. The Galilean decompositions are plotted over λ_{ci}, the swirling strength, to highlight locations of rotational flow. Location of prograde rotation (rotating in the direction of the flow) are shaded in blue, and locations of retrograde rotation (rotating in the direction opposite the mean flow) are red.

Conclusion

The mechanisms by which organisms impact their environment, or engineered systems, often result from organismal- scale interactions with fluids. Here we used experimental methods to visualize and quantify these interactions for burrowing marine worms and fouling biofilms.

In Chapter 1, we show that periodic burrow ventilation results in periodic oxygen fluxes across the sediment- water interface, and that the pattern of sediment oxygenation changes when burrow ventilation behavior changes with temperature. In fact, we show that while the pattern of burrow oxygenation and oxygen flux are temperature dependent, as is the volume of sediment around the burrow that is exposed periodically to oxygen, the time integrated flux of oxygen remains relatively constant with temperature. This means that burrowing organisms mediate the effects of environmental parameters on sediment chemistry through behavioral changes. Chapter 2 continues this work on burrow ventilation by using novel in- burrow flow visualization to show that the polychaete pump using muscular undulatory body movements results in pulsatile, with the strongest oscillations near the burrow entrance. This has implications for the energetics of burrow venitlation, and also has implications for the transport of solutes within the burrow and into the sediments. Taken together, Chapters 1 and 2 provide new, detailed measurements of the fluid dynamics of burrow ventilation and the effects of burrow ventilation on sediment chemistry. Future research should explicitly measure the advective mass transport in burrows. Additionally, the transparent burrowing medium we developed can be used with other species, in order to have a comparative understanding of burrow fluid dynamics.

The results of Chapters 3 and 4 show that low form slime fouling, despite its seeming slipperyness, exacts a large drag penalty on surfaces due to roughness effects and momentum

extraction from the flow by flapping streamers. We also show that patchy biofilms and uniform biofilms have a fundamentally different flow structure, with patchy biofilms creating a plane mixing layer that greatly enhances vertical transport near the creat of the biofilm roughness elements. The drag coefficient, however, is highest for the uniform biofouling, indicating that percent cover, rather than roughness height of the biofilm, is the best predictor of drag due to biofilm. This has practical applications for determining when to clean a ship hull. It also has fundamental implications for understanding the role of biofilms in an ecological context. While biofilms may be assumed to dampen flows at the bed and reduce vertical mass transport and bed shear stresses, we show that if a biofilm is patchy, it may locally enhance bed shear stresses and vertical fluxes, with implications for sediment transport where biofilms cover intertidal sediments, for example, or nutrient transport to coral surfaces.

Collectively, the research presented in this dissertation represents an advancement in the fundamental understanding and practical application of small scale biofluidics.

Appendix i

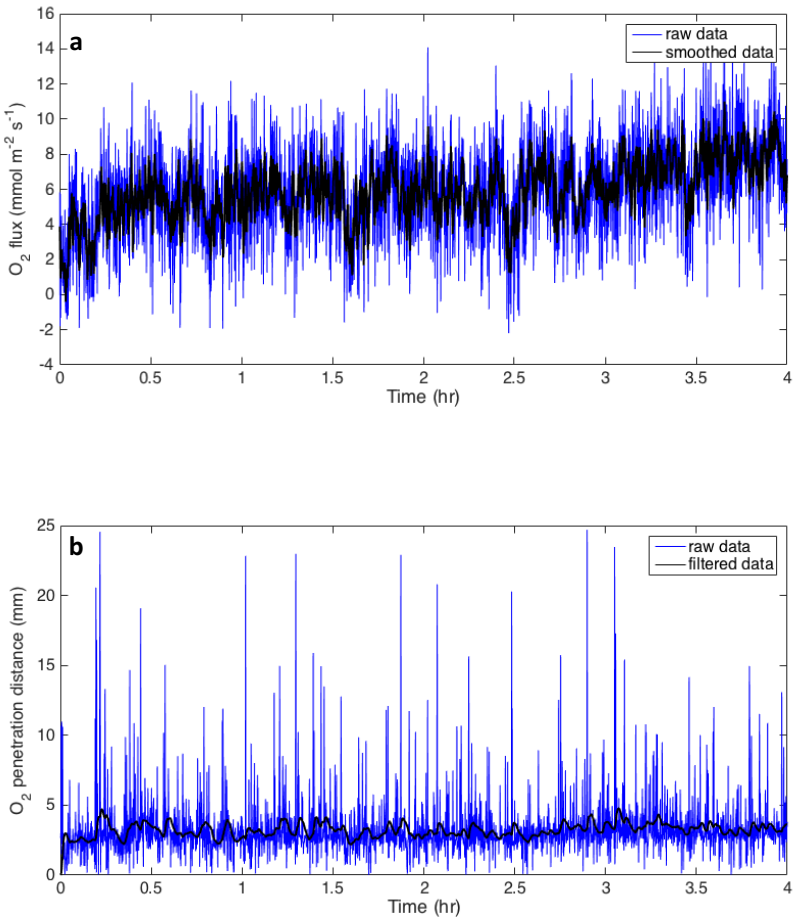

Table Ai.1. (a) Example raw data from a time series of oxygen flux across a burrow wall (blue) and that data smoothed using a Savitzky-Golay smoothing function (black). (b) Example raw data from a time series of oxygen penetration distance into a burrow wall (blue) and that data processed with a Butterworth filter.

Appendix ii

	Minimum burrow oxygenation	**Mean burrow oxygenation**	**Maximum burrow oxygenation**	**Burrow water above 20% air saturation**
	μM (% air saturation)			(% time)
6 °C (n = 4)	80 ± 20 (25 ± 7)	120 ± 30 (40 ± 8)	150 ± 20 (49 ± 6)	60 ± 28
24 °C (n =6)	50 ± 10 (22 ± 4)	80 ± 10 (37 ± 2)	110 ± 10(50 ± 7)	98 ± 1.3
33 °C (n = 5)	20 ± 3 (11 ± 1)	40 ± 1 (21 ±1)	60 ± 2 (32 ± 1)	54 ± 6

Burrow oxygenation values were taken from the middle of the burrow; n, number of sequences. Number of individuals (N) = 4. Values are mean ± s.e. Each sequence is an average of measurements taken from between one and six locations along the burrow. There was at least one sequence at each temperature per individual.

Table Aii.1. Burrow oxygenation patterns at the three temperature treatments.

Appendix iii

	Oxygenation periodicity	**Flux periodicity**	**Mean flux**	**Maximum flux**	**Mean O_2 penetration distance**	**Maximum O_2 penetration distance**
	($x10^{-4}$ Hz) (N = 4)		($mmol\ m^{-2}\ d^{-1}$) (N=4)		(mm) (N=4)	
6 °C	1.7 ± 0.6 (H = 20) (n = 4)	2.4 ± 0.7 (H = 20) (n = 4)	1.5 ± 0.03 (H = 20) (n = 4)	2.7 ± 0.02	3.4 ± 0.5	6.2 ± 0.9
24 °C	4.5 ± 0.3 (H = 40.2) (n = 8)	4.9 ± 0.9 (H = 20.2) (n = 4)	1.3 ± 0.1 (H = 24.2) (n = 6)	3.3 ± 0.7	2.3 ± 0.3	3.9 ± 0.3
33 °C	10.6 ± 3.0 (H = 16) (n = 4)	9.9 ± 2.7 (H = 16) (n = 4)	1.7 ± 0.4 (H = 17.8) (n = 5)	3.7 ± 0.5	1.6 ± 0.1	2.8 ± 0.2

Table Aiii.1. Oxygenation and flux periodicity and the penetration distance of O_2 into the burrow wall. Burrow oxygenation values were taken from the middle of the burrow; n, number of sequences. H is the number of hours of recordings used. Number of individuals (N) = 4. Values are mean ± s.e. Each sequence is an average of measurements taken from between one and six locations along the burrow. There was at least one sequence at each temperature per individual. The overall mean value is the mean of the mean value of each individual at all three temperatures.

Appendix iv

In engineering literature, the streamwise velocity profile in the log-law, or overlap, region is described by

$$U^+ = \frac{1}{\kappa}\ln(y+\varepsilon)^+ + C - \Delta U^+ \qquad \text{(Aiv.1)}$$

where U^+ is the mean streamwise velocity, ΔU^+ is the roughness function, and ε is the vertical displacement of the virtual origin, and κ and C are experimentally determined constants (Jiménez 2004). The + superscript indicates normalization in inner units, because viscosity dominates near the bed. Inner units are (U_τ or $\frac{\nu}{U_\tau}$). Because we have 2D data, the vertical axis is given as y. However, in hydrology, the log-law equation is typically given as

$$U(z) = \frac{U_\tau}{\kappa}\ln\frac{z-\varepsilon}{z_o} \qquad \text{(Aiv.2)}$$

where z_o is the roughness length scale (Reidenbach et al. 2010). Using $0.033k_s^+$ for z_o, where k_s^+ is the equivalent sand grain roughness height (normalized by $\frac{\nu}{U_\tau}$), experimental data in the fully rough regime (where the size of the roughness elements is large enough to fully disrupt the viscous layer) gives

$$U^+ = \frac{1}{\kappa}\ln\frac{z-\varepsilon}{k_s} + 8.5 \qquad \text{(Aiv.3)}$$

These three equations, which are used by default in different fields, show how z_o (also referred to as k_o in some places), ΔU^+ and k_s are essentially interchangeable quantifications of the roughness parameter (Jiménez 2004; Yuan and Piomelli).

References

Jiménez J. 2004. Turbulent flows over rough walls. *Annu. Rev. Fluid Mech*. 36:173-96.

Reidenbach MA, Limm M, Hondzo M, Stacey MT. 2010. Effects of bed roughness on boundary layer mixing and mass flux across the sediment-water interface. Water Resources Research. 46(7).

Yuan J, Piomelli U. 2014. Estimation and prediction of the roughness function on realistic surfaces. *Journal of Turbulence*. 15(6):350-65.